Identification and active thermomechanical control in precision mechatronics

Document status and date:
Published: 07/01/2021

Document Version:
Publisher's PDF, also known as Version of Record (includes final page, issue and volume numbers)

Please check the document version of this publication:

• A submitted manuscript is the version of the article upon submission and before peer-review. There can be important differences between the submitted version and the official published version of record. People interested in the research are advised to contact the author for the final version of the publication, or visit the DOI to the publisher's website.
• The final author version and the galley proof are versions of the publication after peer review.
• The final published version features the final layout of the paper including the volume, issue and page numbers.

Link to publication

Identification and Active Thermomechanical Control in Precision Mechatronics

Enzo Evers

Identification and Active Thermomechanical Control in Precision Mechatronics

Enzo Evers

disc

The author has successfully completed the educational program of the Graduate School of the Dutch Institute of Systems and Control (DISC).

ATC

This work is supported by the Advanced Thermal Control Consortium (ATC).

TU/e EINDHOVEN UNIVERSITY OF TECHNOLOGY

Identification and Active Thermomechanical Control in Precision Mechatronics

PROEFSCHRIFT

ter verkrijging van de graad van doctor aan de
Technische Universiteit Eindhoven, op gezag van de
rector magnificus prof.dr.ir. F.P.T. Baaijens, voor een
commissie aangewezen door het College voor
Promoties, in het openbaar te verdedigen
op donderdag 7 Januari 2021 om 16:00 uur

door

Enzo Evers

geboren te Tilburg

Dit proefschrift is goedgekeurd door de promotoren en de samenstelling van de promotiecommissie is als volgt:

voorzitter: prof.dr. H. Nijmeijer
1e promotor: dr.ir. T.A.E. Oomen
2e promotor: dr.ir. A.G. de Jager
leden: prof.dr. J. Sjöberg (Chalmers University of Technology)
                 prof.dr.ir. J.F.M. Schoukens (Vrije Universiteit Brussel)
                 prof.dr.ir. J.P.M.B. Vermeulen

adviseurs: dr.ir. J.M.M.G. Noël
                 dr.ir. R.W. van Gils (Philips Innovation Services)

Het onderzoek dat in dit proefschrift wordt beschreven is uitgevoerd in overeenstemming met de TU/e Gedragscode Wetenschapsbeoefening.

Summary

Identification and Active Thermomechanical Control in Precision Mechatronics

In modern times, technological advancements and innovations are ubiquitous. To facilitate these developments requires tremendous effort in the high-tech manufacturing, life sciences and the medical industry. These industries often employ sophisticated multidisciplinary machinery, particularly in the electro-mechanical domain that we often denote as mechatronics. Keeping up with the increased demands on accuracy and throughput on these mechatronic systems requires complex systems-of-systems based designs and advanced control methods. Impressive progress in advanced motion control of precision mechatronics has led to a situation where motion systems are capable of positioning up to the nanometer scale. As a result of these advancements, the positioning errors are almost completely compensated and thermally induced deformations have relatively become more pronounced on the overall system performance. Therefore, the thermomechanical aspects are no longer negligible and must be taken into account.

Accurate modeling of thermomechanical systems is challenging, e.g., due to transient dynamics with large time constants, model parameter uncertainty, and model complexity. In sharp contrast, modeling for advanced motion control, using frequency response function (FRF) measurements, is fast, accurate, and inexpensive.

Classically, control of thermal systems is done using a heater based actuation system. However, these actuators are limiting for active thermal control since they do not allow for cooling. In this thesis, first steps towards active thermal control using thermoelectric elements are taken. These elements allow dynamic temperature control, i.e., both heating and cooling. To facilitate their use in thermal control, a comprehensive framework for modeling and control is presented.

The aim of this thesis is to provide a concrete approach to move towards active thermomechanical control in precision mechatronics. Modeling and control methodologies are developed covering both the thermal and mechanical domain.

The contributions are divided into the following research areas.

1) Modeling: An approach is developed that provides a fast and accurate modeling procedure for thermal systems. It addresses several challenges that are typically faced when modeling the thermodynamics in mechatronic systems. Specifically, transients are addressed by using a local modeling approach. A novel algorithm is developed that facilitates appropriate incorporation of prior knowledge into the local modeling domain. The resulting framework allows for fast and accurate identification of frequency response functions of thermomechanical systems with reduced experiment time when compared to traditional methods. Moreover, the accuracy is further improved by the incorporation of ambient air temperature measurements as an additional excitation source. The identification technique is implemented on various experimental setups and industrial applications and yields significantly improved identification results under transient conditions. A high-fidelity parametric model is obtained by constructing a lumped-mass parametric model and leveraging the improved frequency response function to calibrate the model parameters. This grey-box approach is shown to be successful in an industrial application case study. In this thesis, an approach to temperature-dependent modeling of thermoelectric elements is presented using a first principles approach with parameters based on experimental measurements. The procedure yields a temperature-dependent model that is valid for a large operating range, facilitating the use in applications beyond those of steady state operation.

2) Actuation: To accurately control a thermoelectric element is challenging since its dynamics are both state-dependent and non-linear. By leveraging the temperature-dependent model a feedback linearization technique is presented that achieves linearity and stability of the input to output dynamics of the thermoelectric element. Moreover, by using an model-based observer, this linearizion is achieved using a limited number of temperature sensors.

3) Control: In this thesis a systematic procedure for bi-directional coupling of multiple systems to achieve improved overall performance in a systems-of-systems application is presented. It provides filter design guidelines combined with a robust stability guarantee. The procedure is illustrated in an industrial case study of a waferscanner and can also be applied in the thermomechanical domain to provide inter-disciplinary coupling.

The overall result of this thesis is a comprehensive approach for the identification and control of thermomechanical aspects in precision mechatronic systems. Facilitating the transition towards an active thermomechanical control approach by providing contributions in the areas of modeling, actuation, and control.

Contents

Introduction

Abstract: For next-generation mechatronic systems it is expected that a passive isolation approach to thermally induced deformations is no longer sufficient to achieve the increased demands on accuracy and throughput. The main idea pursued in this thesis is geared towards predicting and controlling thermally induced deformations. This is done by taking an active approach towards thermally induced deformations through accurate modeling, actuation, and control. In this chapter, the context for this thesis is presented, accompanied by the research challenges and the contributions.

1

1.1. Digital industrial revolution

Almost every aspect of modern society is infused with digital technology. The vast amount of information available through a pocket size smartphone would have been unimaginable only a generation ago. Equally impressive is the rate of development and adoption of new technologies in the manufacturing industry. These developments are a key enabler for globalization, innovation, and trade (Manyika et al., 2012) by facilitating new means of affordable intercontinental logistics and real-time global communication pipelines.

In the manufacturing industry this increase in real-time communication possibilities has yielded a fast-paced transition towards digitalization of traditional manufacturing and industrial practices, using modern smart technology. It can be considered as both a result of and facilitator for high-tech mechatronic manufacturing systems. Great progress has been made in the different fields of research and manufacturing, examples of this progress, shown in Figure 1.1, include the following.

- In the field of life and material sciences, transmission electron microscopes have become increasingly capable of imaging to the atomic level (De Jonge et al., 2010). Current generation microscopes are able to visualize, with great accuracy, the atomic structure of complex molecules and crystalline formations.

- In the semiconductor industry wafer scanners are used in the exposure step, where an image of a chip layer is exposed onto a photo resist in a lithographic process. Positioning accuracy and stability during this process is crucial in obtaining accurate exposure of the semiconductor substrate. Impressive progress in waferscanner technology (Heertjes et al., 2020) is the key enabler for Moore's law (Moore, 1965) which states that the number of transistor per surface area of the semiconductor die will double every 18 months.

- In the medical industry, blood diagnostics that were classically performed in a full size lab, can now be performed in a lab on a chip by leveraging advancements in microfluidic actuators and sensors. These handheld diagnostic devices enable improved quality of life for patients by reducing the need for hospital visits. Mass production of these systems can reduce the cost price and improve the availability of high quality medical care in less affluent countries. Moreover, inexpensive and rapid testing offers major advantages in managing the initial outbreak during a viral epidemic (Zhu et al., 2020).

(a) Life sciences

(b) Semiconductor

(c) Medical
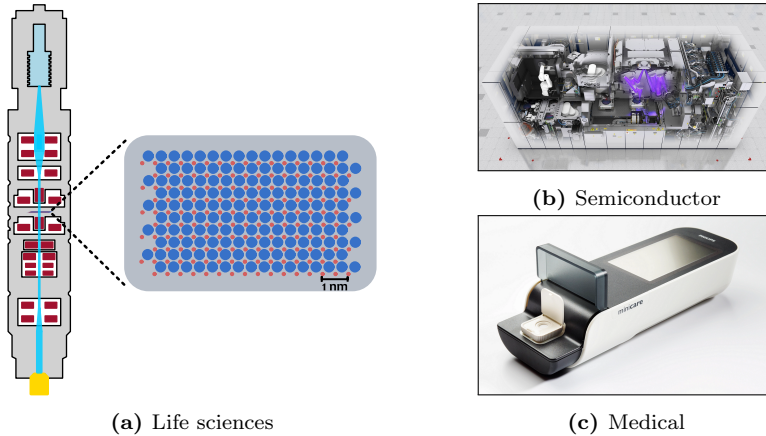
Figure 1.1. Examples from different industries that have made revolutionary progress in research and manufacturing technology. Illustrating a transmission electron microscope (a), a waferscanner (ASML, 2020) (b), and a handheld blood diagnostic device (Philips, 2020) (c).

1.1.1. Digitalization in manufacturing

The digital revolution is a strong driving factor of the shift in the classical manufacturing paradigm. This shift is seen in examples such as moving from a traditional printing press to printing on demand through cloud services and from mass parts production using expensive molds to one-off prototype production using additive manufacturing in 3-D printers. These developments are accompanied by manufacturing equipment that transitions from largely mechanical devices to a complex mechatronic systems often consisting of multiple sub-systems.

The term mechatronics is ubiquitous in both industry and academia and it was first coined by Japanese engineer Tetsuro Mori of the Yasakawa electric company in 1969 (Dixit et al., 2017). Its conception was a result of a combination of 'mecha' from mechanics and 'tronics' from electronics. It involves the integration between components, i.e., hardware, and information-driven functionality, i.e., software, resulting in integrated systems (Isermann, 2005). More precisely, in this thesis, and in line with Bolton (2019), mechatronic system design is described as a design philosophy where there is a co-ordinated and concurrent effort to incorporate mechanical engineering with electronics and computer science in the design of products and processes. Consequently, it is common in mechatronic systems that mechanical functionality is replaced by electronic adaptations. This facilitates agile design principles where the mechanical design, that is often expensive and time consuming to iterate over, is complemented by fast moving developments in electronics and computer algorithms.

A prime example of a mechanical controller that was commonplace in indus-
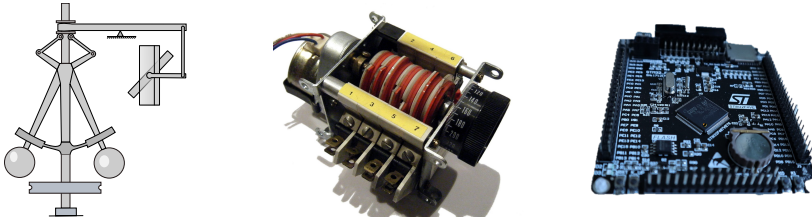
(a) Centrifugal governor.   **(b)** Cam timer mechanism (Wikimedia and Fylip22, 2010).   **(c)** Embedded controller.

Figure 1.2. Examples of traditional, mechanical, control systems (a,b) and their modern implementation (c).

try is the centrifugal governor shown in Figure 1.2a adapted by James Watt to regulate the rotational speed of steam engines by controlling the valve based on centrifugal force on the rotating balls. A more recent example is a cam timer mechanism, shown in Figure 1.2b, often used in washing machines. This is already considered as a mechatronic system since it uses an electrical motor to drive a mechanical cam timing mechanism to schedule the pump, wash, and centrifuge parts of a washing cycle. It relies on the fixed frequency of the AC power grid and the electrical motor to provide accurate timing.

In modern systems, both examples presented in Figure 1.2 are often replaced by a digital controller, implemented on an embedded microprocessor as shown in Figure 1.2c, complemented with sensors and electro-mechanical actuators. This facilitates additional functionality such as reporting error codes and actively responding to a system malfunction. Moreover, these devices are getting increasingly connected to other devices through real time communication pipelines. This has led to the Internet-Of-Things (IOT) and has yielded an interconnected network of smart devices connected through the Internet and cloud services to facilitate data gathering and collaborative behavior to increase automation of common tasks. These developments towards digitalization and automation of tasks through increased connectivity is often colloquially referred to as industry 4.0 (Bonilla et al., 2018; Ustundag and Cevikcan, 2018).

1.2. Shift in the manufacturing paradigm

Mechatronic systems in manufacturing industry are increasingly complex and under stringent demands on their throughput and accuracy. In this thesis, focus is placed on precision mechatronics that are often characterized by strict requirements on accuracy and throughput, intricate systems-of-systems type designs, and high development costs and/or high unit cost, e.g., waferscanners, electron microscopes, and portable medical diagnostic devices.

(a) Traditional   **(b)** Modern   **(c)** Next-generation
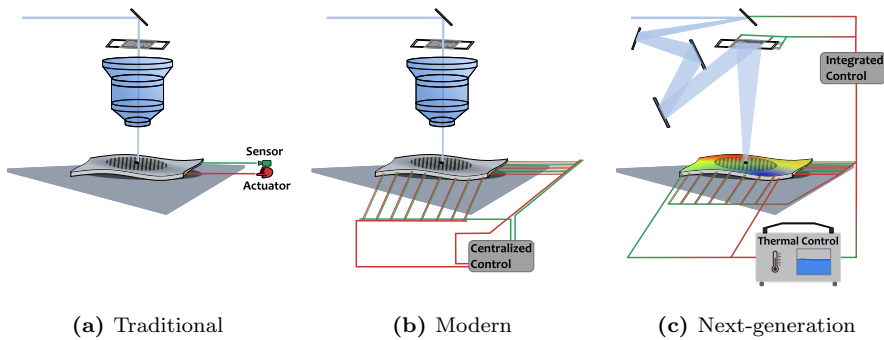
Figure 1.3. The evolutionary phases of mechatronic system design, illustrated through a waferscanner example. Going from traditional, modern, to next-generation mechatronic systems. It illustrates the increase of complexity and inter-connectivity throughout the evolution of mechatronic systems.

1.2.1. Superior performance through control

The synergistic combination of mechanical hardware with smart actuators, sensors, and algorithms allows modern mechatronic systems to achieve superior cost-to-performance ratios, throughput, and accuracy when compared to previous generations. Obtaining a similar performance level by using purely elaborate mechanical designs and exotic material choices would be extremely cost and time prohibitive due to the often iterative nature of the design process. This would require time and resources greatly beyond that of iterating over a digital control implementation. It is clearly preferable to leverage existing system architectures to increase performance. In this thesis, and in line with mechatronic principles, superior performance is achieved by complementing the existing system design through accurate modeling and control. The impressive performance of modern generation mechatronics is the result of a gradual evolution in complexity of the design and control approaches.

1.2.2. Transition in control

In traditional mechatronic systems flexibilities and internal deformations as well as thermally induced deformations are often neglected in favor of rigid body control. Moreover, the system design often relies on passive isolation from the environment for thermal disturbances and external vibrations, and interaction between subsystems are not taken into account. This approach yields a control structure where each of the six degrees-of-freedom (DOF) is actively controlled by a (direct) measurement and matching actuator system, illustrated in Figure 1.3a. Interaction between the DOFs is characterized and decoupled where possible (Skogestad and Postlethwaite, 2009) to achieve a decentralized control

structure. The design of the high performance feedback controllers is subsequently done in a Single-Input Single-Output (SISO) context where analyses for performance and stability are typically done on a loop-to-loop basis.

The revolutionary phase beyond traditional mechatronic systems is illustrated in Figure 1.3b, where the system is no longer considered as a rigid body or in a thermal equilibrium. These systems are often constructed to be more lightweight to achieve superior acceleration, speed and throughput. Consequently, flexible dynamics and internal deformations are more apparent in the full system behavior. The mechanical design is complemented by more elaborate electromechanical actuator systems combined with advanced Multiple-Input Multiple-Output (MIMO) centralized feedback controllers.

1.3. Next-generation mechatronic systems

The next-generation mechatronic system design, illustrated in Figure 1.3c, will require an increasingly elaborate mechatronic system design combined with smart algorithms to achieve its desired performance specifications. Next-generation systems are capable of positioning accuracy up to the nanometer level, this makes achieving the required specifications increasingly challenging, this is illustrated in the following example.

Motivating example

Figure 1.4. Schematic representation of a transmission electron microscope and corresponding thermal expansion loop (—) through the coils (■), positioning stage (□), and sample holder (■).

Consider a 1-D thermal expansion loop in an electron microscope, illustrated in Figure 1.4, with a length of $300 \cdot 10^{-3}$ [m] and an average Coefficient of Thermal Expansion (CTE) of $\alpha = 15$ [μm/m/K]. To achieve the required position stability of $0.5 \cdot 10^{-9}$ [m/min], the temperature fluctuation cannot exceed a threshold of 0.1 [mK/min].

1.3.1. The increasing role of thermal aspects

The stringent demands on accuracy and throughput of next-generation mechatronic systems yields increased power dissipation within these systems. Examples include, cutting forces and spindle losses in machining tools (Fraser et al., 1998), heating of electro-mechanical actuators, increased source power for proper exposure in lithographic systems (Van Schoot et al., 2017), and increasing dissipation in the electron beam generator in transmission electron microscopes. This results in the thermomechanical system behavior becoming an increasingly important part of the overall system accuracy and performance. Indeed, in recent systems, the thermomechanical dynamics are a limiting factor in the achievable performance, i.e., overlay errors in lithography and image drift characteristics in electron microscopy.

1.3.2. Thermally induced deformations

Impressive progress in advanced motion control (Oomen, 2018) has led to a situation where the thermally induced deformations are of essential importance in the overall system performance. These deformations are induced by thermal expansion of constructive elements in the mechatronic system. Indeed, thermal gradients can induce complex deformations and warping due to difference in the expansion coefficient of various materials used in typical manufacturing equipment. Typically, a solution to these thermomechanical deformations is to over-build the structure and use slightly exotic materials such as Invar or Zerodur (Box, 2008) that have a low Coefficient of Thermal Expansion (CTE).

    In sharp contrast, the main idea pursued in this thesis is geared towards predicting and controlling deformations rather than relying on a passive isolation approach. By taking an active control approach towards thermally induced deformations, a significant saving in the mechanical design can be achieved (Box, 2008) by leveraging inexpensive materials. While these materials are often less suitable for strong thermal gradients, due to their higher CTE, if their thermomechanical behavior is highly predictable it can be taken into account during the control design. An early example of this is described in Attia (1998); Attia (1999); Fraser et al. (1998) where the authors proposed methods for modeling and control of thermally induced deformations in machine tools. In Koevoets et al. (2009) it is shown that using a reduced order model based on modal order reduction and a limited set of temperature sensors an accurate prediction can be constructed for the thermally induced deformation in a c-frame experimental setup.

    To achieve the required performance in next-generation mechatronic systems it is expected that the synergistic balance between mechanical design, electromechanical actuators and sensors, and smart control algorithms must be extended to encompass also the thermomechanical behavior of the system.
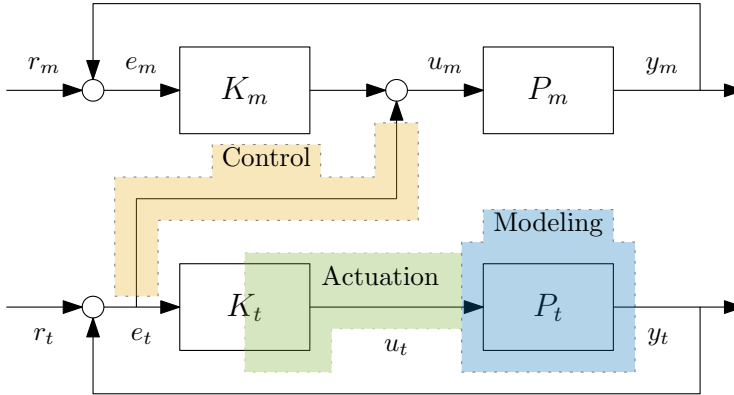
Figure 1.5. A block diagram illustrating the connection between the research areas in this thesis. With P the plant, K the controller, r the reference, e the error, u the actuator effort, and y the output. The block diagram is separated into a mechanical part, indicated by the subscript m, and a thermal part, indicated by the subscript t. Typically, the characteristic time constants of the mechanical system are significantly smaller than those of the thermal system. The research areas of this thesis are indicated by the shaded areas □,□,□, where the color is kept consistent with the topics as discussed in Subsection 1.4.1.

1.4. Thermal challenges in next-generation mechatronics

The next-generation of manufacturing equipment is envisioned to consist of a synergistic mechatronic design that requires aspects from mechanical, electrical, and thermal engineering disciplines. In this section, the requirements for incorporating thermomechanical aspects in precision mechatronics are investigated and a closer look at some of the key challenges faced in this area of research is provided.

1.4.1. Requirements for thermomechanical control

Incorporating the thermomechanical effects into the mechatronic design philosophy is subject to some essential requirements on the topics of both modeling, actuation, and control. This is demonstrated in the thermomechanical control architecture as illustrated in Figure 1.5, where thermal and mechanical control systems exists alongside each other. The areas of research in this thesis are indicated by the shaded areas, and their color is kept consistent throughout.

Requirements 1. *For each of the research areas, as indicated in Figure 1.5, the following requirements are imposed.*

Modeling

In view of increased system complexity and sensitivity towards disturbances a relevant modeling approach should achieve the following.

- *Facilitate models with an increasing amount of inputs and outputs.*

- *Utilize transient data.*

- *Incorporate (ambient) disturbances.*

- *An appropriate balance between data-driven and first principles.*

Actuation

A suitable actuation approach for thermal control should possess the following properties.

- *Facilitate both heating and cooling.*

- *Localized thermal actuation.*

Control

Control for next-generation mechatronics should encompass the following properties.

- *Leveraging existing control architecture by providing add-on controllers.*

- *Achieve performance beyond that of individual sub-systems.*

- *Maintain system stability.*

In the next sections, a more detailed exposition of each of the research areas is provided along with the research challenges that this thesis aims to address.

1.4.2. Modeling

Classical modeling approaches can not deal with the required complexity and accuracy for next-generation mechatronic systems. In this thesis, the following challenges in view of modeling, i.e., obtaining a representation of the system P_t in Figure 1.5 marked by □, for thermal dynamics in precision mechatronics are identified.

1.4.2.1 Complexity: Typically, for thermodynamical analysis of large machine structures a Finite Element Modeling (FEM) approach is employed. The approach constructs an approximation of the underlying Partial Differential Equations (PDE) by constructing a connected set of Ordinary Differential Equations (ODE) that are more tractable to compute. This is done by spatial discretization using a mesh of the geometric structure, and depending on the granularity this approach can result in models containing a significant amount of states. This often necessitates the use of model reduction (Antoulas et al., 2004) or approximation (Van den Hurk et al., 2018) techniques to facilitate realtime execution of the model. An example of a FEM model is shown in Figure 1.6a that illustrates a finite element mesh and temperature field of the Precision Stage Application (PSA) setup used in Chapter 4 of this thesis.

Conversely, for control purposes, a (thermal) system is often reduced to a single discrete mass. Consequently, its dynamical model in the form of a transfer function, can be described as a first order system $G = \dfrac{1}{1 + \tau s}$ with s the Laplace variable and $\tau = \dfrac{mc_p}{h_c}$ the first order time constant with mc_p the thermal capacity and h_c the convection coefficient towards the ambient air. This equates to solely considering the first thermal eigenmode of the structure as illustrated in Figure 1.6b, neglecting any spatial gradients.

In this thesis, it is desired to obtain high-fidelity models that remain tractable for control applications, i.e., contain a "reasonable" amount of states. The models should be balanced according to the required accuracy, complexity and practical usability.

> **Research challenge R1.** *Develop a framework for (parametric) modeling of thermodynamical systems that yields high-fidelity models that are tractable for simulation and control applications.*

1.4.2.2 Accuracy: The time constant τ of a first order (thermal) system can be considered as the point at which its output first passes $1 - e^{-1} = 0.6321 = 63.21\%$ of its final steady-state value, this is illustrated in Figure 1.7. In Atsumi et al. (2013); Paalvast (2010) small mechanical structures are considered that have a thermal time constant in the order of milliseconds. However, for the systems considered in this thesis the time constant is often in the order of multiple seconds, minutes, and even hours. For example the time constant of the housing of an electron microscope is approximately 4 hours (Evers et al., 2019b; Lamers, 2010) and for the PSA in Figure 1.6 the first time constant is 20 minutes. In sharp contrast, the systems typically considered in advanced motion control (Oomen, 2018) have characteristic time constants, related to their natural frequency, in the order of milliseconds. Invariably, a thermal system takes significantly longer to reach steady-state operation, e.g., $5\tau = 20$ [h] in the
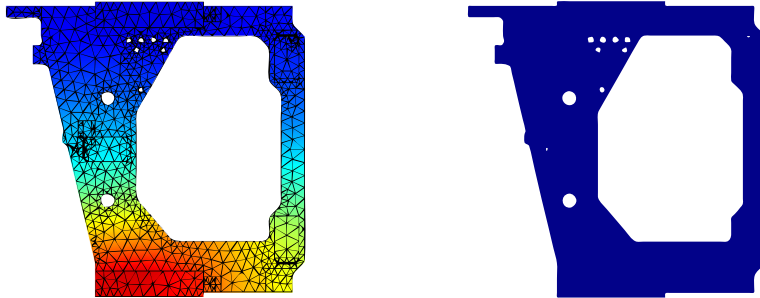
(a) High granularity finite element model.   **(b)** Simplified 1st order model.

Figure 1.6. Illustrating two extremes in thermal modeling, on the left side a model with high granularity finite element model is shown, resulting in $N = 9000$ states. It employs a detailed spatial discretization to provide accurate temperature fields. While on the right side a (overly) simplified first order model, i.e., $N = 1$ and considering only the first thermal eigenmode of the system, is shown that assumes constant temperature over the whole spatial domain.

electron microscope application. Consequently, in view of system identification, the application of the classical Emperical Transfer Function Estimate (ETFE) (Ljung, 1999; Pintelon and Schoukens, 2012) can yield biased results since it assumes that the system is in steady-state.

> **Research challenge R2.** *Develop an accurate approach for frequency response function identification that exploits data obtained under transient conditions.*

1.4.3. Actuation and Control

Current solutions for thermal control in mechatronic systems often focus on isolation and passive disturbance rejection. In this thesis, it is desired to move towards an active control approach to yield superior performance.

1.4.3.1 Thermal actuators: Actuation for control of thermal dynamics in mechatronic systems is typically done through a combination of electrical heating at specific locations (Guo, 2014) and bulk cooling using conditioned water circuits (Bukkems et al., 2018). The local heating is achieved through Joule heating by passing current through an electrical resistor, often in the form of a thin-film foil or coil. Advantages of resistive heating are the relatively fast
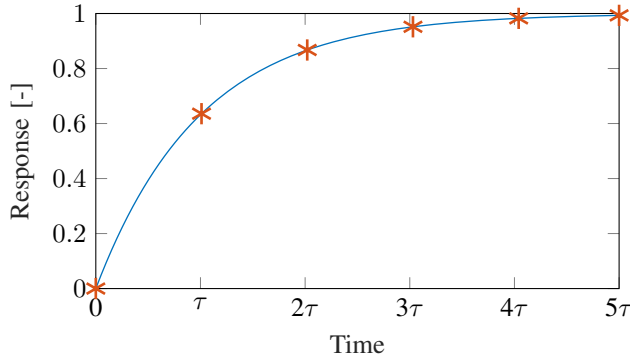
Figure 1.7. A typical response (—) and associated time constants τ (✳) of a first-order system.

response time and ability to modulate the control action. An obvious downside is the inability to provide cooling. In contrast, water cooling is typically able to provide both heating and cooling but has a relatively slow response time and can introduce unwanted flow-induced vibrations into the machine structure. Moreover, water cooling is often considered bulk cooling and is less suitable to provide accurate local temperature control.

A common approach to achieve active local cooling with water cooling is to lower the setpoint of the water cooling system and subsequently compensate this by constantly providing power to local resistive heaters or local fluid stream heaters (Schepens et al., 2020). By then reducing the power to the local heaters, a cooling effect is achieved. However, this approach is not always suitable as it continuously injects energy into the system. Moreover, the water cooling and local heaters are invariably differently spatially distributed, inducing a thermal gradient in the system that can cause additional challenges.

Efficiently controlling local thermal gradients requires a new actuator paradigm to provide localized control, e.g., providing u_t in Figure 1.5 marked by ▫, providing both heating and cooling.

> **Research challenge R3.** *Explore a new avenue of actuators for thermal control in mechatronic systems that provide the possibility for both heating and cooling and localized temperature control.*

1.4.3.2   Integrated control: The next-gen mechatronic system design increasingly incorporates multiple subsystems to achieve the required overall system performance. This synergistic collaborative effort must be coordinated through appropriate control algorithms. A typical approach to multivariable

control is to apply decoupling techniques (Skogestad and Postlethwaite, 2009) to facilitate decentralized control design. The design of modern multidisciplinary mechatronic systems invariably leads to separation into submodules to facilitate decentralized design and manufacturing. It is expected that next-geneneration manufacturing systems with their integrated design spanning multiple domains, e.g., mechanical, electrical, and thermal, will require additional collaborative controller design to achieve optimal performance. Ideally there exists a complementary controller that incorporates the existing decentralized control structure of the submodules. This coordinating controller can provide additional control commands, e.g., the path from e_t to u_m in Figure 1.5 marked by □, to increase the collective performance of the subsystems without impacting the system stability.

In Evers (2016) early results on synchronized motion control illustrated the potential performance advantages by inter-connecting individual control systems. Within the context of thermomechanical control, it is expected that coupling the mechanical and thermal control systems will become increasingly relevant, e.g., compensating mechanically for thermally induced deformations. An application of such coupling is found in Koevoets et al. (2007) where a reduced order model is used to predict thermally induced deformations to facilitate error-compensation.

> **Research challenge R4.** *Provide a framework for an integrated control approach that facilitates the connection of multiple control systems, including interconnecting the thermal and mechanical control system to achieve superior overall performance.*

1.5. Approach and contributions

The aim of this thesis is to facilitate superior overall system performance for next-generation high-tech mechatronic systems, specifically by addressing thermomechanical challenges. It does so by providing several contributions that each focus on a different part of the research challenges. In this section, an overview of the contributions is provided alongside an account of the research approach and context.

1.5.1. Modeling

In Chapter 2, an overview is presented of the challenges faced when trying to model the thermal dynamics in view of advanced motion control. Subsequently, an approach to combat these challenges is provided. A systematic application of this approach will result in a high-fidelity model of the thermodynamical system thereby facilitating the application of advanced control. The approach is demonstrated successfully on a representative experimental setup.

1

> **Contribution C1.** *A fast and accurate approach to parametric modeling of thermodynamics in precision mechatronics.*

The approach consists of the following components.

- Obtaining a high-fidelity FRF of the thermal dynamics through the approach that is described in more detail in Chapter 4.

- Incorporation of ambient temperature measurements as additional inputs to improve low-frequency estimation accuracy of the FRF.

- Accurately calibrating the temperature dependent convection coefficient of the heat transfer of the system towards the ambient air using a dedicated experiment.

- Leveraging the high-fidelity non-parametric FRF the parameters of a lumped-mass model of an experimental setup are optimized. This yields a high-fidelity multivariate parametric model suitable for simulation and advanced control applications.

In Chapter 3, focus is placed on closed-loop and multivariable context in identification for (advanced motion) control.

> **Contribution C2.** *A demonstration of the importance of transient measurements, closed-loop conditions, and multivariable context in identification of non-parametric frequency response functions.*

The contribution is made by illustrating the following aspects.

- Transients in system identification, e.g., a bias resulting from transient contributions in the measurement data.

- Addressing the bias that can occur during closed-loop identification caused by external disturbances. With increasingly sensitive systems, this aspect is expected to be increasingly relevant.

- Guidelines for the correct procedure to multivariable system identification. Specifically illustrating the importance of matrix versus element wise inversion of the Frequency Response Matrix.

The aspects are illustrated on a multivariable motion control setup to provide relevant experimental results for each of the aspects of the contribution. The results are demonstrated on a mechanical example and can be extrapolated to thermal applications.

In Chapter 4, a comprehensive framework for local parametric modeling is presented. It leverages a novel parameterization for the local basis that facilitates a reliable quality metric by providing accurate expressions for the estimation variance.

> **Contribution C3.** *A comprehensive framework for a local parametric modeling approach using rational functions and a reliable quality metric.*

The contribution can be divided into the following parts.

- A local parametric method is developed that uses a linearly parametrized basis, leading to an efficient optimization and closed-form solution.

- Providing an accurate variance analysis, yielding a reliable quality metric.

- Developing necessary theory of Orthogonal Basis Functions (OBF) that leverages single complex pole parameterizations that are orthogonal over the real line in the complex plane.

- Introduction of prior knowledge into the linear basis functions and providing subsequent guidelines of transforming prior knowledge from continuous or discrete time parameterizations to the OBFs on the real line.

The resulting framework is applied to examples in the mechanical and thermal domain. It achieves an increased estimation quality while maintaining a reliable quality metric.

1.5.2. Actuation

In Chapter 5, a complete step-by-step procedure is presented for the modeling, identification, and control of thermoelectric elements. These elements can be employed as thermal actuators that can both heat and cool and offer significant advantages over resistive heater based actuator systems. However, they also introduce additional challenges, these challenges are laid out and eliminated by the steps and techniques presented in Chapter 5.

> **Contribution C4.** *A step-by-step procedure for modeling and control of thermoelectric elements to facilitate localized thermal control.*

The procedure can be decomposed into the following concrete steps.

- First principles modeling of an experimental setup including a thermoelectric element. The model includes temperature dependent and non-linear dynamics.

1

- Leveraging a dedicated identification setup to calibrate the temperature dependent parameters of the thermoelectric element over a wide temperature range.

- Accurate feedback linearization of the non-linear setup using the improved temperature dependent model and a stability proof based on a Lyapunov function.

- Observer design to facilitate feedback linearization and control for situations where sensor placement is limited.

- Experimental validation of each individual step and subsequent total approach.

Application of the step-by-step procedure yields a high-fidelity temperature dependent model of the experimental setup. Using an observer based feedback linearization approach the system is linearized in its input to output dynamics. This facilitates the implementation of existing advanced linear control approaches, possibly expediting industrial adaptation. The procedure is successfully validated on a representative experimental setup.

1.5.3. Control

In Chapter 6, an approach is presented, building on earlier results in Evers (2016), that facilitates improved overall performance of next-generation mechatronic systems by coordinating the control effort of individual subsystems. It does so by introducing bi-directional coupling between the subsystems, e.g., thermal and mechanical, to yield improved combined performance.

> **Contribution C5.** *A framework to achieve increased performance in next-generation mechatronic systems using a bi-directional coupling approach between decentralized control systems, with a stability guarantee. Facilitating both intra-domain and inter-domain coupling, i.e., mechanical to mechanical and mechanical to thermal domains.*

The contribution consists of the following elements.

- Solidifying the framework presented in Evers (2016) with rigorous derivations, proofs, and design insights.

- A procedure of systematic design and analysis of add-on coupling filter that complements an existing decentralized control structure to achieve improved overall performance, encompassing previous results such as master-slave coupling.

- Design guidelines for coupling filter synthesis, suitable for both norm-optimal design and manual tuning.

- An extension based on a Double-Youla type parameterization to guarantee robust stability by considering model uncertainty bounds.

- Performance validation based on experimental measurement data for both nominal and robust filter designs.

The approach yields improved performance for next-generation mechatronic systems. It is envisioned that this class of systems will become increasingly relevant with the inclusion of different domains within the mechatronic design and control approach as described in Section 1.1.1.

1.6. Outline

An outline of the thesis is provided in this section. Each chapter of the thesis represents one of the contributions described in Section 1.5. The chapters are self-contained and it is possible to read them independently according to the specific interest of the reader. A schematic overview of the thesis and its chapters is provided in Figure 1.8. The chapters are based on the following peer-reviewed publications in the same order as they appear in the thesis.

- Evers, E., van Tuijl, N., Lamers, R., de Jager, B., and Oomen, T. Fast and Accurate Identification of Thermal Dynamics for Precision Motion Control: Exploiting Transient Data and Additional Disturbance Inputs. *Mechatronics*, Vol 70, Article 102401, 2020.

- Evers, E., Voorhoeve, R., and Oomen, T. On Frequency Response Function Identification for Advanced Motion Control, IEEE 16th International Workshop on Advanced Motion Control (*AMC2020*) - Kristiansand, Norway, 2020.

- Evers, E., de Jager, B., and Oomen, T. Incorporating prior knowledge in local parametric modeling for frequency response measurements: Applied to thermal/mechanical systems. *Under review.*

- Evers, E., Slenders, R., van Gils, R., and Oomen, T. Temperature-Dependent Modeling of Thermoelectric Elements. *In preparation for journal submission.*

- Evers, E., van de Wal, M., and Oomen,T. Beyond decentralized wafer/reticle stage control design: a double-Youla approach for enhancing synchronized motion. *Control Engineering Practice.* 83, p21-32, 2019.

1
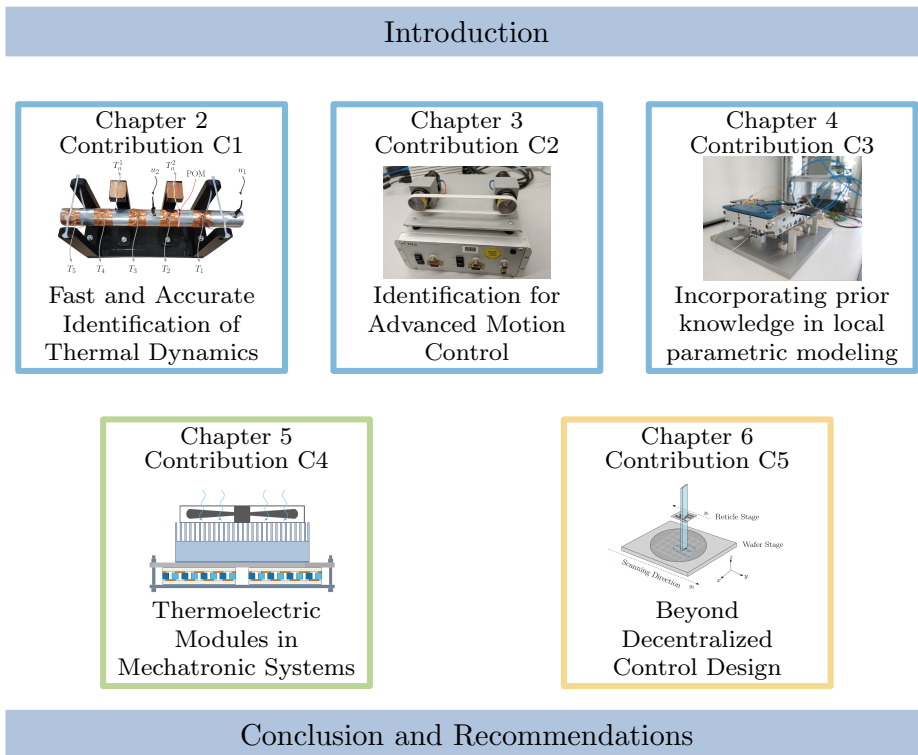
Figure 1.8. Illustration of the outline of this thesis.

Fast and Accurate Identification of Thermal Dynamics for Precision Motion Control: Exploiting Transient Data and Additional Disturbance Inputs [1]

Abstract: Thermally induced deformations are becoming increasingly important for the control performance of precision motion systems. The aim of this chapter is to identify the underlying thermal dynamics in view of precision motion control. Identifying thermal systems is challenging due to strong transients, large time constants, excitation signal limitations, large environmental disturbances, and temperature dependent behavior. In particular 1) reduced experiment time is achieved by utilizing transient data in the identification procedure. 2) an approach is presented that exploits measured ambient air temperature fluctuations as additional inputs to the identification setup. 3) the non-parametric model, obtained through 1) and 2), is used as a basis for parameter estimation of a grey-box parametric model. The presented methods form a comprehensive approach to obtain high-fidelity models that facilitate the implementation of advanced control techniques and error compensation strategies.

---

[1]The results in this chapter constitute Contribution C1 of this thesis. The chapter is based on "Evers, E., van Tuijl, N., Lamers, R., de Jager, B., and Oomen, T. Fast and Accurate Identification of Thermal Dynamics for Precision Motion Control: Exploiting Transient Data and Additional Disturbance Inputs. Mechatronics, Vol 70, Article 102401, 2020".

2.1. Introduction

Impressive progress in advanced motion control of precision mechatronics has led to a situation where thermally induced deformations are a major error source (Oomen, 2018) in positioning accuracy and are no longer negligible on the overall system performance. These deformations are typically induced by heat dissipation from actuators and encoders or by environmental temperature fluctuations. Modern precision motion systems are capable of achieving positioning accuracy in the nano-meter range. These precise movements are essential in several industrial applications, e.g., the manipulation of the sample in an electron microscope and the manufacturing of integrated circuits.

To meet the ever increasing demands to enhance the throughput and positioning accuracy, thermal deformations must be analyzed and compensated for through advanced control approaches utilizing an appropriate thermomechanical model.

Ideally, using a limited amount of temperature measurements combined with an accurate thermomechanical model enables the use of advanced control and error-compensation techniques (Evers et al., 2019c; Koevoets et al., 2007). An application of error-compensation is illustrated in Atsumi et al. (2013) where a thermomechanical actuator is employed to complement the closed-loop performance of a hard disk drive positioning system. Here, the small thermal mass of the hard disk drive magnetic head allowed the thermal actuator to obtain an extremely fast response rate. Unfortunately, the thermal mass of the systems considered in this chapter, e.g., electron microscopes, are significantly larger, thereby drastically increasing the time constant of the thermomechanical response.

Earlier solutions to compensate for the deformations in electron microscopes, e.g., image-based feedback in Van Horssen, E. P. (2018), can not always cope with large deformations and strongly depend on model quality (Salmons et al., 2010; Tarău et al., 2011). Therefore, an accurate parametric model is desired for a model-based control approach. Accurate modeling of precision thermomechanical systems is complex, resulting in large scale finite element models that require significant effort to construct due to, e.g., uncertainty in the parameters and contact resistances.

In sharp contrast, modeling for advanced motion control, see, e.g., Evers et al. (2018a); Oomen (2018) is fast, accurate and inexpensive. Significant progress has been made in Frequency Response Function (FRF) identification, particular in addressing identification in transient conditions. These recent developments include the local parametric methods, see Pintelon and Schoukens (2012) for initial results in this direction. The Local Polynomial Method (LPM) (Pintelon et al., 2010) exploits the local smoothness of the transient term that otherwise would cause a bias. Both the transient contribution and system dynamics are modeled with a polynomial in a small frequency window. The local rational

method (LRM) (McKelvey and Guérin, 2012), is an extension of the LPM that can lead to improvements over the LPM (Geerardyn et al., 2014). However, the LRM is non-convex due to the rational parameterization. In addition, the variance is only accurately computed for a high SNR, since measured output signals are included in the regression matrix.

Related work in the mechanical domain includes a newly developed rational parameterization with prescribed poles (LRMP), introduced in Evers et al. (2018a) where it is applied to a simulation example featuring lightly damped mechanics, and first applied to an experimental thermal system in Evers et al. (2018b), that yields superior estimation accuracy over the LPM while maintaining linearity in the parameters. Although thermomechanical interactions are increasingly relevant, the modeling of this behavior in view of control is a key challenge. And although estimating FRFs using a local modeling approach shows promising results by suppressing the transients, these techniques are not yet applied to thermal dynamics in precision motion systems. The methods are mainly developed and applied on (lightly damped) mechanical systems, see, e.g., Van Keulen et al. (2017); Voorhoeve et al. (2018). Important aspects such as excitation signal design, transient measurement conditions and ambient disturbance reduction need to be re-evaluated.

To improve low frequency estimation quality of the FRF, a measurement of the ambient air temperature is used as an additional uncontrollable excitation input in the identification procedure. It is shown that by utilizing the additional excitation, mainly present at lower frequencies, the estimation quality of the FRF can be significantly improved. Comparable approaches in the mechanical domain have been explored in an active vibration isolation application (Beijen et al., 2018), using ground vibrations.

For some applications, e.g., direct feedback of a fast thermal system in Atsumi et al. (2013), models based on curve fitting a frequency response function can be sufficient. The application considered in this chapter requires a more extensive model. Therefore, a first principles lumped-mass modeling approach (Van der Sanden et al., 2007; Touzelbaev et al., 2013) is adopted in conjunction with frequency response function parameter calibration to obtain a predictive model of sufficient complexity.

Although FRF identification is well-developed for mechatronic systems from the electromechanical perspective, at present these techniques are not tailored towards identifying accurate thermal models for precision control. The aim of this chapter is to develop a framework for advanced identification, particularly suitable for thermal-mechanical systems and to experimentally validate this approach on a representative experimental setup.

This chapter builds on previous results reported in Evers et al. (2019b) and expands on these results with additional details and techniques providing a comprehensive framework. The main contributions of this chapter are:

C1 An overview of the significant challenges in thermal system identification,
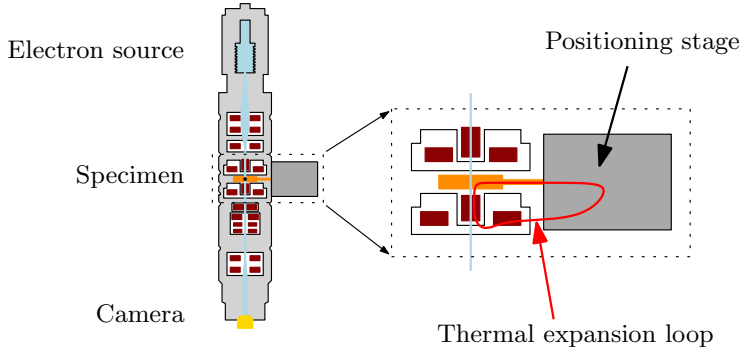
Figure 2.1. A general overview of a typical transmission electron microscope. The key component considered in this chapter is the sample holder stage. The expansion loop represents the collective thermal expansion of different components in the mechanical positioning stage assembly. Dominant heat sources in the system are the coils (▮) that are used to shape the electron beam.

illustrated on a representative experimental setup.

C2 Application of a new FRF identification approach that facilitates identification under transient conditions.

C3 Exploiting additional temperature measurement to reduce the low-frequency estimation error by explicitly including ambient air temperature fluctuations in the identification process.

C4 Estimation of a temperature dependent convection coefficient to improve model quality over a large temperature range.

C5 An extensive case study, leveraging the improved FRF identification results to calibrate model parameters yielding a high-fidelity parametric model.

2.2. Thermal system identification: challenges and problem formulation

In this section, an overview of the challenges in thermal system identification for precision motion systems is given. Moreover, the experimental setup that serves as a representative case study to illustrate the significance of these challenges is presented. The setup also provides a suitable experimental platform for the application of improved identification techniques.

2.2.1. Industrial challenges

Deformations induced by thermal gradients are increasingly relevant in several industrial applications, see, e.g, Evers et al. (2019a) for a selection. Examples

include, warping and wafer edge deformation in lithography applications, thermally induced drift in Transmission Electron Microscopy (TEM) (Tarău et al., 2011), see Figure 2.1, and frame deformations in machine tools (Koevoets et al., 2007; Weck et al., 1995). While the full temperature field is relevant for the prediction of thermally induced deformations, the expansion is often most relevant in a single Degree of Freedom (DOF). In this chapter, it is assumed that many industrial applications can be considered in one dimension (1D) such that the geometry can be simplified without loss of generality. This simplification is valid for many industrial applications where the thermal behavior is often analyzed in 1D, e.g., in the tool-path direction in machine tools (Weck et al., 1995) or perpendicular to the electron beam in TEM applications (Evers et al., 2019a), e.g., the expansion loop shown in Figure 2.1.

2.2.2. Problem formulation

2.2.2.1 Experimental setup: In this section the experimental setup is presented. The setup consist of a round uniform cylinder with a length of 250 mm and a diameter of 25 mm. The system has two heat inputs u_1, u_2 and five temperature outputs $T_{1,...,5}$, in the form of power resistors and negative thermal coefficient (NTC) thermistors respectively. A photograph of the experimental setup including its inputs and outputs is shown in Figure 2.2. The experimental setup consists of two aluminium cylinders with a small piece polyoxymethylene (POM) in between that acts as a high thermal resistance, as displayed in Figure 2.2. This setup represents a typical industrial use case, where commonly mixed-material system designs are used. Typically, thermal properties of aluminum are accurately known, however, the thermal conductivity of POM is often an uncertain parameter. The conductivity of POM varies between 0.22 to 0.39 W/mK at 20°C depending on the manufacturing process of the material. Accurately identifying the conductivity parameter value provides an excellent benchmark for a grey-box parameter estimation problem.

2.2.2.2 Transient response: Thermal actuators are often limited to positive input signals or to binary sequences (Monteyne et al., 2013), e.g., the power resistors in Figure 2.2 can only apply a positive thermal flux. As a result of this positive flux, the temperature of the system increases, causing components in the system to expand. This could exceed the measurable temperature or deformation range. Especially with systems with multiple inputs, where the applied heat input is cumulative. The design of thermal excitation signals should have a low mean input while the input spectra remains rich. Designing optimal excitation signals remains a challenge for accurate FRF estimation.

Conventional approaches to frequency response function identification are typically unable to cope with large transients present in the response. These transients are, e.g., a result of the offset in the input or initial system condi-
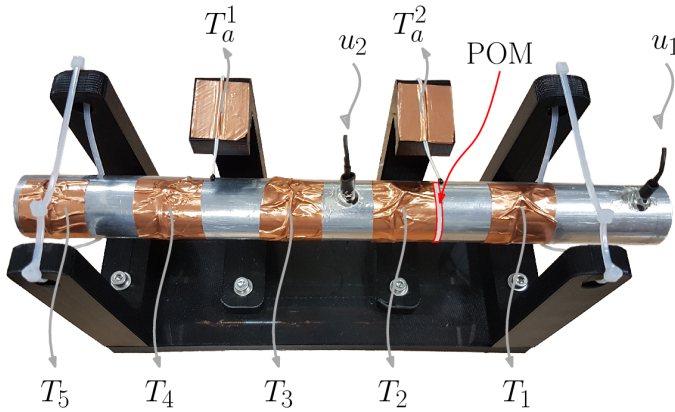
Figure 2.2. The experimental setup used in this chapter. It consists of an aluminium cylinder with two heater inputs (u_1, u_2), five temperature sensors $(T_{1,...,5})$, and two ambient temperature sensors $(T_a^{1,2})$.

tions. Commonly, the measurement data obtained under transient conditions is discarded in the identification process leading to loss of usable data. Moreover, due to the slow dynamics of thermal systems, removing this initial transient leads to an unacceptable increase of experiment time. In this chapter, a novel approach to FRF identification is applied, first described in Evers et al. (2018a), that is suitable for FRF identification under transient conditions. This facilitates a reduced experiment time by eliminating the need for transient data removal and improves the overall estimation quality by removing the bias caused by the transient contribution.

2.2.2.3 Environmental disturbances: The response of thermal systems is highly influenced by environmental disturbances, consequently the identification accuracy often deteriorates. Typically, these environmental disturbances are dominated by day/night cycles or fluctuations in thermal conditioning systems, e.g., water chillers, which have relatively slow dynamics. As a consequence, the disturbance spectrum is relatively large at low frequencies and converges to a typical flat spectrum at higher frequencies, this is sometimes referred to as $1/f$ noise (Ninness, Jan./1998). This is illustrated in Figure 2.3 where a measured spectrum of the ambient air temperature surrounding the experimental setup is shown.

Specific limited time frames in the day/night cycle, e.g., at night, have relatively little environmental disturbances, however performing experiments at these specific time frames is not always viable. Reducing the impact of environ-
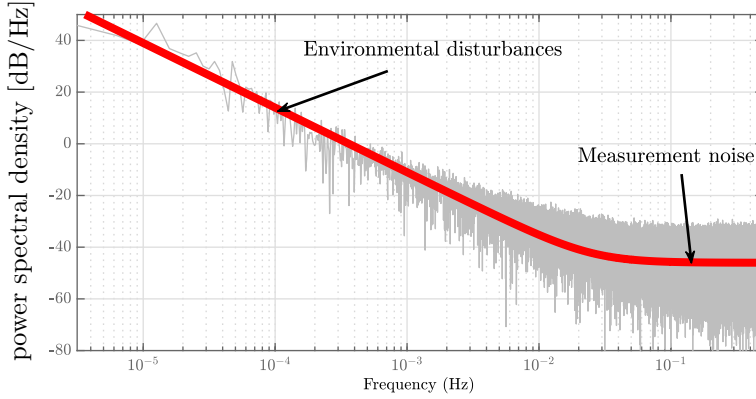
Figure 2.3. A typical power spectral density of the temperature of the ambient air surrounding the experimental setup. Illustrating the low-frequency ambient disturbances and high frequency measurement noise.

mental disturbances is needed to increase the estimation accuracy and to reduce the experiment time. In this chapter, an approach is used where the ambient temperature measurement, taken by sensors shown as T_a^1, T_a^2 in Figure 2.2, is taken as an additional system input. This provides additional information for the system identification problem, and can increase the estimation accuracy, specifically at low frequencies.

2.2.2.4 Parameter varying dynamics: Typically, the assumption of linear time invariant (LTI) for thermal systems is only valid around a certain temperature. Realistically, the convection is expected to vary even within a relatively small temperature range (Bergman, 2011). For larger temperature ranges, the system behavior is nonlinear, and can be modeled as a linear parameter varying (LPV) system (Shamma, 2012). Typically, the convection coefficient only significantly alters the low frequency response of the system, resulting in a change in the largest time constant. Typically, the relation between temperature and the convection coefficient is described empirically (Morgan, 1975) based on the geometry of the setup and properties of the fluid medium, e.g., air. In this chapter, an approach is shown where this empirical relation is estimated for different operating conditions, allowing it to be included in the model as a temperature dependent parameter.

2.2.2.5 Problem formulation: In precision motion control thermomechanical interactions are increasingly relevant, yet the modeling of this behavior in view of control is a key challenge. To obtain an accurate system model it is key to take into account 1) transient contributions 2) environmental disturbances

and 3) temperature dependency of the parameters. In this chapter, estimating the FRF is taken as a first step towards high-fidelity modeling. The estimated FRF can be used directly, e.g., for controller tuning (Karimi and Zhu, 2014). In this work, the FRF is used as a basis for a grey-box approach to calibrate model parameters based on experimental data gathered under transient conditions. This facilitates the use of high-fidelity models for advanced model based control, enabling further advances in precision motion control.

2.3. Improved thermal system identification

In this section, an improved approach to identification of non-parametric frequency response functions in view of thermodynamics in mechatronic systems is presented.

2.3.1. Non-parametric frequency response function

Consider a causal linear time invariant (LTI) system in an open-loop identification setting as shown in Figure 2.4. Throughout, the excitation signal $u(n)$ is assumed to be a random phase multisine. Commonly, multisine signals are being used as a periodic excitation since their spectrum is deterministic (Ljung, 1999; Pintelon and Schoukens, 2012).

Definition 2.1. *In this chapter, a Random Phase Multisine (RPMS) signal is defined as*

$$u(n) = \sum_{k=1}^{N} A_k \sin(2\pi f_k n/N + \phi_k) + \Delta, \qquad (2.1)$$

where, n is a specific discrete sample, N is the total number of samples, A_k is the amplitude of the sinusoidal signal at frequency f_k, ϕ_k is a uniformly distributed random phase on $[0, 2\pi)$ such that $\mathbb{E}\{e^{i\phi_k}\} = 0$ and Δ is an offset to enforce $u(t) \geq 0$.

These multisine excitation signals offer the possibility to tune their frequency content by adjusting A_k, and due their periodic nature spectral leakage due to the excitation input can be minimized. Different possible realizations of multisine signals are presented in Geerardyn (2016), e.g., using a linear or logarithmic power distribution to maximize the amplitude spectrum of the excitation signal. The response $y(n)$ to input $u(n)$ of a discrete LTI system is as follows

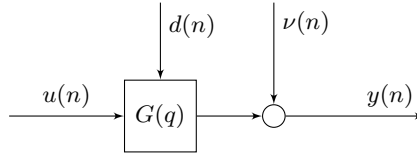$$y(n) = \sum_{m=-\infty}^{\infty} g(n-m)u(m) + \nu(n), \qquad (2.2)$$

Figure 2.4. Discrete time linear dynamical open-loop system with input $u(n)$, environmental disturbance $d(n)$, measurement noise $\nu(n)$, and output $y(n)$.

with $g(n)$ the impulse response of the system and $\nu(n)$ the additive noise contribution. The Discrete Fourier Transform (DFT) of a signal is given by

$$X(k) = \frac{1}{\sqrt{N}} \sum_{n=0}^{N-1} x(n) e^{-j2\pi nk/N}. \tag{2.3}$$

Applying the DFT to (2.2) results in

$$Y(k) = G(\Omega_k)U(k) + \mathcal{T}(\Omega_k) + \mathcal{V}(k). \tag{2.4}$$

Here, $\Omega_k = e^{-j2\pi nk/N}$ and $Y(k)$, $U(k)$, $\mathcal{V}(k)$ are the DFT of $y(n)$, $u(n)$, $\nu(n)$ respectively, $G(\Omega_k)$ is the frequency response function of the dynamic system, and k denotes the kth frequency bin. Here, $\mathcal{T}(\Omega_k)$ represents the combination of the system and noise transient terms. These transients are the result of the truncation of an infinite response to a finite measurement interval.

Traditionally, the empirical transfer function estimation (ETFE) is used to derive the FRF (Ljung, 1999; Pintelon and Schoukens, 2012). The ETFE is defined as

$$\begin{aligned}
\hat{G}(\Omega_k) &= Y(k)U(k)^{-1}, \\
&= G(\Omega_k) + \underbrace{\underbrace{\mathcal{T}(\Omega_k)U(k)^{-1}}_{\text{Transient}} + \underbrace{\mathcal{V}(k)U(k)^{-1}}_{\text{Noise}}}_{\text{Estimation error}}
\end{aligned} \tag{2.5}$$

For thermal systems, the transient contribution is significant. While the ETFE can often yield acceptable results on mechanical systems, since the transient is significantly shorter than the measurement period, for thermal systems the estimation accuracy is severely biased due to the transient component in the estimation error in (2.5). In view of existing system identification methods, this poses additional challenges, since these methods often assume the transient component to be negligible. In this chapter, a method is proposed that explicitly takes these transients into account during the identification procedure. This method is also applicable to a more general class of systems.

2.3.2. Transient elimination

To cope with data gathered under transient conditions, a local modeling method is adopted. This method, see also Evers et al. (2018a) and Chapter 4 of this thesis, uses a local rational parameterization of $G(\Omega_k)$ and $T(\Omega_k)$ in (2.4) on a subset of points

$$\lambda = \{\{k - l, \ldots, k + l\}|\lambda \neq k\} \subset \mathbb{N}, \tag{2.6}$$

i.e., a local window of width $2l + 1$ with $l \in \mathbb{N}$, in the complex plane. Consider again (2.5) and let

$$G(\Omega_\lambda) = \sum_{b=0}^{N_b} \theta_G^k(b)\Psi(b, \lambda) \tag{2.7}$$

$$T(\Omega_\lambda) = \sum_{b=0}^{N_b} \theta_T^k(b)\Psi(b, \lambda), \tag{2.8}$$

such that locally the terms in (2.5) are approximated in a local window λ by an expansion of degree N_b using general basis functions $\Psi(\lambda) \in \mathbb{C}$ where $\theta_G^k(b) \in \mathbb{C}$ and $\theta_T^k(b) \in \mathbb{C}$ are the local coefficients for the plant and transient respectively. An identical basis function is used for the system and transient estimation as the dynamics are the same. This parameterization is linear in the parameters, i.e., θ can be obtained in a closed-form solution, while having the advantages of using a general basis Ψ that allows for user-chosen parameterizations. For instance, the basis Ψ can be chosen to be a polynomial, rational, or fractional function of the window parameter λ. Moreover, the basis straightforwardly allows for the inclusion of prior knowledge on the system dynamics through pre-scribed poles in Ψ.

Generally, thermal systems are described by Partial Differential Equations (PDEs) that have no finite order. After spatial discretization they can be described by a finite set of first order Ordinary Differential Equations (ODEs) with inherently stable poles. Commonly, a first estimation of the time constants of the system can be made and included as prior knowledge through Ψ to improve the estimation error of the FRF, see, e.g., Evers et al. (2018b).

2.3.3. Incorporating additional inputs

One of the main environmental disturbances for thermal systems is ambient air temperature fluctuations. To reduce the effect of these fluctuations on the FRF identification, measurements of the ambient temperature are incorporated as an additional input (Ljung, 1999). Since it is difficult to excite the ambient air temperature in this chapter it is considered an uncontrollable additional input. Measuring the environment and treating it like an input is commonly done for identifying vibration isolation systems, e.g., using ground vibrations as additional excitation sources (Beijen et al., 2018).

The temperature of the environment is spatially dependent, and therefore ambient temperature measurements are only valid under the assumption that the ambient temperature surrounding the experimental setup is relatively uniform. The measured ambient air temperature is incorporated as an additional input in the identification procedure, yielding

$$Y(k) = \tilde{G}(\Omega_k) \begin{bmatrix} U(k) \\ \tilde{D}(k) \end{bmatrix} + \mathcal{T}(\Omega_k) + \mathcal{V}(k) \tag{2.9}$$

where $\tilde{D}(k)$ is the DFT of the measured environmental temperature. Here, $\tilde{G}$ is now a 1×2 multi-variable system model due to the additional system input. The augmented plant $\tilde{G}$ can now straightforwardly be estimated through the procedure described in Section 2.3.2.

2.4. Thermal modeling: parametric model applications

In this section, an approach to lumped-parameter parametric modeling for thermal systems is presented. Moreover, it is shown that the improved FRF obtained by applying the approach presented in Section 2.3 facilitates a grey-box parameter estimation approach. Lastly, a preliminary approach for identification of a temperature dependent convection coefficient is described.

2.4.1. Thermal modeling

Consider a thermal system, e.g., the setup in Section 2.2.2.1, where the thermal dynamics are described by the heat equation

$$c_p(x)\rho(x)\frac{\partial T(x,t)}{\partial t} = \frac{\partial}{\partial x}\left(\kappa(x)\frac{\partial T(x,t)}{\partial x} + h\big(T(x,t) - T_\infty(t)\big)\right) + Q(x,t). \tag{2.10}$$

With $T(x,t)$ the temperature at position x, $T_\infty(t)$ the ambient temperature, $Q(x,t)$ the heat flux, h the convection coefficient, $\kappa(x)$ the thermal conductivity, $\rho(x)$ the material density, and $c_p(x)$ the specific heat capacity. The heat transfer due to radiation is linearized and combined in the convection coefficient h. By employing spatial discretization, shown in Figure 2.5, the PDE in (2.10) is transformed into a set of ODEs and the parameterized model can be represented in state space form by

$$\begin{aligned} \dot{T}(t) &= A(\varphi)T(t) + B(\varphi)u(t) \\ y(t) &= C(\varphi)T(t) \end{aligned} \tag{2.11}$$

where $\varphi \in \mathbb{R}^{N_p \times 1}$ is a parameter set with N_p number of parameters including, but not limited to, material constants and contact resistances.
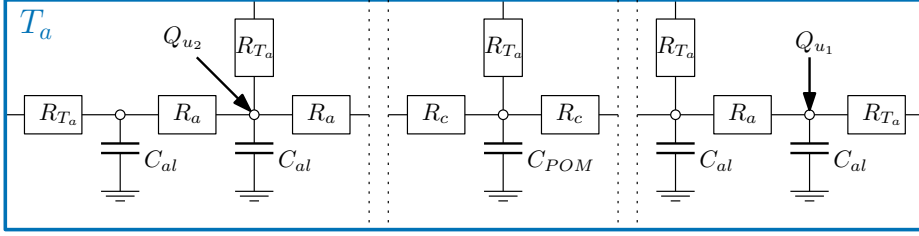
Figure 2.5. An illustration of the lumped-mass discretization of the experimental setup. The setup is divided into lumps, represented as capacitances C, that are interconnected to each other and the ambient temperature T_a by resistances R. The actuator inputs are represented as a heat flux $Q_{u_{1,2}}$ entering the appropriate lump. The dashed lines indicate a repeating pattern of the appropriate lumps, the illustration is simplified to facilitate the presentation.

2.4.2. Grey-box identification

The parameterized model (2.11) contains uncertain parameters φ that limit the prediction accuracy and suitability for advanced control. The aim of grey-box identification is to calibrate the parameter set φ such that the model (2.11) yields an accurate representation of the real system. The grey-box approach is based on minimizing the discrepancy between the measured non-parametric FRF and the FRF of the parametric model with the following cost function

$$\mathcal{J} = \min_{\varphi}\Big\{\|W(\Omega_k)\Big(G(\Omega_k) - \hat{G}(\Omega_k, \varphi)\Big)\|_2^2\Big\}. \qquad (2.12)$$

Here, $\hat{G}(\Omega_k)$ is the measured non-parametric FRF obtained by applying the approach presented in Section 2.3, $G(\Omega_k, \varphi) = C(\varphi)(\Omega_k I - A(\varphi))^{-1}B(\varphi)$ is the FRF of the parametric model (2.11), $W(\Omega_k) \in \mathbb{C}^{N_y \times N_u}$ is a dynamic weighting filter depending on the variance of the FRF at each frequency, and N_u and N_y are the number of inputs and outputs, respectively. By minimizing (2.12) the parameter set φ is calibrated such that the model (2.11) best describes the experimental system. This facilitates the use of the calibrated model for advanced control and error compensation techniques.

2.4.3. Non-linear convection coefficient estimation

In this section, a procedure is proposed to estimate the temperature dependent convection coefficient. The convection coefficient is often assumed to be constant in a small temperature range. However, realistically, the convection coefficient depends, among others, on the temperature difference between the aluminium bar and its surroundings, $\Delta T = T(x,t) - T_\infty(t)$ (Bergman, 2011) and therefore varies with temperature. To accurately capture larger temperature variations,

this coefficient needs to be estimated for a wide temperature range. The empirical relation between the convection coefficient and ΔT can be estimated, under the assumptions that the Rayleigh number is linear in terms of ΔT and the Prandtl number is constant, by

$$h(\Delta T) = a + b\Delta T^c \tag{2.13}$$

where a, b, c are model parameters. Here, it is proposed to apply a staircase function to the input. Due to the constant input, the temperature converges to a steady state for various ΔT. Next, for each steady state temperature, the convection coefficient is estimated by minimizing the error between the measured and simulated output.

> **Remark**
>
> Typically, the convection coefficient is also dependent on the specific geometry of the boundary surface, making it spatially varying. A possible simplification approach is to approximate the coefficient through empirical relations that are determined for common geometric shapes, see, e.g., Bergman (2011); Morgan (1975). A spatially varying convection coefficient is considered outside the scope of this thesis.

2.5. Case study: from measurement to model

In this section, the proposed identification methodology is applied to the experimental setup presented in Section 2.2.2.1 to yield a high-fidelity parametric model.

2.5.1. Measurement: obtaining the FRF

In this section, the FRF of the experimental setup is estimated by using 1) transient suppression techniques as presented in Section 2.3.2 and 2) incorporation of additional inputs, presented in Section 2.3.3, to improve low-frequency estimation.

2.5.1.1 Transient suppression: Since the input to the system is constrained to be positive, the excitation input $u_1(t)$ is selected as a RPMS with offset, see Def. 2.1 for a definition. The temperature response T_1 to the input u_1 is shown in Figure 2.6. Initially, the temperature response consist of a first order step response due to the offset Δ in the excitation signal. After the initial transient has settled, the output consists of the response of the excitation signal and environmental disturbances.

   Two sub-records of the same dataset are considered, one includes the first two periods, which consist of a significant initial transient, and environmental
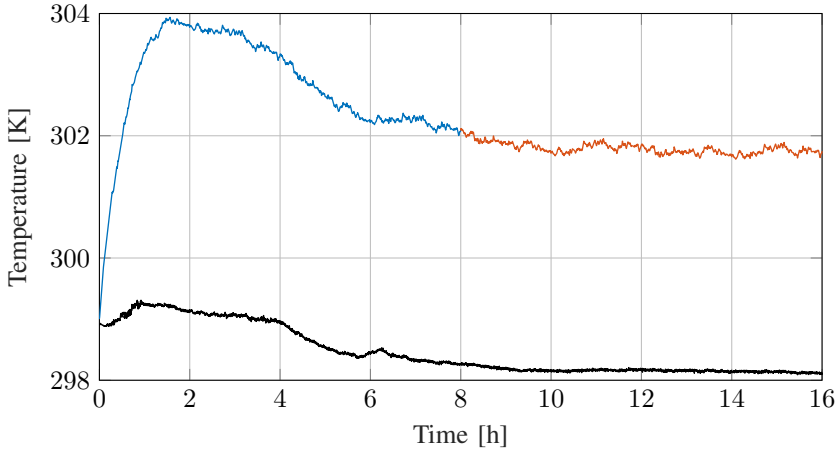
Figure 2.6. Temperature response $u_1 \rightarrow T_1$ of the experimental setup to a random phase multi-sine with offset for 4 periods of each 4 [h]. The dataset is divided into two sub-records, sub-record 1 (—) contains the majority of the initial transient and ambient temperature (—), and sub-record 2 (—) contains significantly less initial transient.

disturbances. The second sub-record consist of the last two periods with a reduced transient and environmental disturbance and is used as a validation dataset.

In Figure 2.7 the FRF estimation using sub-record 1 is shown. Clearly, the ETFE is unable to estimate the dynamics correctly using sub-record 1 since the transient contribution is relatively large. The LRMP estimates and suppresses the transient $\mathcal{T}(\Omega_k)$ and is invariant to significant transients in the response. As a result, the estimation error of the FRF $\hat{G}(\Omega_k)$ is improved by using the LRMP when compared to the validation data.

2.5.1.2   Incorporating additional inputs: In this section a measurement of the ambient temperature T_∞ is used as an additional excitation input, see (2.9), to improve the estimation accuracy at low-frequencies. The procedure yields an estimate for a 1×2 plant model

$$\tilde{G}(\Omega_k) = [G(\Omega_k)_{u_1 \rightarrow T_1}, G(\Omega_k)_{T_\infty \rightarrow T_1}] \tag{2.14}$$

containing the transfer function between the input u_1 and T_1, i.e., the desired FRF, and the transfer function between T_∞ and T_1, where the latter can be used for a disturbance sensitivity analysis.

In Figure 2.8, the amplitude estimation of the FRF $G(\Omega_k)_{u_1 \rightarrow T_1}$ and the 3σ uncertainty bounds are shown. The results show the estimation using only the
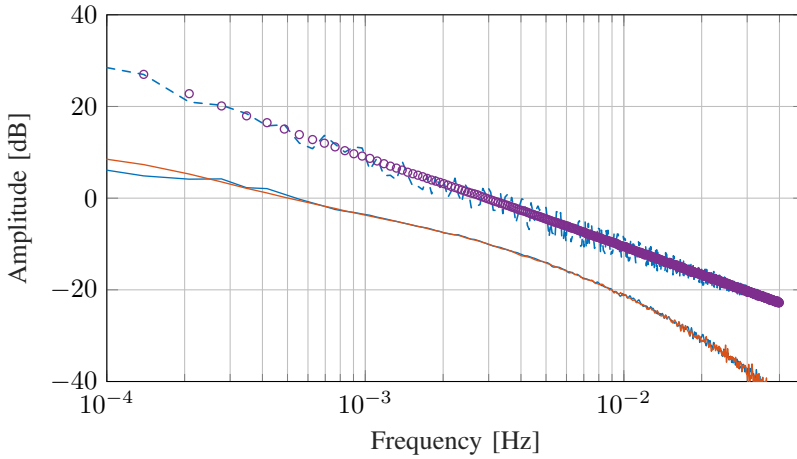
Figure 2.7. FRF estimation of $u_1 \to T_1$ using ETFE and LRMP from sub-record 1 in Figure 2.6. It shows that the LRMP (—) unlike the ETFE (- -), is invariant to the transient contribution (○) and provides a good estimate when compared to the validation data (—) obtained from sub-record 2 in Figure 2.6.
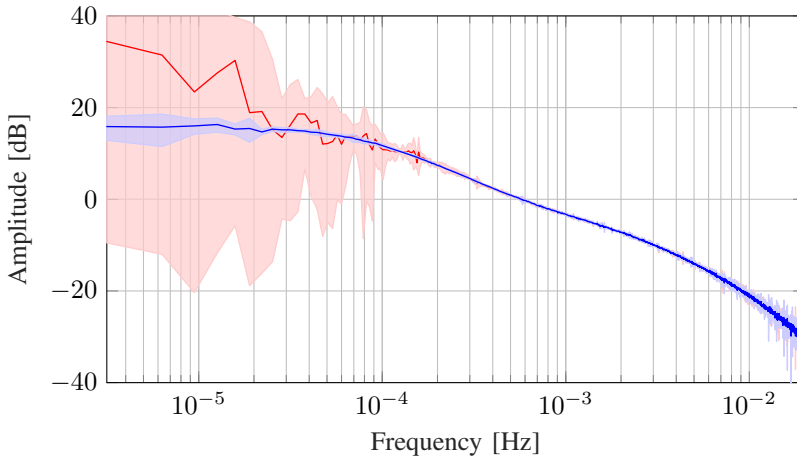
Figure 2.8. FRF estimation of $u_1 \to T_1$ using (a) LRMP with only input u_1 (—) and (b) using the additional input (—). By incorporating the additional input the variance, shown as (■,■), is significantly reduced at low frequencies.

input u_1, shown in red (a), and using u_1 and the ambient temperature measurements as an additional input, shown in blue (b). The amplitude estimation and variance at medium to high frequencies are similar for both estimations. However, using only the input u_1 a large variance is obtained in the low frequency region. By then incorporating the ambient measurement as an additional input, the variance of the estimation of the FRF is reduced significantly.

2

Figure 2.9. Non-parametric FRF estimate (●) of the experimental setup and the 3σ estimation uncertainty (▨). The FRF is used for a grey-box parameter estimation, yielding a high-fidelity parametric model (—).

2.5.2. Model: parametric modeling and simulation

In this section, facilitated by the improved FRF obtained in Section 2.5.1, a high-fidelity parametric model of the experimental setup is constructed.

2.5.2.1   Parameter estimation: In this section, the parameters of a Multi-Input Multi-Output (MIMO) lumped mass model, i.e., a model in the form (2.11), are calibrated by minimizing the discrepancy between the parametric model and the non-parametric FRF estimation using (2.12). The parameters that are optimized include, but are not limited to, the conduction coefficient, contact resistances and material properties of the aluminum and POM. In Figure 2.9 the estimated non-parametric FRF, estimated at a temperature of approximately 300 [K], and the calibrated parametric model, is shown. Clearly, the estimated parametric model is within the 3σ 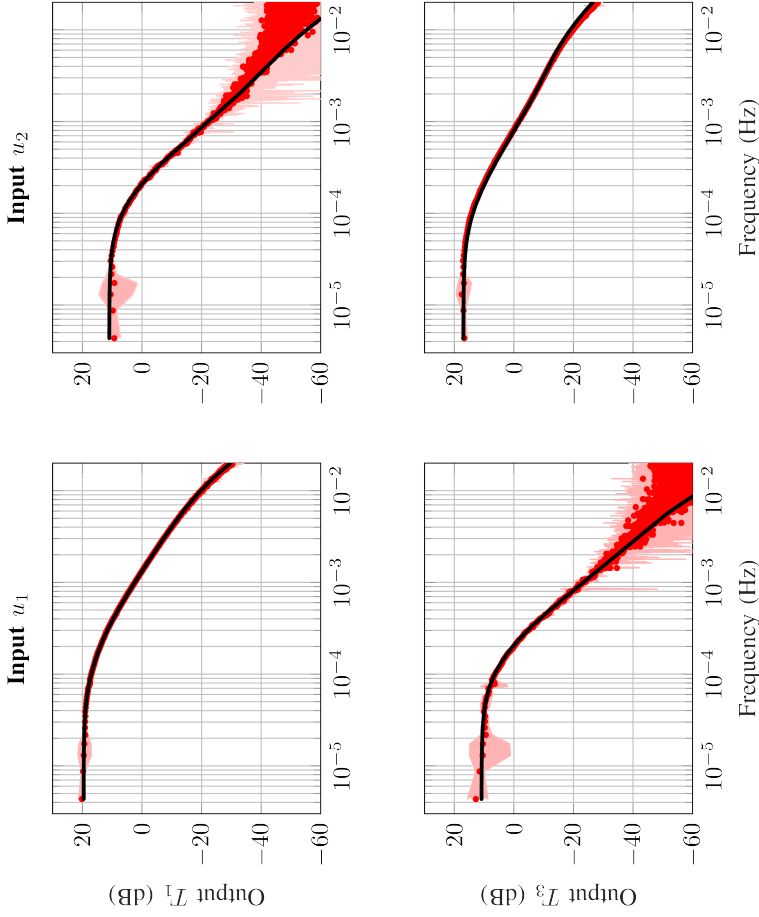uncertainty of the FRF estimation. The conductivity of the slice of POM material is estimated at 0.32 W/mK, which is well within the range supplied by the manufacturer. The procedure yields a MIMO high-fidelity parametric model of the experimental system.

2.5.2.2   Estimating the convection coefficient: The method proposed in Section 2.4.3 is applied to the experimental setup. The system is excited using a staircase function with a step gain of 0.05 W and a step time of 5 hours. The response and input signal are shown in Figure 2.10. Clearly, the temperature response suffers from ambient temperature fluctuations. At each steady state, in terms of the heat input, the error between temperature simulation and measurement is minimized by tuning the convection coefficient. The convection coefficient is found for various ΔT. An temperature dependent function is derived by fitting (2.13) onto the evaluated points from the experiment in a least squares manner, yielding results as shown in Figure 2.11.

2.5.2.3   Time domain validation: By applying the framework presented in this chapter a high-fidelity parametric model is obtained. This model can be used for various objectives, e.g., controller design or predictive simulation studies. The predictive accuracy of the model is validated by using a step response measurement using heater input u_1. A step response of 0.5 [W] is applied to u_1, at $t = 1$ [h], and the simulated response of T_1 and T_2 is compared to the measured response as shown in Figure 2.12(top). The results clearly show the high thermal resistance of the POM, located between u_1 and T_2, indicated by a slower response when compared to T_1. It is seen that by utilizing the procedure presented in this chapter a high-fidelity model is obtained as illustrated by the small prediction error shown in Figure 2.12(bottom). While the results for the experimental setup are not yet in the millikelvin range, it is expected that the presented approach scales well to more sophisticated hardware.
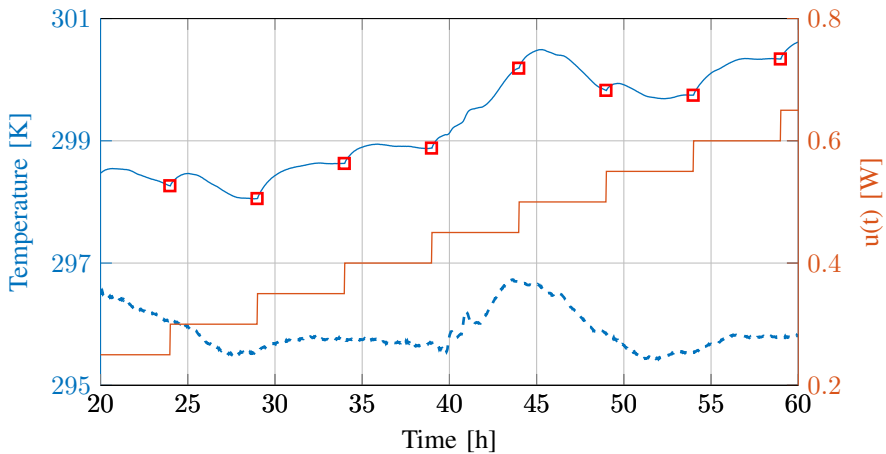
Figure 2.10. Experimental data used to estimate the temperature dependent convection coefficient. The heater input (—) is applied in a stair sequence. The resulting temperature (—) is then evaluated at specific points (□). The ambient temperature (- -) is recorded and taken into account.
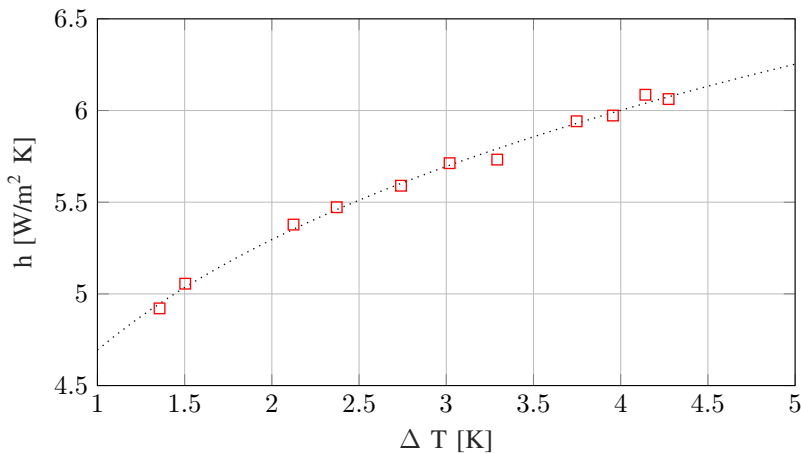
Figure 2.11. Estimated empirical function (····) and calculated convection coefficients (□) from Fig. 2.10 describing the temperature dependency of the convection coefficient.
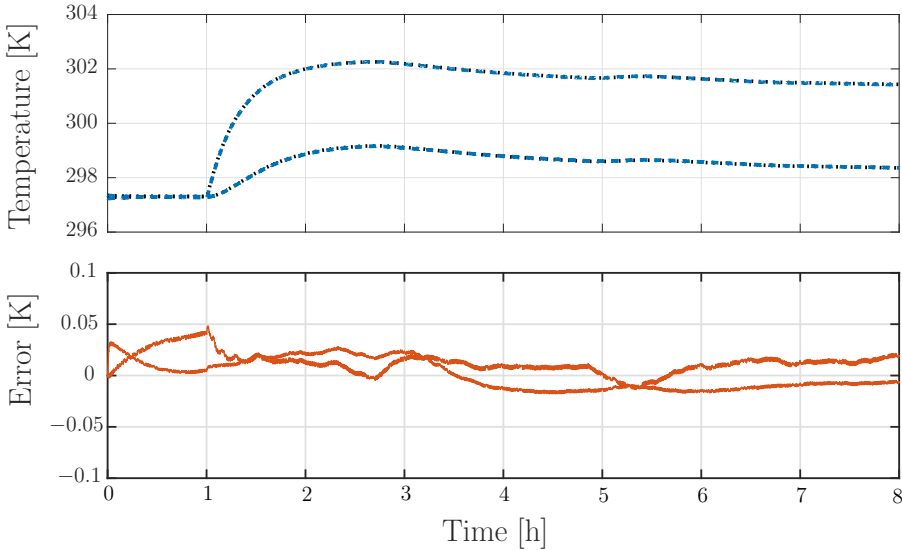
Figure 2.12. Time domain validation experiment on the parametric model obtained using the framework presented in this chapter. In the top figure, the simulated (- - -) is compared to the measured (····) output. In the bottom figure, the simulation error (—) is shown for both outputs.

2.6. Conclusion

The modeling approach presented in this chapter enables fast and accurate modeling of thermal dynamics in view of precision motion control. By applying the local parametric method an improved non-parametric FRF estimate is obtained. Furthermore, by explicitly taking into account the transient contributions a significant reduction in measurement time is achieved when compared to classical methods. Moreover, the estimation error for low-frequencies is significantly reduced by incorporating additional sensor data that makes use of environmental disturbances to provide additional excitation input. Building on the improved FRF estimation, a grey-box parameter calibration approach is presented that yields high-fidelity parametric models of the thermodynamical system. The proposed methodology is applied to a multi-variable experimental setup. The method achieves significant improvements in estimation accuracy, and a reduced experimentation time by incorporating the transient and disturbance contributions. The presented methods form a framework that facilitates the implementation of advanced control techniques and error compensation strategies, enabling increased accuracy and throughput in high precision motion control.

On Frequency Response Function Identification for Advanced Motion Control [1]

Abstract: A key step in control of precision mechatronic systems is Frequency Response Function (FRF) identification. The aim of this chapter is to illustrate relevant developments and solutions for FRF identification. Specifically dealing with transient and/or closed-loop conditions that can normally lead to inaccurate estimation results. This yields essential insights for FRF identification that are illustrated through a simulation study and validated on an experimental setup. Although the chapter is set in an advanced motion control context the demonstrated principles can be straightforwardly translated to a thermomechanical setting.

---

[1]The results in this chapter constitute Contribution C2 of this thesis. The chapter is based on "Evers, E., Voorhoeve, R., and Oomen, T. On Frequency Response Function Identification for Advanced Motion Control, IEEE 16th International Workshop on Advanced Motion Control (AMC2020) - Kristiansand, Norway, 2020" .

3.1. Introduction

Many mechatronic systems in the manufacturing industry are considered as Multiple-Input Multiple-Output (MIMO) systems in view of control. These systems often have multiple Degrees of Freedom (DOF) that must be controlled using feedback control for various reasons, e.g., safety margins or constraints on movement range. Furthermore, there is an increasing need for the control of systems-of-systems (Evers et al., 2019c) where multiple subsystems jointly contribute to the overall system performance. Examples include wafer scanners used in the lithographic industry, where the wafer stage and reticle stage synchronization is critical to achieve the required overlay performance or gantry and carriage platforms such as large scale industrial printers (Blanken and Oomen, 2019), where performance of both subsystems is directly related to the print quality, and roll-to-roll processing plants, where synchronization between rolls is required for correct deposition of the layer material (Chen et al., 2016).

Due to the increasing complexity of these MIMO systems-of-systems appropriate modeling techniques are required. For this, acquiring the frequency response function (FRF) of the system is an important first step. FRF identification is often fast and inexpensive and provides an accurate representation of the system. The FRFs can be used for many applications, e.g., direct controller tuning (Karimi and Zhu, 2014) or as a basis for parametric modeling (Voorhoeve et al., 2016b).

The identification of FRFs has made significant progress in recent years, particularly by explicitly addressing transients errors (McKelvey and Guérin, 2012; Schoukens et al., 2009). Indeed, one of the underlying assumptions is that the system is in steady state, which is often not valid for experimental systems. Furthermore, these approaches have been extended to MIMO systems (Voorhoeve et al., 2018), but in MIMO identification for control, it is often ambiguous which closed-loop transfer functions have to be identified.

Although important progress is made in FRF identification, application of these advanced methods, especially for multivariable systems, is strikingly limited. The aim of this chapter is to provide a clear and concise overview of the steps and decisions that are taken during the identification process. Specifically, two items are investigated in more detail: 1) the elimination of transients and 2) closed-loop aspects for single and multivariable systems. The elimination of transients, i.e. aspect 1), is key when identifying complex systems with many inputs and outputs, commonly, an individual experiment is required for each separate input channel. An approach is presented that can explicitly estimate and remove transient components from FRF estimation that otherwise would cause a biased estimate. Traditionally, these transient effects are mitigated by increasing the experiment length and removal of the initial transient data. By applying the proposed method, a significant reduction in measurement time is achieved.
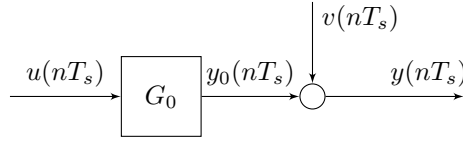
Figure 3.1. LTI discrete time system in an open-loop setup.

Moreover, closed-loop aspects, i.e., aspect 2), are highly important since these increasingly complex systems often operate in closed-loop conditions. Identification under these conditions is increasingly challenging since the additional feed-back loop can cause an estimation bias when not appropriately addressed. Furthermore, a distinction in view of system modeling for control must be made between full MIMO modeling or appropriate selection of a closed-loop Single-Input Single-Output (SISO) transfer function that includes the effect of the interaction between different DOFs.

3.2. Problem formulation

Consider the discrete time signal $u(nT_s)$, $n = 0, \ldots, N-1$, where N is the total amount of samples, and its frequency domain representation $U(k)$ obtained by application of the Discrete Fourier Transform (DFT) defined as (Pintelon and Schoukens, 2012):

$$X(k) = \frac{1}{\sqrt{N}} \sum_{n=0}^{N-1} x(nT_s) e^{-j2\pi nk/N}. \tag{3.1}$$

When the signal $u(nT_s)$ is applied as input to a linear time invariant system G_0 with additive output noise $v(nT_s)$, as in Figure 3.1, the resulting output in the frequency domain equals

$$Y(k) = G_0(\Omega_k)U(k) + T(\Omega_k) + V(k), \tag{3.2}$$

where $T(\Omega_k)$ represents the transient contribution and $V(k)$ represents the noise contribution. The argument Ω_k denotes the generalized frequency variable evaluated at DFT-bin k, which, when formulated in, e.g., the Laplace domain, becomes $\Omega_k = j\omega_k$ and in the Z-domain $\Omega_k = e^{j\omega_k T_s}$.

3.2.1. Problem formulation

In this chapter focus is placed on two aspects in particular, 1) transient contributions and 2) closed-loop aspects.

3.2.1.1   Transient contribution: The transient contribution consists of the additional signal that results from past inputs, minus the missed signal in the future response that results from final conditions in the current window. Provided that G_0 is proper, this yields the following state-space representation of the transient contribution

$$T(z^{-1}) = C(I - z^{-1}A)^{-1} \left(x(0) - x(N)\right). \tag{3.3}$$

where the initial state $x(0)$ and final state $x(N)$ capture the past and final conditions respectively. The additional term $T(\Omega_k)$ in (3.2) poses difficulties when identifying the system in transient conditions, i.e., when $x(0) \neq x(N)$. It is generally not possible to separate the forced and transient contribution in the obtained mixed output signal. In Section 3.3.3 a method is provided to alleviate these difficulties.

3.2.1.2   Closed-loop aspects: Consider again the setup in Figure 3.1, here u is assumed to be independent of y and noise free. Clearly, in a closed-loop setting, where $u = K(r - y)$, where K is the controller and r and y the reference and output respectively, this no longer holds since u and y are correlated. In view of identification, additional care has to be taken, as is shown in Section 3.5.

3.2.2. Experimental Setup

The challenges for FRF identification presented in this paper are demonstrated on an experimental setup or a representative simulation model. The experimental setup is shown in Figure 3.2 and it consists out of two DC motors interconnected by a flexible connection. The system is operated in closed-loop and is multivariable with high interaction terms, i.e., with strong cross-coupling between the two inputs and outputs.

A representative simulation model is constructed by considering the setup as two masses connected to each other and the fixed world by spring-damper elements, as shown in Figure 3.2b. The state-space model of the system is then given by

$$\dot{x} = \underbrace{\begin{bmatrix} 0 & 1 & 0 & 0 \\ -173 & -8 & 166 & 1.33 \\ 0 & 0 & 0 & 1 \\ 166 & 1.33 & -173 & -8 \end{bmatrix}}_{A} \begin{bmatrix} x_1 \\ x_2 \\ x_3 \\ x_4 \end{bmatrix} + \underbrace{\begin{bmatrix} 0 & 0 \\ 53 & 0 \\ 0 & 0 \\ 0 & 53 \end{bmatrix}}_{B} \begin{bmatrix} u_1 \\ u_2 \end{bmatrix} \tag{3.4}$$

$$y = \underbrace{\begin{bmatrix} 1 & 0 & 0 & 0 \\ 0 & 0 & 1 & 0 \end{bmatrix}}_{C} \begin{bmatrix} x_1 \\ x_2 \\ x_3 \\ x_4 \end{bmatrix} \tag{3.5}$$

(a)
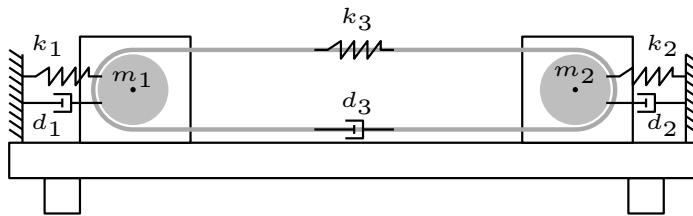
(b)

Figure 3.2. The experimental setup (a) and it's schematic counterpart (b). The system consists of two DC motors coupled by an elastic connection, often representative for a conveyor belt type system. Due to the direct connection between the motors, the system is highly multivariable.

where y [rad] is the angular position measured by optical encoders and u [V] is the input voltage to the linear amplifiers that control the motors. The transfer function matrix (TFM) can then by obtained by $G(s) = C(sI - A)^{-1}B$.

3.3. Estimators

In this section, various estimators for Frequency Response Functions (FRFs) are presented. Throughout, the SISO open-loop case is considered. The extension to closed-loop and MIMO is considered in Section 3.5 and Section 3.5.2 respectively.

3.3.1. Empirical Transfer Function Estimate

One of the most straightforward transfer function estimates can be obtained by simply dividing the frequency domain output signal with the input signal. This is known as the Empirical Transfer Function Estimate or ETFE, i.e.,

$$\hat{G}_{\mathrm{ETFE}}(k) = Y(k)/U(k). \tag{3.6}$$

To average out the noise contribution, the input and output signals are divided into windows of equal length and subsequently the ETFE is obtained for each window m to yield,

$$\hat{G}_{\mathrm{ETFE}}(k) = \frac{1}{M} \sum_m Y_m(k)/U_m(k). \tag{3.7}$$

When periodic excitation signals are used and the window length matches the periodicity of the excitation, this is an effective approach. However when arbitrary excitation signals are used such as noise excitation, averaging as performed in the ETFE can lead to poor results. This is due to the fact that when the excitation signal $u(nT_s)$ is a Gaussian (pseudo) random signal, the amplitude of $U(k)$ is also stochastic and can therefore be arbitrarily close to zero. When $U_m(k)$ is close to singular in some window m and at frequency bin k, the ETFE at that frequency will be dominated by the noise contribution yielding a very poor FRF estimate. This poor FRF estimate is subsequently averaged with the estimates in the other windows without accounting for the difference in the quality of the individual estimates.

The main guideline to follow is to always average out the noise before division. When this principle is directly applied for arbitrary signals by first averaging the inputs and outputs over all windows and then performing the division, i.e.,

$$\hat{G}_{\mathrm{avg}} = Y_{\mathrm{avg}}(k)/U_{\mathrm{avg}}(k), \tag{3.8}$$

with

$$Y_{\mathrm{avg}}(k) = \frac{1}{M} \sum_m Y_m(k), U_{\mathrm{avg}}(k) = \frac{1}{M} \sum_m U_m(k), \tag{3.9}$$

another problem occurs due to the randomness of the phases of $U_m(k)$ for each m. As these phases are random the mean value, i.e., $U_{\mathrm{avg}}(k)$, will tend to zero for large M.

3.3.2. Spectral Analysis

For arbitrary signals the spectral analysis approach is commonly applied. In this approach the cross-power spectrum of the input and output signals and

auto-power spectrum of the input signal are first calculated, involving an averaging step over all considered excitation windows, and subsequently the transfer function estimate is obtained by dividing these spectra

$$\hat{G}_{\text{SA}}(k) = \hat{\Phi}_{yu}(k)/\hat{\Phi}_{uu}(k) \tag{3.10}$$

where G_{SA} denotes the spectral analysis approach and

$$\hat{\Phi}_{yu}(k) = \frac{1}{M} \sum_m Y_m(k)U_m(k)^H \tag{3.11}$$

$$\hat{\Phi}_{uu}(k) = \frac{1}{M} \sum_m U_m(k)U_m(k)^H. \tag{3.12}$$

In this approach, transient suppression is achieved by using so called windowing functions, such as the Hanning window. For additional details, see Pintelon and Schoukens (2012, sections 2.2.3 & 2.6.5). An estimate for the noise covariance and the covariance on the transfer function estimate are obtained in spectral analysis through (Pintelon and Schoukens, 2012, eq. (7-33) & (7-42)).

$$\sigma_v^2(k) = \frac{M}{M - n_u} \left(\hat{\Phi}_{YY}(k) - \hat{\Phi}_{YU}(k)/\hat{\Phi}_{UU}(k)\hat{\Phi}_{YU}^H(k) \right) \tag{3.13}$$

$$\sigma_{G_{\text{SA}}}^2(k) = \frac{1}{M} \left(1/\hat{\Phi}_{UU}(k) \cdot C_v(k) \right) \tag{3.14}$$

3.3.3. Local Modeling Approach

The main idea of the local modeling approach, e.g., as in Schoukens et al. (2009), is to identify a model, with validity over only a small frequency range, which can be used to provide a non-parametric estimate of the FRF and the transient at the central point k. Consequently, errors due to the transient can be effectively eliminated. To achieve this, a small frequency window r around DFT-bin k is considered, i.e., $r = [-n_w, \dots, n_w] \in \mathbb{Z}$, to yield

$$Y(k+r) = G(\Omega_{k+r})U(k+r) + T(\Omega_{k+r}) + V(k+r). \tag{3.15}$$

Next, both the plant, $G(\Omega_{k+r})$, and the transient contribution, $T(\Omega_{k+r})$, which are assumed to be smooth functions of the frequency, are parametrized. For instance, using the polynomial parametrization

$$G(\Omega_{k+r}) = G(\Omega_k) + \sum_{s=1}^{R} g_s(k)r^s, \tag{3.16}$$

$$T(\Omega_{k+r}) = T(\Omega_k) + \sum_{s=1}^{R} t_s(k)r^s. \tag{3.17}$$

(a) Plant
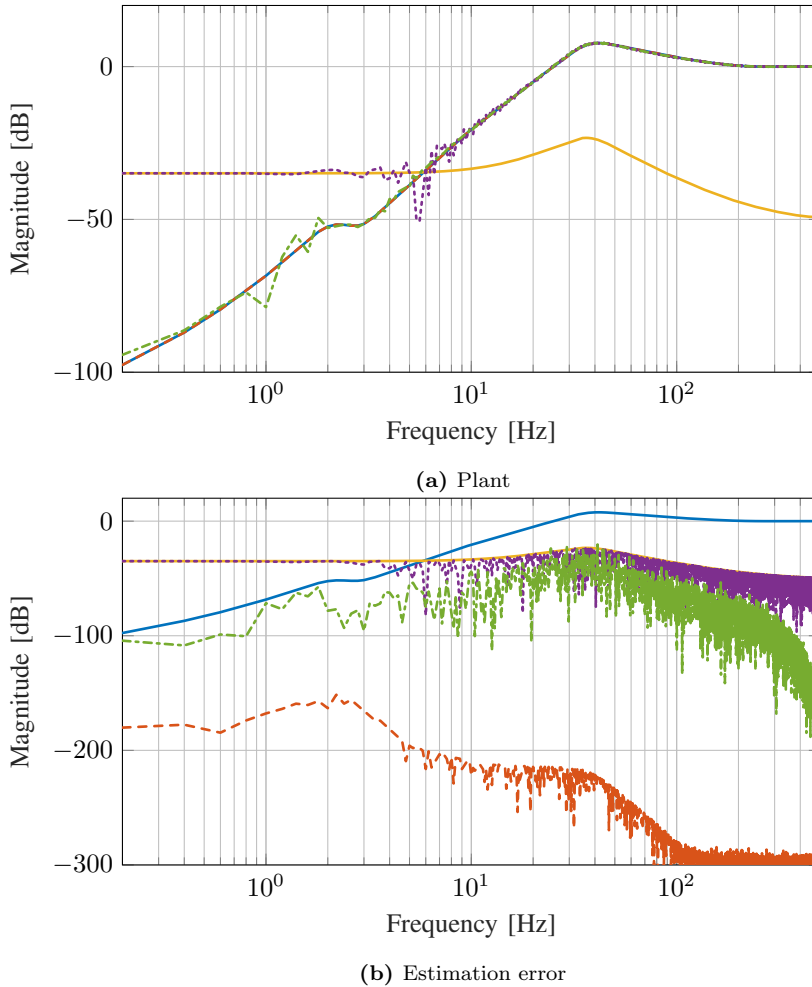
(b) Estimation error

Figure 3.3. Identification result under transient conditions, the top figure (a) shows the magnitude of the identified frequency response function and the bottom figure (b) shows its estimation error when compared to the model. The results show that the LPM (---), described in Sec.3.3.3, outperforms the spectral analysis method using both a rectangular (····) and a Hann (-·-) window. The LPM is invariant to the transient contribution (—) that dominates the response at lower frequencies when compared to the plant (—).

Using this parametrization (3.15) is rewritten as

$$Y(k+r) = \Theta(k)K(k+r) + V(k+r), \qquad (3.18)$$

with

$$\Theta(k) = \begin{bmatrix} \Theta_G(k) & \Theta_T(k) \end{bmatrix},$$
$$\Theta_G(k) = \begin{bmatrix} G(\Omega_k) & g_1(k) & g_2(k) & \dots & g_R(k) \end{bmatrix},$$
$$\Theta_T(k) = \begin{bmatrix} T(\Omega_k) & t_1(k) & t_2(k) & \dots & t_R(k) \end{bmatrix}, \qquad (3.19)$$

$$K(k+r) = \begin{bmatrix} K_1(r) \otimes U(k+r) \\ K_1(r) \end{bmatrix} \qquad (3.20)$$

where

$$K_1(r) = \begin{bmatrix} 1 & r & \cdots & r^R \end{bmatrix}^T. \qquad (3.21)$$

Finally, the parameters of the local model are determined by solving the linear least squares problem

$$\hat{\Theta}(k) = \underset{\Theta(k)}{\arg\min} \sum_{r=-n_W}^{n_W} \|Y(k+r) - \Theta(k)K(k+r)\|_2^2 \qquad (3.22)$$

$$= Y_n(k)K_n(k)^+ \qquad (3.23)$$

with $X_n(k) = \begin{bmatrix} X(k-n_W) & \cdots & X(k+n_W) \end{bmatrix}$, and with $A^+ = A^H(AA^H)^{-1}$ the right Moore-Penrose pseudo-inverse. Performing this least squares estimation for each DFT-bin, k, and evaluating the local models at the center frequency $r = 0$, yields a non-parametric estimate, $G(\Omega_k)$, for the FRF. For the parametrization described here this evaluation is trivial, since for $r = 0$ only the zeroth order polynomial term remains, which is why $G(\Omega_k)$ directly appears in this parametrization, see (3.16). It should be noted that this least squares estimation can be subject to certain weighting factors, as in, e.g., Voorhoeve et al. (2016a), which is true for any estimation problem considered in this paper. However, for clarity, such weighting factors have been omitted in the present chapter. An estimate for the covariance on the transfer function estimate can be obtained as provided in Schoukens et al. (2012, section 7.2.2.2).

3.4. Transients in System Identification

Estimating the true plant $G_0(\Omega_k)$ in (3.2) using classical estimators is challenging since the measurement of $Y(k)$ is contaminated with an additional component $T(k)$. In Section 3.3.3 it is shown that an explicit estimation of $T(k)$ can be made by constructing a local parametric model in a frequency window of width n around DFT bin k. The underlying assumption facilitating this approach is the smoothness of the transient component $T(k)$ in (3.3) since the transient is a decaying response, assuming that the system is stable.
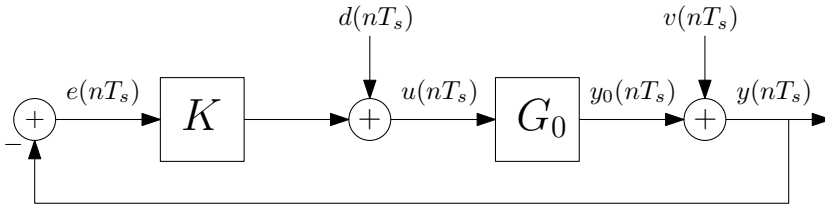
Figure 3.4. LTI discrete time system in a closed-loop setting.

Simulation study   To illustrate the benefit of the local modeling approach, a simulation study is performed using the simulation model presented in Section 3.2.2. The system G_0 is considered in closed-loop, see Figure 3.4, with identification input $d(nT_s)$ and identification output $u(nT_s)$. Therefore, the identification setting essentially is an open-loop one as in Figure 3.1, since the transfer function that is identified is the sensitivity function $S(\Omega_k) = \dfrac{u}{d}$, and d is noise free.

Simulation results   The excitation signal is 2 periods of a 5 [s] random phase multisine with a sampling frequency $F_s = 1000$ [Hz], resulting in a total of 10000 samples. The FRF of G_0 is then estimated using both the spectral analysis and local modeling approach, presented in Section 3.3, yielding results as shown in Figure 3.3. The spectral analysis method is applied using both a rectangular window and a Hann window. While the latter appears to achieve improved performance, the results are misleading, with increasing amount of periods, mitigating the effect of transients, the rectangular window will outperform the Hann window. Indeed, with a periodic excitation no window should be used since this will introduce additional leakage errors. The local modeling approach clearly outperforms the spectral analysis approach, since it explicitly estimates and removes the transient component $T(\Omega_k)$ that is causing the FRF estimate using the spectral analysis method to be erroneous.

3.5. Closed-loop aspects

The techniques presented in the previous sections are described for an open-loop output error setup, see, e.g., Figure 3.1. Many precision motion systems have safety constraints, requiring closed-loop operations. In this section, the transition to a closed-loop identification setting is made as shown in Figure 3.4. It is shown that the techniques presented in Section 3.3 can be straightforwardly extended to a closed-loop setting when taking into account some important differences.

3.5.1. Indirect approach to Closed-loop identification

A common approach for the control of motion systems is to neglect possible cross-coupling between the DOFs or performing a decoupling procedure. This allows the simplification to a Single-Input Single-Output (SISO) control setting. Consider again an LTI discrete time system, now operating in closed-loop as shown in Figure 3.4. A transfer function estimation can be performed using excitation input $d(nT_s)$, identification input $u(nT_s)$ and identification output $y(nT_s)$, as described in Section 3.3.2, yielding (Söderström and Stoica, 1989, Chap. 10)

$$\hat{G}(k) = \frac{\hat{\Phi}_{yu}(k)}{\hat{\Phi}_{uu}(k)} = \frac{G_0 \Phi_{dd} - K \Phi_{vv}}{\Phi_{dd} + |K|^2 \Phi_{vv}}. \tag{3.24}$$

This clearly yields a biased estimate of G_0 since y and v are not independent in the closed-loop setting. This shows that taking a direct approach and identifying the system G_0 using y and u in a closed-loop setting can lead to an estimation bias.

Indirect approach To mitigate the estimation bias resulting from a direct approach in Eq. 3.24, an indirect approach is considered that identifies two transfer functions in a Single Input Multiple Output (SIMO) procedure to yield

$$\widehat{GS}(k) = \frac{\hat{\Phi}_{yd}}{\hat{\Phi}_{dd}}, \widehat{S}(k) = \frac{\hat{\Phi}_{ud}}{\hat{\Phi}_{dd}} \tag{3.25}$$

that are the estimate of the process sensitivity and sensitivity respectively. The system estimate $\hat{G}_0$ is then obtained by

$$\hat{G}(k) = \frac{\widehat{GS}(k)}{\widehat{S}(k)}. \tag{3.26}$$

Alternatively $\hat{G}(k)$ is obtained by $\hat{G}(k) = \frac{1}{K(k)}(\frac{1}{S(k)} - 1)$ but this requires the controller $K(k)$ to be known exactly, which is often not possible. The estimate (3.26) is unbiased in the closed-loop setting since d and v are independent. Note that (3.26) recovers (3.10) in the open-loop setting since then $S(k) = 1$ and $GS(k) = G(k)$. Similarly, the local approach proposed in Section 3.3.3 can be used to identify $GS(k)$ and $S(k)$ in (3.26) to yield an unbiased estimate of $\hat{G}(k)$ under transient conditions.

3.5.2. Closed-loop identification of multivariable systems

In this section the indirect method to closed-loop identification is extended to encompass MIMO systems. Depending on the control objective, a different plant
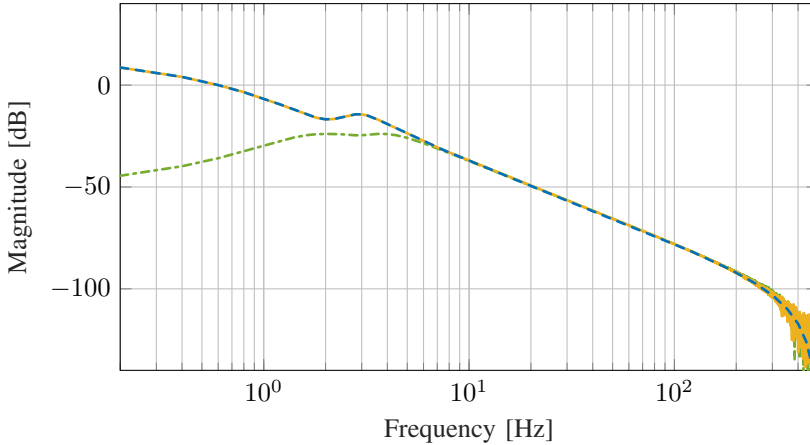
Figure 3.5. Comparison of the estimated FRF of the true system (- - -) using the direct method (- · -) and the indirect method (——) . It is shown that applying the direct method in a closed-loop setting yields a significantly biased result.

model is desired. A distinction is made between the true multivariable plant and an equivalent plant.

Consider a MIMO system in the closed-loop setting as shown in Figure 3.7. The system in Figure 3.7 is multivariable and the control solution is decentralized, i.e., diagonal. Consider now the proposed indirect method from Section 3.5.1 using excitation input d_1 and identification output u_1, y_1 and u_2, y_2 to identify the first column of $\hat{G}$ to obtain G_{11}, G_{21}. Applying the indirect method to individual entries of GS and S yields for G_{11}

$$\tilde{G}_{11}^{eq} = GS_{11}/S_{11} = G_{11} - \underbrace{\frac{G_{12}K_2G_{21}}{1 + K_2P_{22}}}_{\text{interaction}} . \tag{3.27}$$

Here, the estimated $\tilde{G}_{11}^{eq}$ is clearly different from the "true" MIMO entry G_{11}, as indicated in Figure 3.7. This is caused by the interaction terms G_{12}, G_{21} and the secondary closed-loop controller K_{22}. Indeed, the plant $\tilde{G}_{11}^{eq}$ is also known as the "equivalent plant", since it represents the fully coupled system as a single SISO transfer function. This approach is often applied in sequential loop closing, where a full MIMO system is modeled as a sequence of equivalent plants for which a SISO controller is designed (Maciejowski, 1989).

To obtain the full multivariable plant G a slightly different formulation to (3.27) is required. The plant G can straightforwardly be identified using 2 independent excitations, exciting d_1 and d_2 to identify the first and second column
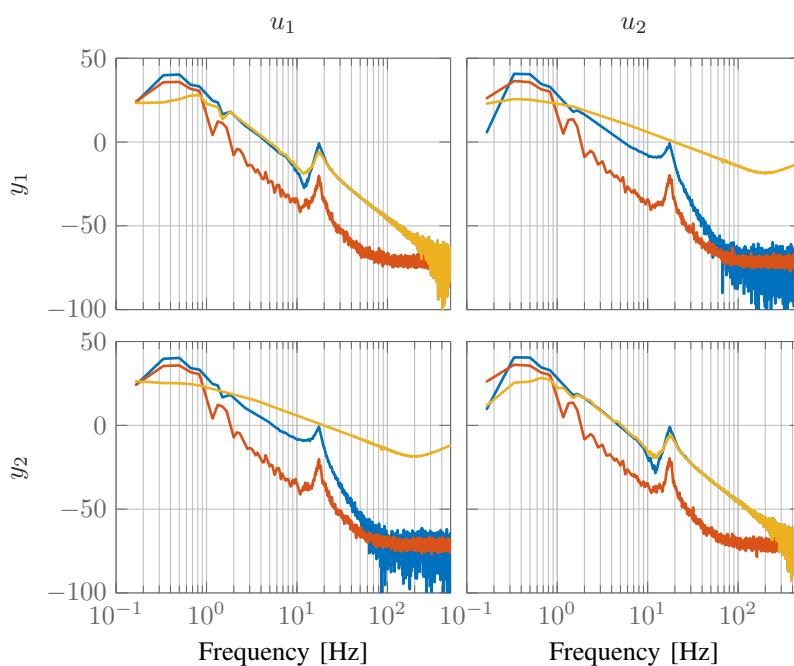
Figure 3.6. Experimental estimation of the MIMO transfer function matrix, shown as a magnitude [dB] plot, using both matrix wise (——), with corresponding variance (——), or element wise division (——), shown without variance, yielding significantly different models. Depending on the desired model, a specific operator should be used.
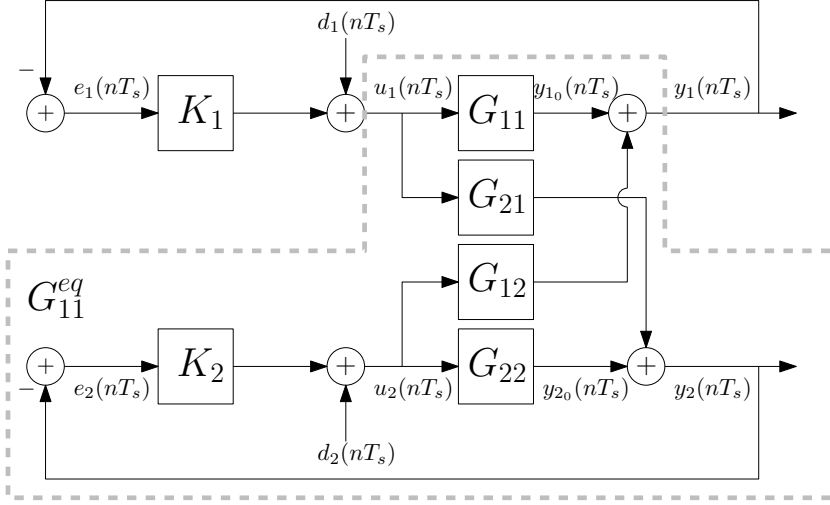
Figure 3.7. LTI discrete time system in a MIMO closed-loop setup. Here G_{11}^{eq} indicates the equivalent plant that includes the interaction in the secondary loop as a SISO transfer function.

respectively of GS and S. Then G is obtained by performing

$$G(\Omega_k) = GS(\Omega_k)S(\Omega_k)^{-1} \tag{3.28}$$

$$\begin{bmatrix} G_{11} & G_{12} \\ G_{21} & G_{22} \end{bmatrix} = \begin{bmatrix} GS_{11} & GS_{12} \\ GS_{21} & GS_{22} \end{bmatrix} \begin{bmatrix} S_{11} & S_{12} \\ S_{21} & S_{22} \end{bmatrix}^{-1} \tag{3.29}$$

for each frequency Ω_k. Here, the Frequency Response Matrix (FRM) of the closed-loop sensitivity function $S(\Omega_k)$ is inverted using a matrix inverse and not element wise inversion. While this difference is subtle, the obtained plant is significantly different for systems with interaction.

3.6. Experiments

In this section, the techniques presented in this chapter are applied to the experimental setup as shown in Figure 3.2. Specifically, the transient elimination by employing the local modeling technique, as shown in Section 3.3.3, and the closed-loop MIMO estimation, as shown in Section 3.5.2, are highlighted.

3.6.1. Transient elimination

To illustrate the effects of transient conditions on the estimation accuracy, an FRF is estimated on two different datasets. The first dataset contains 6 periods
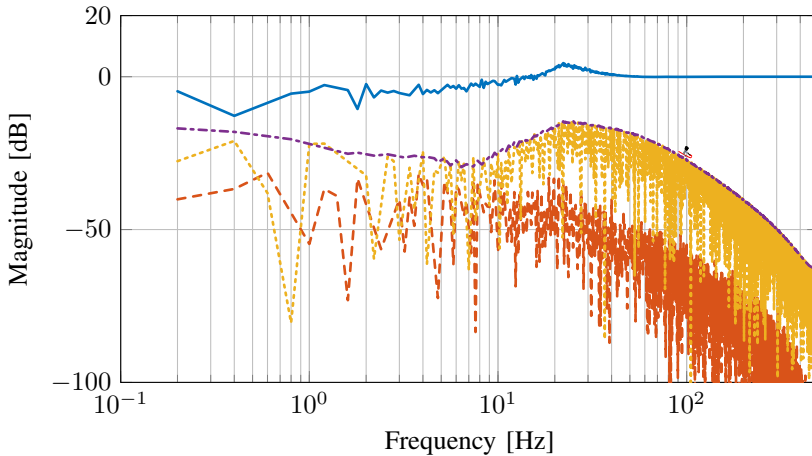
Figure 3.8. Estimating the FRF of the sensitivity function $S = \frac{u}{d}$ using 2 periods of a 5 [s] multisine, compared to using 6 periods as a baseline reference (——). Results show that the estimation error using spectral analysis (⋯) is significantly higher than when using the LPM method (---), this is caused by the transient contribution (-·-).

of the system response to a multisine signal with a length of 5 [s], yielding $N = 30 \cdot F_s = 30 \cdot 10^3$ samples, this dataset serves as a baseline reference. The second dataset contains only the first 2 periods of the first dataset, reducing the number of available samples to $N = 10 \cdot F_s = 10 \cdot 10^3$. Moreover, the initial periods contain significantly more transients than the latter. The results are shown in Figure 3.8. It is demonstrated that the LPM described in Section 3.3.3 is able to significantly reduce the estimation error caused by the transient contributions, when compared to the more classical spectral analysis approach. Furthermore, this allows for a significant reduction in experiment time since transient data can be used in the estimation. Traditionally, this transient data would need to be eliminated resulting in additional experiment time that can now be avoided.

3.6.2. MIMO identification in a closed-loop setting

In Section 3.5.2 it is shown that by applying the indirect method in multivariable setting, two different FRM can be obtained. By applying the matrix inverse, e.g., $\hat{G} = PSS^{-1}$ the multivariable plant model is obtained. Conversely, if an element wise inversion is employed, e.g., $PS \odot \dfrac{1}{S}$ where $\odot$ is the Hadamard product, then the equivalent plant model is obtained. This is illustrated on the experimental setup as shown in Figure 3.6. The results show that depending on the desired model, a different matrix operation should be employed.

3.7. Conclusion

In this chapter, an overview of important aspects in FRF identification for advanced motion control, specifically transient and closed-loop conditions, is presented. It is shown that if these aspects are not appropriately addressed the FRF estimate can be biased or of poor quality. By applying the techniques presented in this chapter a high quality unbiased FRF is obtained, facilitating parametric modeling or direct controller design for advanced motion control.

3

CHAPTER 4

Incorporating prior knowledge in local parametric modeling for frequency response measurements: Applied to thermal/mechanical systems [1]

Abstract: A key step in experimental modeling of many applications, including mechatronic systems, is Frequency Response Function (FRF) identification. Applying these techniques to systems where measurement time is limited leads to a situation where the accuracy of the identified model is deteriorated by transient dynamics. The aim of this chapter is to develop an identification procedure that mitigates these transient dynamics by employing local parametric modeling techniques. To improve the modeling accuracy, prior knowledge is suitably incorporated in the procedure, while at the same time allowing for rational parameterizations that ensure global optimality. This prior knowledge exploited in the relevant local frequency range using a specific Möbius transformation. It is shown that the presented framework leads to accurate identification results, both in a simulation study of a mechanical system, as well as on experimental data of a thermal system.

---

[1]The results in this chapter constitute Contribution C3 of this thesis. The chapter is based on "Evers, E., de Jager, B., and Oomen, T. Incorporating prior knowledge in local parametric modeling for frequency response measurements: Applied to thermal/mechanical systems. *Under review*".

4.1. Introduction

Frequency Response Function (FRF) identification is a key step in identification and control. Acquiring FRFs is often fast, inexpensive, and accurate, and requires very limited user-intervention. The obtained FRFs are used for many purposes, ranging from controller design by manual tuning (Oomen, 2018), optimal synthesis (Karimi and Zhu, 2014), stability analysis, interaction analysis (Evers et al., 2017), to parametric identification (Pintelon and Schoukens, 2012). Also, these FRFs are used in many application domains, e.g., in mechanical systems with flexible dynamics (Geerardyn et al., 2015; Voorhoeve et al., 2015), in thermal systems (Monteyne et al., 2013), in electrical systems (Relan et al., 2017a), and in combustion systems (Van Keulen et al., 2017).

Identification of FRFs has recently been substantially advanced by explicitly mitigating transient errors. Indeed, one of the tacit assumptions is that the system under test is in steady state, which is often not valid for experimental systems. Moreover, due to the slow dynamics in certain applications, e.g., thermal-mechanical systems, transients are increasingly relevant. In the Local Polynomial Method (LPM) (Pintelon et al., 2010), the smoothness, in the frequency domain, of the transient response is exploited by locally approximating the transfer function by a polynomial function to estimate and remove the transient component. In McKelvey and Guérin (2012), this is generalized towards the Local Rational Method (LRM), which uses a rational function in the local approximation.

Although the general parameterization used in the LRM enables improved identification results, the LRM involves an optimization problem that introduces additional challenges. As a key advantage, the LRM is a more general parameterization, directly recovering the LPM as a special case, and the additional freedom in the parameterization allows to capture dynamics, especially lightly damped, more accurately, see Verbeke and Schoukens (2018) for a theoretical analysis of the local approximation error and Geerardyn et al. (2015) for experimental evidence. On the other hand, the rational parametrization leads to a non-convex optimization problem, which is approximated in typical LRM approaches as in Levy (1959). Further improvements to employ an iterative algorithm has mixed outcomes, see, e.g., Geerardyn et al. (2015). Furthermore, as a direct consequence, the variance results, which are valid for LPM, are only accurate for the LRM for sufficiently high Signal to Noise Ratio (SNR) due to a bias effect.

The aim of this chapter is to present a unified framework for FRF identification that employs a rational local parameterization, in conjunction with a closed-form optimizer to yield reliable variance expressions and improved estimation accuracy. This is achieved by exploiting prior knowledge on the system, characterized by pole locations in the complex plane, e.g., resonance frequency region in mechanical systems (Geerardyn et al., 2015), or pole locations on the

real axis (Guo, 2014; Relan et al., 2017b) for thermal systems. In Peumans et al. (2018) prior knowledge is incorporated in the local rational parameterization by using Vector Fitting to estimate pole locations from input/output data.

In Peumans et al. (2018), Vector Fitting (VF) is used to provide the local rational parameterization with estimated pole locations. The VF algorithm is adapted to work on transient input-output data and employs an iterative process to estimate the pole locations.

The approach in the present chapter exploits the freedom of selecting those poles at a prescribed location. The presented approach is linear in the parameters, similar to the LPM, and therefore maintains the associated benefits, e.g., an analytical solution and bias and variance expression. The approach utilizes orthonormal rational basis functions (OBFs), which are well studied (Heuberger et al., 2005; Ninness and Gustafsson, 1997; De Vries et al., 1998) to form the basis for the local regression problem. Moreover, it is shown that it requires the development of OBFs with complex coefficients over the real line, which is in sharp contrast to the typical use of OBFs in system identification, where the support is typically over the imaginary axis or the unit disc. Indeed, local parametric methods (LPM/LRM) often tacitly represent FRFs of systems by complex valued transfer functions that are evaluated over the real axis.

The main contributions of this chapter are the following.

C1 A local parametric method is developed that uses a linearly parametrized basis, leading to an efficient optimization and closed-form solution, providing an accurate variance analysis yielding a reliable quality metric, and exploiting prior knowledge.

C2 Development of the necessary theory of OBFs using single complex pole parameterizations over the real line and transformation of prior knowledge to this domain.

C3 Validation of the method by application on relevant systems, e.g., on resonant dynamics in a simulation study of a mechanical system and first-order dynamics in an experimental study on a high tech industrial thermal setup.

The chapter is organized as follows. In Section 4.2, FRF identification under transient conditions is investigated. In Section 4.3, the local parametric method using the general parameterization considered is presented. In Section 4.4, a design for the local approximation basis is introduced together with a framework for orthonormal rational functions on the real line. A Möbius transformation is used to connect different components of the framework to appropriate prior knowledge and previous results. In Section 4.5 the method is applied in a case study on relevant industrial applications, involving 1) a simulation study involving lightly damped resonant dynamics and 2) experiments on a high tech industrial thermal setup. In Section 4.7, conclusions are presented.
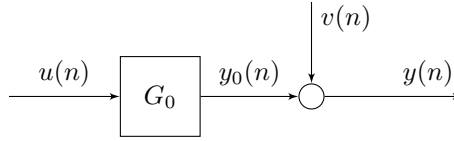
Figure 4.1. Discrete time linear time invariant system in an open-loop setting with input $u(n)$, measurement noise $v(n)$, and output $y(n)$.

4.2. Problem formulation

4.2.1. Transients in FRF identification

In this section, the role of transients in FRF identification is investigated.

Consider a discrete time Linear Time Invariant (LTI) Single-Input Single-Output (SISO) system G in an open-loop setting, as shown in Figure 4.1, and an excitation input $u(n)$. Then, the output $y(n)$, for an infinite time interval $n \in (-\infty, \infty)$, is given by

$$y(n) = \sum_{k=-\infty}^{\infty} u(k)g(n-k) + v(n) \tag{4.1}$$

where $g(n)$ is the impulse response of G and $v(n)$ the noise contribution on the output. By applying the Discrete Fourier Transform (DFT)

$$X(k) = \frac{1}{\sqrt{N}} \sum_{n=0}^{N-1} x(n) e^{\frac{-i2\pi kn}{N}} \tag{4.2}$$

on a finite interval, i.e., $n \in \{0, 1, \ldots, N-1\}$ of (4.1), yields

$$Y(k) = G(\Omega_k)U(k) + T(\Omega_k) + V(k) \tag{4.3}$$

in the frequency domain, where $G(\Omega_k)$ is the frequency response function of the dynamic system. Also, $Y(k), U(k), V(k)$ are the DFT of $y(n), u(n), v(n)$, respectively. Here, Ω_k denotes a generalized frequency unit, e.g. in continuous time $\Omega_k = j\omega$ and in discrete time $\Omega_k = e^{j\omega_k T_s}$ where T_s is the sample time, and k denotes the k-th frequency bin, the latter is used throughout.

In (4.3), $T(\Omega_k)$ accounts for the transients for both the system response $T_G(\Omega_k)$ and the noise $T_V(\Omega_k)$. The transient terms are directly related to the initial and final conditions of the system, i.e., the transition of an infinite to a finite interval such that the relation (4.3) is an exact representation. Also, the estimation error by neglecting the term $T(\Omega_k)$ is often referred to as leakage error (Pintelon and Schoukens, 2012). An insightful interpretation, see also McKelvey

and Guérin (2012), of $T(\Omega_k)$ can be made by using a state-space realization of the system G in Figure 4.1, e.g.,

$$x(n+1) = Ax(n) + Bu(n)$$
$$y(n) = Cx(n) + Du(n) \tag{4.4}$$

where $x(n) \in \mathbb{R}^{n_x}$ is the state vector with n_x the number of states. By then applying the DFT to (4.4), this directly connects to (4.3) through

$$G(\Omega_k) = C(e^{j\omega_k}I - A)^{-1}B + D \tag{4.5}$$
$$T(\Omega_k) = C(e^{j\omega_k}I - A)^{-1}(x(0) - x(N))e^{j\omega_k}. \tag{4.6}$$

Here, the term $G(\Omega_k)$ is the FRF of the LTI system and $T(\Omega_k)$ the transient contribution in the frequency domain. This shows that $T(\Omega_k)$ and $G(\Omega_k)$ exhibit similar but not identical dynamics, since they share the same poles and it is assumed that no pole/zero cancellations are present. However, the zeros of their transfer functions can be different.

4.2.2. Classical approach

The finite time response in (4.3) contains the additional terms $T(\Omega_k)$ and $V(k)$. A classical approach to identify the system $G(\Omega_k)$ is to use the Emperical Transfer Function Estimate (ETFE), i.e.,

$$\hat{G}(k) = Y(k)U^{-1}(k). \tag{4.7}$$

Analysis reveals that

$$G(\Omega_k) - \hat{G}(k) = \underbrace{T(\Omega_k)(k)U^{-1}(k) + V(k)U^{-1}(k)}_{\text{estimation error}}. \tag{4.8}$$

Hence, the transients, in addition to the noise contribution $V(k)$, lead to an estimation error.

4.2.3. Transients in different applications

The result (4.8) reveals that transients lead to estimation errors of the true system $G(\Omega_k)$. From (4.5)-(4.6), the system dynamics, i.e., pole locations, largely determine the transient contribution.

The central idea in this chapter is that the application domain provides clear prior knowledge on the locations of these poles. In Figure 4.2 pole locations are shown for a mechanical system, in Figure 4.2a, and a thermal system, in Figure 4.2b. An ad-hoc solution that is often employed to cope with transient data, is to remove the initial transient response from the identification data. Electro-mechanical systems, e.g., servo-positioning systems, often have lightly
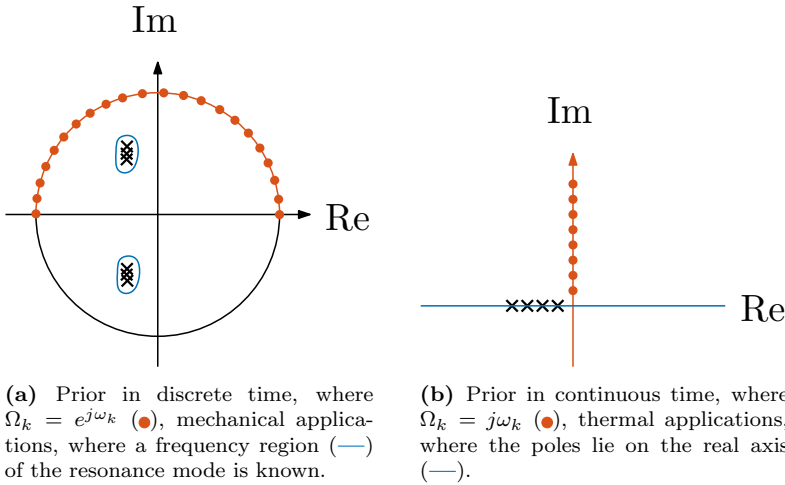
(a) Prior in discrete time, where $\Omega_k = e^{j\omega_k}$ (●), mechanical applications, where a frequency region (—) of the resonance mode is known.

(b) Prior in continuous time, where $\Omega_k = j\omega_k$ (●), thermal applications, where the poles lie on the real axis (—).

Figure 4.2. Examples of prior knowledge in different domains and applications. In the discrete time domain, where $\Omega_k = e^{j\omega_k}$, and mechanical applications, in Figure 4.2a, often a frequency region of resonance modes is known either from FEM analysis or initial experiments. In the continuous time domain, where $\Omega_k = j\omega_k$, and thermal applications, typically poles lie on the real negative axis.

damped dynamics and small time constants. For these systems, the transient contribution in (4.3) can sometimes be substantial due to low damping. For other systems, e.g., thermomechanical systems (Evers et al., 2018a), the time constants are significantly larger and the transient contributions constitute a dominant part of the output response. Waiting for the initial transient to settle requires an unacceptable increase in experiment time. FRF identification for a more general class of systems, e.g., including thermomechanical systems, requires a method capable of coping with data obtained under transient conditions.

In this chapter, an approach that explicitly takes into account the transient term $T(\Omega_k)$ to obtain an unbiased estimate of $\hat{G}(\Omega_k)$ is presented. This eliminates the need to discard the initial transient data, thus achieving a significant savings in the necessary experiment time to accurately identify the system.

4.2.4. Problem formulation

The problem considered in this chapter is as follows. Given an input/output sequence u, y where y contains a transient response, provide an accurate non-parametric FRF estimate $\hat{G}(\omega)$ of the true system $G_0(\omega)$ accompanied with a reliable variance estimation $\hat{C}_v(\omega)$.

To address this, a new parameterization is employed that allows for the estimation of transient responses by solving an optimization problem that has a closed-form solution, thereby providing an accurate estimate and accompanying variance expressions. Moreover, this method facilitates the incorporation of appropriate prior knowledge, enabling increased estimation accuracy.

4.3. Local parametric Modeling

In this section, a local parametric approach is presented with a rational parameterization that allows convex optimization, in particular a closed-form solution, leading to contribution $C1$. The outline of the section is as follows. First, the concept of local parametric modeling is presented. Second, the linear parameterization used in this chapter is presented. Third, the presented approach is connected to previous results on local parametric modeling, including the local polynomial method (LPM) (Pintelon and Schoukens, 2012) and the local rational method (LRM) (McKelvey and Guérin, 2012). In fact, these results are recovered as special cases.

4.3.1. Local modeling

Local parametric methods construct approximations of $G(e^{i\omega_k})$ and $T(e^{i\omega_k})$ in (4.3) on a subset of points

$$\lambda = \{k - l, \ldots, k + l\} \subset \mathbb{N}, \tag{4.9}$$

i.e., a local window of width $2l + 1$ with $l \in \mathbb{N}$, in the complex plane. This is illustrated in Figure 4.3 where a first-order and second-order local approximation is shown.

> **Remark**
>
> Throughout, the notation $\{k - l, \ldots, k + l\}$ is dropped, and k indicates a single DFT-bin and λ indicates the local window, i.e., $\lambda = \{k - l, \ldots, k + l\} \subset \mathbb{R}$.

The key mechanism underlying local parametric methods is the smoothness of both $G(\Omega_k)$ and $T(\Omega_k)$ in (4.3).

In particular, the input $U(k)$ is selected such that it is sufficiently exciting and "wild", i.e., having a non-sparse and non-smooth frequency spectrum in magnitude and/or phase. Signals that are particularly suited are (filtered) white noise or random phase multisines. This ensures that $G(\Omega_k)$ can be distinguished from $T(\Omega_k)$, since the latter is not affected by the system input $U(k)$. For each frequency point k, a local parametric approximation is constructed over neighboring points w, e.g., by polynomial functions in the LPM and rational

functions in the LRM. Then, an estimate for the transient component at $T(\Omega_k)$ is constructed using this local approximation, such that it can subsequently be removed from $G(\Omega_k)$. This is illustrated in Figure 4.3 for $G(k)$. The result for the transient $T(k)$ follows along conceptually similar lines. For more details on the local parametric method in general, see Evers et al. (2018a); Schoukens et al. (2012). In the remainder of this chapter, the emphasis lies on constructing a suitable local parametric approximation basis for the functions $G(\Omega_k), T(\Omega_k)$.

4.3.2. Linearly Parameterized Rational Parametrization

Consider again (4.3) and let

$$G(\Omega_\lambda) = \sum_{b=0}^{N_b} \theta_G^k(b)\Psi(b,\lambda) \tag{4.10}$$

$$T(\Omega_\lambda) = \sum_{b=0}^{N_b} \theta_T^k(b)\Psi(b,\lambda), \tag{4.11}$$

such that locally the terms in (4.3) are approximated in a window λ by an expansion of degree N_b using general basis functions $\Psi(b,\lambda) \in \mathbb{C}$ where $\theta_G^k(b) \in \mathbb{C}$ and $\theta_T^k(b) \in \mathbb{C}$ are the local coefficients for $G(\Omega_\lambda)$ and $T(\Omega_\lambda)$, respectively. Note that $\Psi = \lambda^b$ in (4.10) for the well-known Local Polynomial Method. For each point k this local approximation yields

$$\hat{Y}(\lambda) = \underbrace{\begin{bmatrix} \theta_G(k) & \theta_T(k) \end{bmatrix}}_{\Theta(k)} \underbrace{\begin{bmatrix} \Psi(\lambda) \otimes U(\lambda) \\ \Psi(\lambda) \end{bmatrix}}_{K(U(\lambda),\Psi(\lambda))} \tag{4.12}$$

where $\Theta(k)$ contains the local approximation coefficients for the basis functions contained in the regression matrix $K(\lambda) = K(U(\lambda), \Psi(\lambda))$. From this local approximation, only the center value, i.e., $G(\Omega_k)$ is used, as illustrated in Figure 4.3. This local approximation is repeated to obtain an estimate of $G(\Omega_k)$ and $T(\Omega_k)$ for each frequency bin k.

> **Remark**
>
> The input $U(\lambda)$ is assumed to vary sufficiently over the full input spectrum such that $G(\Omega_\lambda)U(\lambda)$ can be distinguished from $T(\Omega_\lambda)$ so $K(\lambda)$ does not lose rank, i.e., the input is sufficiently "wild". This can be achieved by, e.g., broadband noise excitation or random-phase multisines (Pintelon and Schoukens, 2012).
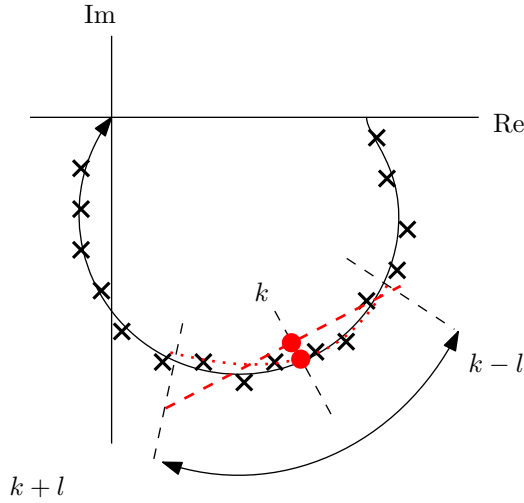
Figure 4.3. Resulting local approximation of $G(\Omega_k)$ in local parametric modelling in the complex plane. Here, a first order (- -) and second order (· · ·) approximation of the true plant (—) is constructed using the measured data (×) in the local window λ yielding an estimate for $G(\Omega_k)$ at k (●). The local approximation for $T(\Omega_k)$ follows along conceptually similar lines.

The coefficients $\Theta(k)$ are found by solving the Least Squares (LS) problem

$$\hat{\Theta}(k) := \arg\min_{\Theta} \sum_{p=k-l}^{k+l} |Y(p) - \Theta(k)K(p)|^2, \qquad (4.13)$$

which should be overdetermined. Then, $\hat{\Theta}$ is given by

$$\hat{\Theta}(k) = Y(\lambda)K(\lambda)^H (K(\lambda)K(\lambda)^H)^{-1}, \qquad (4.14)$$

where $K(\lambda)^H$ is the Hermitian transpose of the regression matrix $K(\lambda)$ in (4.12). Due to the closed-form solution, which resembles the LPM (Pintelon and Schoukens, 2012, Sec. 7.2.2), an estimate for the noise covariance matrix is given by

$$\hat{C}_v(k) = \frac{1}{q}(Y(\lambda) - \hat{Y}(\lambda))(Y(\lambda) - \hat{Y}(\lambda))^H \qquad (4.15)$$

where q is the degree of freedom of the residual $Y(\lambda) - \hat{Y}(\lambda)$, i.e., $q = 2l + 1 - N_b$. The final covariance on the estimated FRF $\mathrm{Cov}(\mathrm{vec}(\hat{G}(k)))$ is then determined by an appropriate transformation, e.g., Pintelon and Schoukens (2012, Chapter 7).

Indeed, the covariance of the estimated FRF is given by

$$\mathrm{cov}(\mathrm{vec}(\hat{G}(k))) = \overline{S^H S} \otimes \hat{C}_v(k), \qquad (4.16)$$

where

$$S = K(\lambda)^H (K(\lambda)K(\lambda)^H)^{-1} \begin{bmatrix} I_{n_u} \\ 0 \end{bmatrix} \Psi(k), \tag{4.17}$$

and vec() denotes a stacking of the columns of the matrix and n_u is the number of inputs of the estimated system.

> **Remark**
>
> The key point is that (4.15) holds for a linearly parameterized model (4.10), which is in sharp contrast to the LRM, see Section 4.3.3, in which case variance estimations are typically biased. This is caused by the Levy approximation that introduced measurement data in the regressor matrix. The result (4.15)-(4.16) holds for any linearly parametrized basis, the results in (Pintelon and Schoukens, 2012) are recovered as a special case.

The basis Ψ is general and allows for user-chosen parameterizations. For instance, the basis Ψ can be chosen to be a polynomial, rational, or fractional function of the window parameter w. In forthcoming sections, it is shown how earlier approaches fit in the framework. Then, a new approach is presented that enables the incorporation of prior knowledge.

4.3.3. Connection to LRM

A particular choice regarding the parametrization in (4.10) is to select rational polynomials for Ψ, which directly connects to previously used rational functions in the Local Rational Method (LRM) (McKelvey and Guérin, 2012). To introduce the LRM, consider the optimization problem

$$\hat{\Theta}_{LRM} := \underset{\Theta_{LRM}}{\arg\min} \sum_{p=k-n}^{k+n} \left| Y(p) - \frac{N_\lambda}{D_\lambda} U(p) - \frac{M_\lambda}{D_\lambda} \right|^2 \tag{4.18}$$

where

$$N_\lambda = \sum_{s=0}^{N_n} n_s(k)\lambda^s \tag{4.19}$$

$$M_\lambda = \sum_{s=0}^{N_m} m_s(k)\lambda^s \tag{4.20}$$

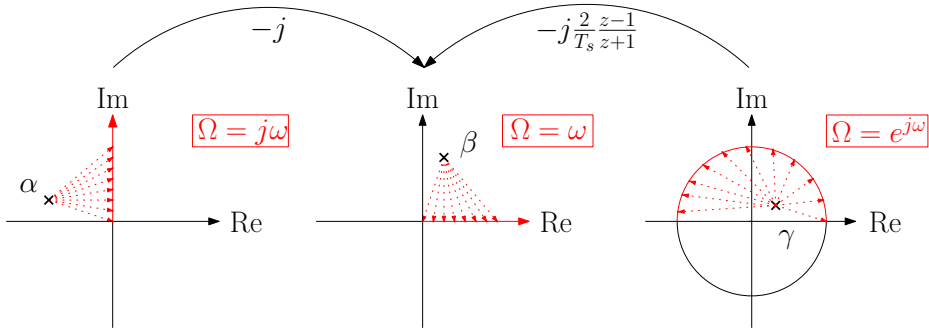$$D_\lambda = 1 + \sum_{s=1}^{N_d} d_s(k)\lambda^s. \tag{4.21}$$

Figure 4.4. Complex plane, with a pole location β as a function of $\Omega = \omega$, a pole location α as a function of $\Omega = j\omega$ or a pole location γ as a function of $\Omega = e^{j\omega}$. By applying the required Möbius transformations pole locations in different domains can be incorporated in the proposed parameterization.

In case of the typical LRM parameterization, the free parameters are $\Theta_{LRM} = [n_0, \ldots, n_{N_m}, m_0, \ldots, m_{N_m}, d_1, \ldots, d_{N_d}] \in \mathbb{C}^{N_n + N_m + N_d}$ where N_n, N_m, N_d denote the order of the plant and transient numerator and common denominator respectively. From (4.18), the LPM is directly recovered by setting $[d_{N_d} \ \ldots \ d_1] = 0$. For general D_w, (4.18) is non-linear in the parameters and generally no closed-form solution similar to (4.14) exists. At least two approaches (Geerardyn, 2016; McKelvey and Guérin, 2012; Verbeke and Schoukens, 2018; Voorhoeve et al., 2018) have been pursued to determine (4.18) and find Θ_{LRM}: 1) iteratively solving the LS problem, which has been applied in Geerardyn (2016) with mixed results or 2) multiplying the criterion with D_w as in the classical approach in Levy (1959), which introduces an a priori unknown weighting function in (4.18). On top of these aspects, both approaches lead to a situation where K contains measurement data that is corrupted with noise, potentially introducing errors in the variance estimate (4.15),(4.16), see also remark 4.3.2. The form in (4.12) combines a general rational basis with the benefits associated with a linear parametrization where the regression matrix is noise free.

4.4. LRMP

The local parametric approach in Section 4.3 yields improved FRF estimation by explicitly taking transient contributions into account. For this, a local parametric parameterization is used to approximate $T(\Omega_k)$ as a linear combination of basis functions Ψ. In this section, an approach facilitating the construction of a suitable basis Ψ is presented, henceforth referred to as the Local Rational Method with Prescribed poles (LRMP).

4.4.1. Approximation basis

In this section, the parameterization (4.10) is considered where the key idea is to select a basis Ψ such that the closed-form expression to (4.13) is retained. Consider a basis Ψ composed of rational functions with single complex poles, i.e.,

$$\Psi(\omega) = \sum_{b=0}^{N_b} \frac{1}{\omega + \beta_b} \tag{4.22}$$

where $\beta_b \in \mathbb{C}, b \in 1, \ldots, n_b$ are the prescribed poles of the rational functions and $\omega \in \mathbb{R}$ is the (local) frequency parameter on the real-line. This basis facilitates the modeling of resonant behavior and offers a general parameterization while (4.10) remains linear in the parameters. For the local approximation (4.10), the basis functions coefficients may be complex, indeed such model structures with complex parameters are standard in the local methods. In previous methods, e.g., in the LPM, the poles of the basis functions are all placed at ∞. In this chapter, the freedom in the location of the prescribed poles in (4.22) is exploited to obtain a higher approximation accuracy by including prior knowledge. In Section 4.5.1, the appropriate transformation, to the $\omega \in \mathbb{R}$ domain, of this prior knowledge is investigated further.

Assuming the poles β_b have been selected, see also Section 4.5, the basis can be systematically constructed using orthogonal rational functions on the real line.

Theorem 4.1. *Given $\beta_b \in \mathbb{C}$ where $b \in [0, N_b]$, i.e., the poles in (4.22). Let $\Psi(\omega)$ be parameterized as*

$$\Psi_b(\omega) = \begin{cases} \sqrt{-2\text{Im}(\beta_0)}\frac{-j}{\omega+\beta_0} & b = 0 \\ \sqrt{-2\text{Im}(\beta_b)}\frac{-j}{\omega+\beta_b}\prod_{l=0}^{b-1}\frac{\omega+\bar{\beta}_l}{\omega+\beta_l} & b \neq 0 \end{cases}, \tag{4.23}$$

then

$$\frac{1}{2\pi}\int_{-\infty}^{+\infty}\Psi_n(\omega)\overline{\Psi_m}(\omega)d\omega = \begin{cases} 1, & n = m \\ 0, & n \neq m \end{cases}, \tag{4.24}$$

where $\omega \in \mathbb{R}$, i.e., the basis Ψ is orthonormal on the real line.

A proof of Theorem 4.1 is provided in appendix 4.A. The basis in Theorem 4.1 is novel since the orthonormal basis functions are considered on the real line.

The orthogonality of the functions Ψ facilitates the repetition of poles to expand the basis, improving the approximation of the true FRF (Ninness et al., 2000). In fact, for a function $f(\omega)$ in the Hardy space H_2 for arbitrary $\epsilon > 0$ and for sufficiently large m an element $g(\omega) \in \{\Psi_b(\omega)\}_{k=1}^m$ can be found such that $||f - g||_2 \leq \epsilon$, i.e., the basis $\Psi(\omega)$ is complete in H_2. The basis Ψ is complete if the following theorem holds.

Theorem 4.2. *The model set spanned by the basis functions $\{\Psi_b(\omega)\}_{n\geq 0}$ is complete in all of the spaces $H_p, 1 < p < \infty$ if and only if*

$$\sum_{k=1}^{\infty} \frac{-\mathrm{Im}\{\beta_b\}}{1 + |\beta_b|^2} = \infty \tag{4.25}$$

A proof for this is presented in appendix 4.A.

The condition (4.25) in Theorem 4.2 is mild and fulfilled by (4.23) if the poles β_b are not on the real line. Finally, the orthogonality of the basis potentially yields improved numerical conditioning for the approximation problem (Akçay and Ninness, 1999).

> **Remark**
>
> The basis in Theorem 4.1 is orthogonal when evaluated over the real line as in (4.24). In the local window λ, this orthogonality can be lost since a discrete set of points is considered that no longer span the complete real line. A solution for this could be found in line with Van Herpen, R. (2014) that considers a discrete data-dependent basis to improve conditioning. The conditioning (Ninness et al., 1999) of (4.23) improves with the window size for $\lim_{\lambda \to N}$ where N is the total amount of samples in a measurement.

4

4.5. Employing prior knowledge: Möbius transformation

In this section, it is shown how to incorporate prior knowledge from different domains using a specific Möbius transformation, constituting contribution C2. Moreover, this transformation is used to connect the presented framework to previous results from literature.

A Möbius transformation is a conformal mapping defined on the extended complex plane $\mathbb{C}_\infty = \mathbb{C} \cup \{\infty\}$ of the form

$$f(z) = \frac{az + b}{cz + d} \tag{4.26}$$

where $z \in \mathbb{C}_\infty$ and $a, b, c, d \in \mathbb{C}$ satisfy $ad - bc \neq 0$. A well-known special case of this transformation is the bilinear transform, i.e., Tustin's method (Houpis and Lamont, 1992).

> **Remark**
>
> In previous local parametric modeling methods, discrete time frequency domain data, i.e., an FRF evaluated on points on the unit disc $e^{j\omega}$, is approximated by local models that are a function of $k \in \mathbb{N}$ on the real line, i.e., the DFT bins as illustrated in Figure 4.3. The transformation from $s = j\omega$ or $z = e^{j\omega}$ to the ω domain is often implicit, but it is essential when including prior system knowledge, as is done in this chapter.

4.5.1. Prior knowledge

In Section 4.4, a suitable basis Ψ for the local approximation (4.10) is presented, i.e., (4.23) where β_i is selected a priori. However, prior knowledge, e.g., system poles, is often defined in terms of the Laplace variable s or the Z-transform variable z, where the frequency response is obtained by substituting $s = j\omega$ and $z = e^{j\omega}$, respectively. In contrast, the functions (4.22) for which the poles are defined as β are evaluated on the real line w. Consequently, prior knowledge regarding the poles of the physical system $G(\Omega_k)$ cannot directly be incorporated in the local function (4.22). The appropriate prescribed poles β for (4.23) are transformed using the forthcoming results from prior knowledge in the continuous domain α or discrete domain γ, by employing the Möbius transformations shown in Figure 4.4.

Continuous time α   Given some knowledge on the system poles in continuous time domain, i.e., $\Omega_k = s$, an equivalent prior is obtained for the ω domain by using $\beta = -j\alpha$, such that their frequency response function is equal, e.g., $\Psi(\beta)|_\omega \equiv G(\alpha)|_{j\omega}$.

Discrete time γ   In the discrete time domain $\Omega_k = z$, a similar approach is applied by mapping the pole locations using a bilinear transformation $\beta = -j\frac{2}{T_s}\frac{z-1}{z+1}\gamma$ that is known as a Cayley transformation. However, care has to be taken, since for $\Psi(\beta)|_\omega \equiv G(\gamma)|_{e^{j\bar{\omega}T}}$ it holds that $\omega \neq \bar{\omega}$, i.e., the frequency $\bar{\omega}$ is distorted with respect to the original frequency ω.

> **Remark**
>
> To compensate the frequency distortion when including discrete time domain prior knowledge, several approaches can be used. First, the warping can be ignored as is commonly done in LPM techniques for discrete time systems. This could be used if the prior knowledge is mainly located at lower frequencies, where $\omega \approx \bar{\omega}$. Second, pre-warping in the bilinear transformation can be employed for each local frequency window w such that locally the reconstruction is exact. Third, the frequency axis can be
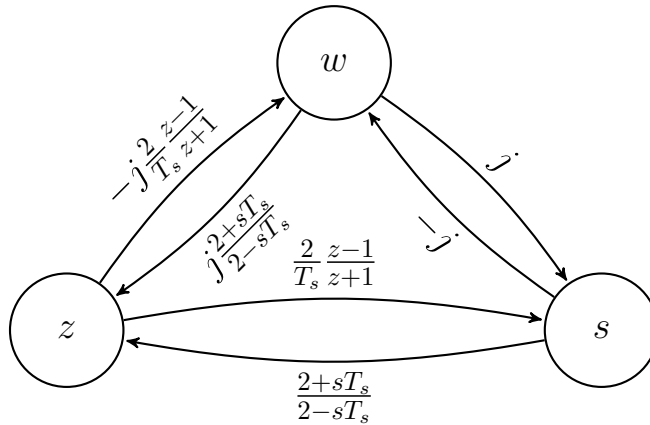
Figure 4.5. Diagram indicating the Möbius mapping to connect orthonormal functions in different domains.

adjusted by using $\omega = \frac{2}{T} \tan(\bar{\omega} \frac{T}{2})$ such that the reconstruction is exact over the full frequency range. Note that this results in non-equidistant frequency points in the ω domain (Houpis and Lamont, 1992).

Summarizing, by applying a suitable Möbius transformation any available prior knowledge can directly be incorporated into the basis Ψ in the ω domain.

4.5.2. Connection to existing results

In this section, the presented framework is connected to previous parameterizations in literature. Applying the Möbius transform $-j$ to the Local Rational Method with Prescribed poles (LRMP) in (4.23) results in the well-known continuous time Takenaka-Malmquist (Akçay and Ninness, 1999) basis. Moreover, if the Möbius transform $-j$ is combined with a bilinear transform, e.g., the Tustin approximation, the discrete time Takenaka-Malmquist (Takenaka, 1925) functions are obtained. The generalization in (4.23) simplifies to the well-known Laguerre functions by taking all $\beta_b \in \mathbb{C}, \operatorname{Re}(\beta) = 0$ such that the rational functions model a system containing first order real-valued poles. While selecting $\beta_{k+1} = -\bar{\beta}_k \in \mathbb{C}$ such that all complex poles appear in real positive/negative pairs, results in the Kautz basis functions. In Figure 4.5, the Möbius transformation is used to connect the presented basis to existing results found in literature (Akçay and Ninness, 1999; Ninness and Gustafsson, 1997; Takenaka, 1925).

4.6. Case study

In this section the theory from Section 4.4 with the design guidelines from Section 4.5 is applied in a case study. Both in a simulation study of a mechanical system and an experimental study of a thermal system.

> **Remark**
>
> Throughout this section it is assumed that accurate prior knowledge is available, e.g., through FEM modeling or initial experiments. In the case of uncertainty in the prior knowledge, mechanisms such as pole repetition or iterative pole placement can aid in improving the estimation accuracy. A sensitivity analysis towards uncertainty in the prescribed pole locations would provide additional value to the presented method. This sensitivity analysis is outside the scope of the current research.

4.6.1. Procedure

In the case study, the following procedure is employed to construct the FRF $\hat{G}$ and variance estimate $\hat{C}_v$.

Procedure 4.3 (FRF Identification). ***Require:*** *Appropriate excitation signal, e.g., white noise or random-phase multisine.*
  1: ***Perform simulation/experiment***
  2: **if** *Prior knowledge* **then** $\beta \leftarrow$ *according to Figure 4.4*
  3: **else** $\beta = 0$
  4: **end if**
  5: ***procedure*** LRMP$(U(k), Y(k), \beta)$
  6:      **for** $k \in [0, \ldots, N]$ **do**
  7:          *Construct* (4.13) *to obtain* $\hat{\Theta}(k)$
  8:          *Calculate* $\hat{G}(k)$ *and/or* $\hat{T}(k)$.
  9:          *Calculate the variance estimate* $\hat{C}_v$
 10:      **end for**
 11: **end procedure**

In this context, an appropriate excitation signal is system dependent, e.g., for a thermal system, an offset to the input is often required since a negative heat flux input is infeasible using conventional actuators.

4.6.2. Simulation study: Mechanical system

In this section, the method presented in Section 4.4 is applied to a mechanical system with resonant behavior in a simulation study. The true system is given
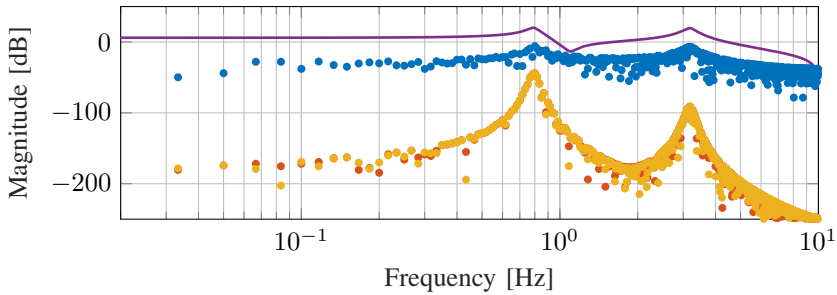
(a) Selecting $\beta = [0,0]$ recovers the LPM as a special case of the proposed approach.

(b) Including prior knowledge on the first resonance peak location by using $\beta = [0.76 + 0.6i, 0]$.
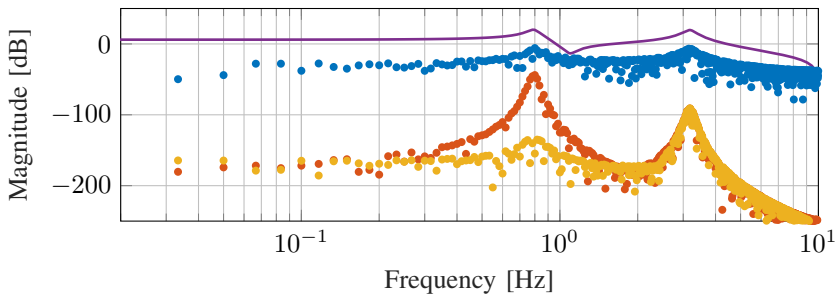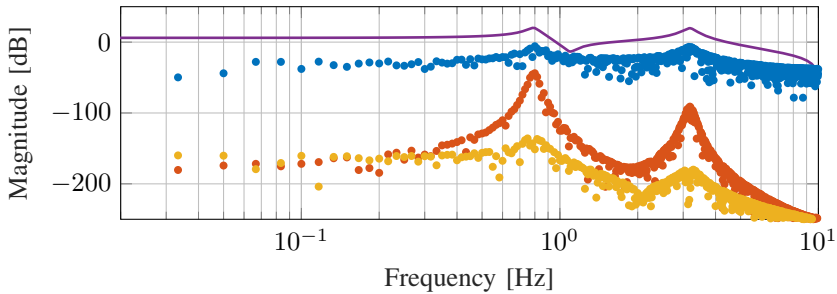

(c) Including both resonance peaks as prior knowledge by including two single complex poles at $\beta = [0.76 + 0.6i, 0.98 + 0.16i]$.

Figure 4.6. Reducing the estimation error by incorporating prior knowledge. True plant $G_0(\omega)$ (——) and estimation error $|G_0(\omega) - \hat{G}(\omega)|$ using classical approach (●), LPM (●) and LRMP (●). Here, the LPM is recovered as a special case of the LRMP by selecting $\beta = [0,0]$, as shown in Figure 4.6a. By incorporating additional prior knowledge, i.e., using the transformations in Figure 4.4 to incorporate the system poles γ as pre-scribed poles β, the estimation error is significantly reduced, as shown in Figure 4.6b and Figure 4.6c.

by

$$G_0(s) = \frac{\Omega_1^2}{s^2 + 2\zeta\Omega_1 + \Omega_1^2} + \frac{\Omega_2^2}{s^2 + 2\zeta\Omega_2 + \Omega_2^2} \tag{4.27}$$

characterized by the natural frequencies $\Omega_1 = 5$ [rad/s], $\Omega_2 = 4\Omega_1$ and damping coefficient $\zeta = 0.05$. The system $G_0(s)$ is then discretized using zero-order hold with a sample time $T_s = 1/20$ [s] to obtain $G_0(z)$. The dynamics of the true system is characterized by the system poles, that are $\gamma = [0.76\pm0.6i, 0.98\pm0.16i]$ in discrete time.

The system $G_0(z)$ is excited using 2 periods of a random-phase multisine of 60 [s] that is defined as

Definition 4.4.

$$u(n) = \sum_{k=1}^{N} A_k \sin(2\pi f_k n/N + \phi_k), \tag{4.28}$$

where, n is a specific discrete sample, N is the total number of samples, A_k is the amplitude of the sinusoidal signal at frequency f_k, ϕ_k is a uniformly distributed random-phase on $[0, 2\pi)$ such that $\mathbb{E}\{e^{i\phi_k}\} = 0$.

Then, an FRF estimate $\hat{G}_0(\omega)$ is obtained using the classical ETFE approach, the traditional LPM and the new LRMP approach. Initially, the prescribed poles β are set to 0, i.e., $\beta = [0, 0]$, by doing so the LPM is recovered as a special case of the LRMP. This results in an estimation error as shown in Figure 4.6a. Here, the LPM and LRMP both obtain a significantly better estimation of $G_0(z)$ when compared to the ETFE. Moreover, it is observed that the LPM and LRMP obtain similar results.

By then applying the LRMP with appropriate prior knowledge, e.g., by employing the transformations in Figure 4.4 on the poles α, γ, an improved estimation error is obtained. In Figure 4.6b, the prescribed poles include a single complex pole $\gamma(1)$ at the first resonance of $G_0(z)$. This results in an improved estimation error at the first resonance frequency. By expanding the basis Ψ to include a single complex pole at each resonance, the estimation error is decreased further as shown in Figure 4.6c.

4.6.3. Experimental study: Thermal system

In this section, an experimental case study on a precision motion system, considered in a thermal control context, is presented.

4.6.3.1   Thermal system: The experimental setup used in this chapter is shown in Figure 4.7a. A 2D-schematic overview of the setup including the relevant components and sensor location is shown in Figure 4.7b. In the original application, the system under test is a high precision linear motion stage moving in the y direction, used in optical inspection equipment. In this chapter, thermal
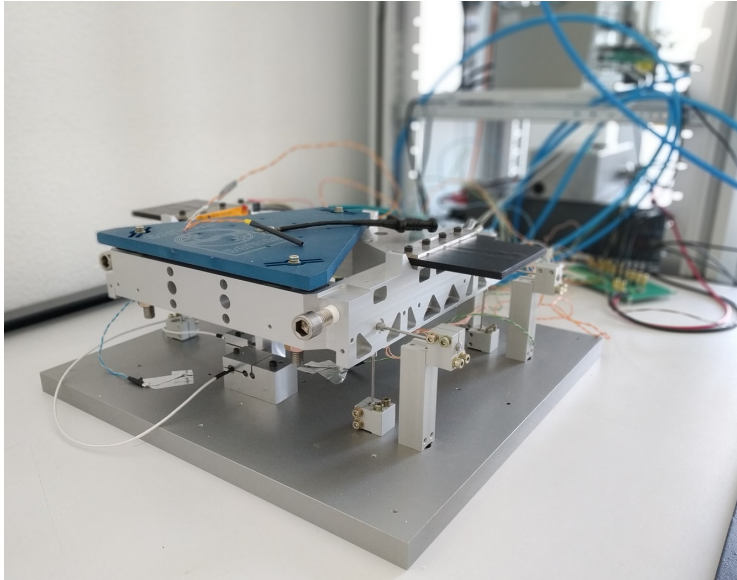
(a) Photograph of the experimental setup.
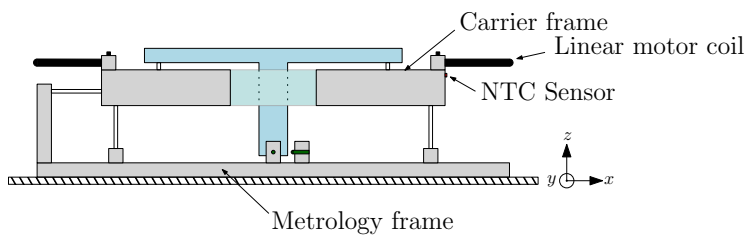
(b) Illustration of the experimental setup.

Figure 4.7. Photograph and illustration of the experimental setup, including the carrier frame and the base plate that is used as a metrology frame. On the illustration the carrier frame, metrology frame, linear motor coil, and sensor locations are indicated.

Figure 4.8. Temperature response of the experimental setup over a 48 hour period. The identification procedure is performed on two separate sub-records, set 1 and set 2, each containing 2 full periods of the multisine. Set 1 contains the initial response and a strong transient. Conversely, set 2 contains relatively little transient response and is used as a validation data set.

aspects of this setup are investigated. Transient effects in these types of systems are often dominant, hence the approach in Section 4.3 is expected to be highly applicable.

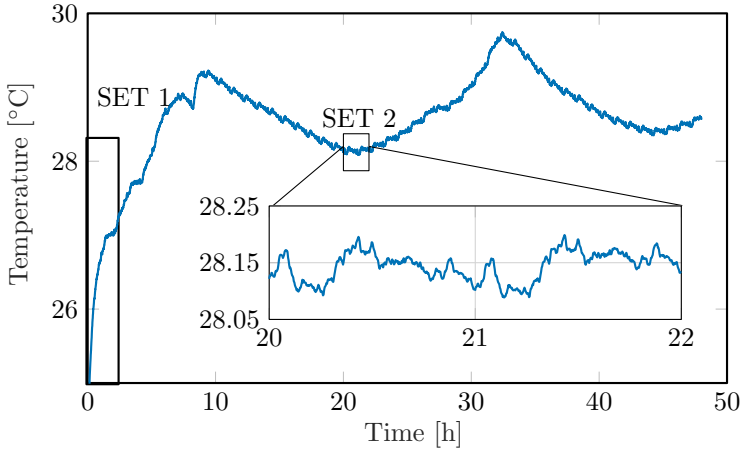To isolate the thermal aspects of the system the linear motor stator is removed, and its rotor, the coils, is maintained. The linear motors are then used as a thermal excitation source by passing a current through the coils, thereby heating them.

4.6.3.2   Transient response: To facilitate the presentation, a single temperature measurement is used as shown in Figure 4.7b, yielding a Single-Input Single-Output system. The system is excited using a random-phase multisine limited to 0.1 [Hz], with a peak of 5 [W] centered around an offset of 5 [W], since only heating is possible. Measurements are sampled at $F_s = 1$ [Hz], since the dynamics are predominantly low-frequent. The periodic excitation has a period length of $L = 1$ [h], that is repeated $P = 48$ times, yielding a total dataset of $F_s L P = 172800$ samples. The system response is presented in Figure 4.8, it shows the temperature over a 48 hour period.

The experimental data as shown in Figure 4.8 is separated into two sub-records, i.e., set 1 and set 2. Set 1 contains the first 2 periods, i.e., 2 hours, of the response data that includes the strong transient behavior due to the offset in the excitation signal. Set 2 contains the 2 periods as shown in the magnified plot in Figure 4.8, i.e., 2 hours starting at hour 20, that contains a minimal amount
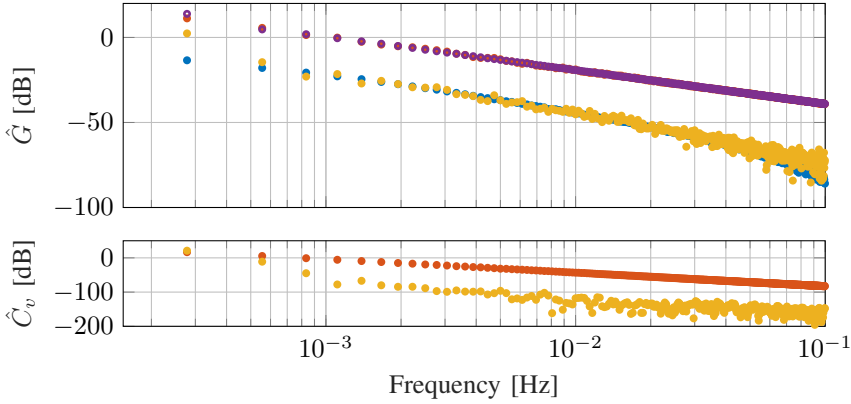
(a) Application of the ETFE (●) and LRMP (●) to sub-record 1. Interestingly, the ETFE is dominated by the transient contribution. Indeed, the transient T (○) obtained with the LRMP is almost equal to the ETFE. Here, G_0 (●) is shown for validation. Moreover, the variance $\hat{C}_v$ estimation of the ETFE appears to be biased by the transient.
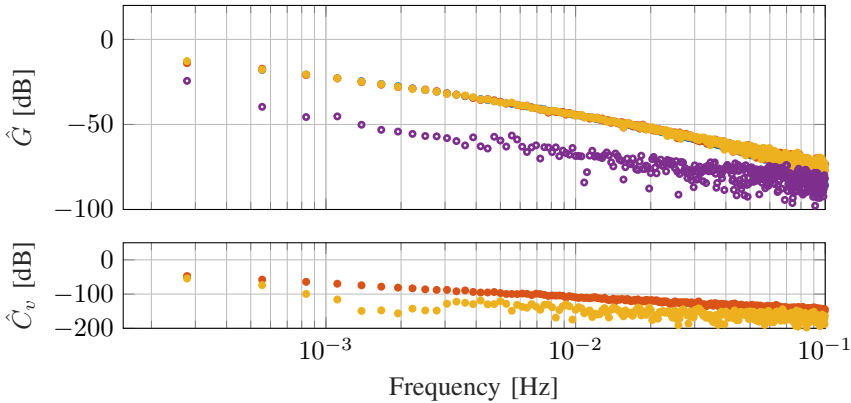
(b) To verify the accuracy of the presented LRMP approach, also sub-record 2 is investigated, which is almost transient free. In this case, the LRMP (●) and ETFE (●) obtain almost equal results and approach G_0 (●). The transient T (○) indeed is significantly smaller than in sub-record 1 allowing both the ETFE and LRMP to accurately estimate G_0. However, the variance estimation of the ETFE still appears to be influenced by the residual transient in the estimation, while the LRMP is not.

Figure 4.9. Application of both the traditional approach, the ETFE, and the presented approach, the LRMP, to both sub-record 1 and sub-record 2 in Figure 4.9a. Yielding a FRF $\hat{G}$, transfer function between heater input [W] to temperature output [°C], and corresponding variance $\hat{C}_v$.

of transient response and can be used as a validation data set. Furthermore, it is seen that the small and relatively fast dynamic response is superimposed onto a much larger and slower transient response caused by initial excitation and the $24-$hour, e.g., day/night, cycle of the environment. To validate the accuracy of the estimation, a validation FRF G_0 is obtained by averaging over 20 periods between hour 10 and 30.

By applying the classical approach, the ETFE, and the presented method, the LRMP, results as shown in Figure 4.9 are obtained. The results show the estimated plant $\hat{G}(\omega)$ for both methods and the estimated transient component $\hat{T}(\omega)$. Clearly, the first sub-record contains a strong transient response, therefore the ETFE yields a biased and therefore poor estimate of G_0. Moreover, the covariance estimate $\mathrm{cov}(\hat{G})$ using the ETFE appears to also be biased by the transient. The presented approach is able to estimate the FRF more accurately since it is close to G_0. The second sub-record contains significantly less transient contribution, allowing the ETFE to also accurately estimate the FRF. Although the variance $\mathrm{cov}(\hat{G})$ still appears slightly biased. However, relying on the second sub-record for FRF estimation requires a significant time investment since an additional 20 hours of experimental time is required to obtain the results.

By applying the approach presented in this chapter, a significant reduction in experimental time is achieved since the FRF can be estimated by measuring 2 hours, by using the first sub-record, opposed to 22 hours required for the classical approach.

4.7. Conclusion

Incorporation of prior knowledge in conjunction with explicit transient estimation leads to improved FRF estimation for a large class of systems, including thermal and mechanical systems. Indeed, the transient response often present in measurements from these systems can cause a biased FRF estimate when employing classical approaches. Recent advancements in FRF identification employ local modeling techniques to estimate and remove these transients from the response. The framework presented in this chapter enables fast and accurate frequency response function estimation of a wide class of systems with a reliable quality metric, i.e., covariance expressions. This is achieved by utilizing a unified approach to local parametric modeling. It presents a local rational parameterization while maintaining a closed form solution by using prescribed poles. It leverages appropriate Möbius transformations to incorporate prior knowledge from different domains and applications in the local parameterization. The presented approach yields high-fidelity models that enable the application of advanced design, analysis and control procedures.

4.A. Proofs

Proof to theorem 4.1

Proof. Given the results in (Akçay and Ninness, 1999), where it is shown that the continuous time Takanaka-Malmquist functions, e.g.,

$$B_n(s) = \frac{\sqrt{2\mathrm{Re}\{\alpha_n\}}}{s + \alpha_n} \prod_{l=0}^{k-1} \frac{s - \bar{\alpha}_l}{s + \alpha_l} \qquad (4.29)$$

are orthonormal with respect to

$$\frac{1}{2\pi} \int_{-\infty}^{+\infty} B_n(j\omega)\overline{B_m}(j\omega)d\omega = \begin{cases} 1, & n = m \\ 0, & n \neq m, \end{cases} \qquad (4.30)$$

it suffices to show that $\Psi(\beta, \omega) \equiv B(\alpha, j\omega)$. Given $\alpha = x + jy$ then $\beta = -j\alpha = y - jx$, resulting in

$$\Psi(\beta, w) = \sqrt{2x}\frac{-j}{\omega + y - jx} \prod \frac{\omega + y + jx}{\omega + y - jx} \qquad (4.31)$$

$$= \sqrt{2x}\frac{1}{j\omega + x + jy} \prod \frac{j\omega - x + jy}{j\omega + x + jy} \qquad (4.32)$$

$$= \sqrt{2Re\{\alpha\}}\frac{1}{s + \alpha} \prod \frac{s - \bar{\alpha}}{s + \alpha} \qquad (4.33)$$

which concludes the proof. □

Proof to theorem 4.2

Proof. Given the results in (Akçay and Ninness, 1999), where it is shown that (4.29) is complete if and only if

$$\sum_{n=1}^{\infty} \frac{\mathrm{Re}\{\alpha_n\}}{1 + |\alpha_n|^2}. \qquad (4.34)$$

It is shown that $\Psi(\beta, \omega) \equiv B(\alpha, j\omega)$. Therefore, is sufficient to show that (4.25) is equivalent to (4.34), where $\beta = -j\alpha$. Since $|\alpha| \equiv |\beta|$ and $\mathrm{Re}\{\alpha\} = \mathrm{Re}\{j\beta\} = -\mathrm{Im}\{\beta\}$ this equivalence is straightforward which concludes the proof. □

Thermoelectric Modules in Mechatronic Systems: From Modeling to Control [1]

Abstract: Active thermal control enables substantial improvements in accuracy and throughput in industrial applications, e.g., in the medical industry, high-power lighting industry, and semiconductor industry. Thermoelectric Modules provide major advantages compared to traditional electric heater based control. The aim of this chapter is to provide a complete framework for modeling and control of thermoelectric modules. Temperature-dependencies are explicitly taken into account to yield a high-fidelity model over a wide operating temperature range. This model is then leveraged in a feedback linearization control strategy. Both the modeling and control approach are validated on an experimental setup. The techniques presented in this chapter form a complete framework from modeling to control of thermoelectric modules.

---

[1] The results in this chapter constitute Contribution C4 of this thesis. The chapter is based on "Evers, E., Slenders, R., van Gils, R., and Oomen, T. Temperature-Dependent Modeling of Thermoelectric Elements. *In preparation for journal submission*", related preliminary results are reported in "Evers, E., Slenders, R., van Gils, R., and Oomen, T. Temperature-Dependent Modeling of Thermoelectric Elements. 21th World Congress of the International Federation of Automatic Control (IFAC 2020 World Congress) - Berlin, Germany. 2020.".

5.1. Introduction

Advanced thermal control is crucial to achieve the required specifications on accuracy and throughput in many industries, especially in the medical, high-power lighting, and semiconductor industry. For example, in the medical field, diagnostic platforms are used to process extremely small fluid volumes, e.g., blood or saliva samples (Yager et al., 2006). Hand-held devices are designed to significantly reduce analysis time and reagent costs. The temperature of the fluid volumes needs to be accurately controlled during a wide range temperature cycle. In particular, in PCR amplification, which is presently used to test for active infections in patients during the COVID-19 pandemic (Zhu et al., 2020), it is critical to quickly cycle the sample over wide temperature range. Another example is in high-power LED lighting, where LEDs offer superior efficiency compared to traditional lighting. However, due to their limited volume the heat that is produced is of significant intensity and must be actively controlled to achieve sufficient light quality and an increased lifespan (Kaya, 2014). Finally, in the semiconductor industry, wafer scanners are used to produce integrated circuits that need to achieve a positioning accuracy of nanometers, where the current performance of these high precision systems is often limited by thermally induced deformations. Therefore, thermal control is an important aspect in their mechatronic design (Bos et al., 2018). In Box (2008); Saathof et al. (2016), the benefits of active thermal control are already confirmed for this class of systems.

TEMs are not limited to heating, offering major advantages over resistive heaters that are often used in thermal control. TEMs are compact, have no moving parts and facilitate both heating and cooling. This lends them particularly well to application in compact systems, e.g., small scale PCR amplification devices (Qiu and Yuan, 2005). In mechatronic systems they can be employed to locally provide both heating and cooling, unlike traditional water conditioning circuits.

The thermodynamics of a TEM are non-affine, containing both state dependencies and input non-linearities, complicating the controller design. Standard linear control methods (e.g. PID control) could be unreliable because stability, robustness, and performance cannot be guaranteed. Therefore, nonlinear control methods can be considered. In recent literature several methods have been developed. In Shao et al. (2014), a linear-parameter-varying approach is used to control the nonlinear system, which linearizes the nonlinear system at different operating points. For each operating point a different controller is synthesized. In Guiatni et al. (2007), a sliding- mode controller is used, which applies a state feedback. The state feedback ensures that all trajectories move towards a stable sliding manifold. Lastly, in Bos et al. (2018), the nonlinear system is partially linearized using a feedback linearization by creating a new input that has linear input-to-output (IO) dynamics. This facilitates the use of conventional linear control approaches. However, this approach do not include temperature depen-

dency in the model and linearization controller. This limits their applicability to situations were the temperature remains fairly constant, limiting their use in industrial applications were a large temperature range is desired.

In Van Gils, Rob (2017), again a linearization approach is used to control the cold side of a TEM for a large temperature range from 5 to 80 °C. However, it is shown that the feedback linearization yields some residual nonlinear dynamics, that might cause instabilities. Moreover, in both Bos et al. (2018) and Van Gils, Rob (2017) an observer design is recommended since it is often impractical or infeasible to install temperature sensors around the point of interest (POI). For example, in a diagnostic platform the fluid temperature must be accurately controlled but placing a temperature sensor in the fluid is undesired due to hygiene constraints. In Bos et al. (2020), initial results using an Extended Kalman Filter (EKF) are promising, although a stability guarantee remains challenging. Consequently, in this chapter a state reconstruction is obtained by utilizing sensors placed at different locations in the system and an appropriate observer design.

This chapter provides a complete framework for modeling and control of thermoelectric elements. A dedicated experimental identification setup is used to obtain a high-fidelity temperature dependent model, presented in earlier work in Evers et al. (2020). By leveraging the temperature-dependent parameters in the model, the system is linearized using feedback linearization that is valid over a wide temperature range. And to facilitate situations where sensor placement is limited, an observer based approach is presented that is capable of providing an accurate state reconstruction using a limited number of temperature sensors. The main result of this chapter is a unified modeling and control approach for thermoelectric elements, with the following detailed contributions.

C1 A temperature-dependent model of a TEM.

C2 Providing a systematic parameter estimation procedure over a wide temperature range.

C3 Accurate feedback linearization with a stability guarantee using temperature-dependent parameters.

C4 Observer design incorporating temperature-dependent parameters with a Lyapunov-based stability proof.

C5 Experimental validation of total framework from modeling to control.

5.2. Problem formulation

In this section, a motivation and problem formulation for modeling and control of thermoelectric elements is presented. Subsequently, the experimental setup that will serve as an illustrative benchmark setup throughout this chapter is presented.

5.2.1. Problem formulation

In view of control and to facilitate the implementation of both accurate linearization methods and observer design, a high-fidelity model of the TEM is required. In literature, often a limited operating temperature for the TEM is considered, allowing the model to be simplified by using temperature independent parameters. In this chapter, in particular to facilitate the application of peltiers in the medical industry (Jiang et al., 2012; Qiu and Yuan, 2005), a significantly larger operating temperature range is considered, e.g., from 5 to 80 °C, necessitating the inclusion of temperature dependency (Cui et al., 2019; Pourkiaei et al., 2019) in the simulation model.

Moreover, it is important to take the increased temperature range into account during the control design. Previous results have shown that a feedback linearization approach is promising but can lead to inaccurate results when neglecting temperature dependencies. Concurrently, it is important to provide a suitable stability proof for the entire operating range. Finally, to facilitate situations were sensor placement is limited, a suitable observer based approach must be constructed. Summarizing these aspects leads to the following problem formulation.

Problem formulation

Provide a framework for temperature dependent modeling and control of thermoelectric elements that facilitates their application in a wide range of operating conditions.

5.2.2. Experimental setup

In this section, the illustrative experimental setup that is used throughout this chapter is presented. The methods and techniques presented in each section are validated using this experimental setup.

Application setup   The setup, shown in Figure 5.1, consists of two thermoelectric elements clamped between a steel bottom plate and an aluminum top plate. Both elements are cooled by convective cooling using an aluminum heat sink attached to the top plate. The experimental setup incorporates 2 TEMs to provide additional challenges by introducing interaction. More precisely it uses TEM 2 en 3 from Section 5.4 since they are the most similar. The setup is constructed such that it presents a sufficiently challenging benchmark for modeling and control and will be referred to as the application setup throughout.

Data acquisition   To measure the temperature, voltages and current in the TEM setup a CompactDAQ by National Instruments is used. To facilitate temperature measures using the thermistors with Negative Temperature Coefficient
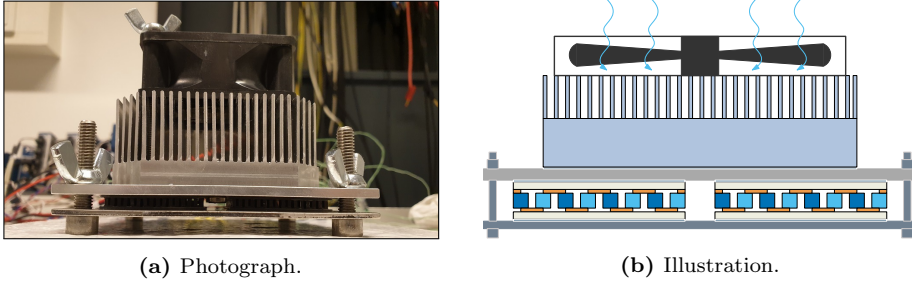
(a) Photograph.   (b) Illustration.

Figure 5.1. Photograph and illustration of the experimental validation setup. On the top, a photograph of the setup is shown. On the bottom, an illustrative representation is shown. To reduce the thermal resistance between components a thin layer of thermal conductive compound is applied on the contact surfaces. The heat transfer through the bolted connection is considered negligible

(NTC), a Wheatstone bridge is used that converts the resistance measurements, and thereby the temperature, to an electrical potential. Moreover, since the identification method proposed in Section 5.4.1 relies heavily on accurate knowledge of the input current, a precision power resistor is placed in series with the TEM. The resistor is selected such that its resistance R remains constant for the operating currents. By measuring the voltage drop V over the resistor the current can be accurately calculated, i.e., $I = \frac{V}{R}$.

5.3. Modeling

In this section the first principle relations describing the major thermoelectric effects within a thermoelectric module are presented. Following this, a full lumped-mass model of the experimental setup presented in Subsection 5.2.2 is provided that is used throughout as an illustrative example.

5.3.1. First principles

The thermoelectric module in this chapter is modeled through lumped-capacitance discretization, i.e., the module is subdivided into lumps of uniform temperature. This is illustrated in Figure 5.2, where the module is divided into a hot and cold side where each ceramic plate is a single lump. Conversely, some literature models a TEM on the pellet level (Qiu and Shi, 2020), which would be overly complicated for the application considered in this chapter. Moreover, it is shown that a lumped-mass discretization can yield sufficient model granularity. The thermoelectric dynamics of a TEM are described by including 3 phenomena: 1) the Fourier effect Q_f, 2) Joule heating Q_j and 3) the Peltier effect Q_p.

(a) Photograph.

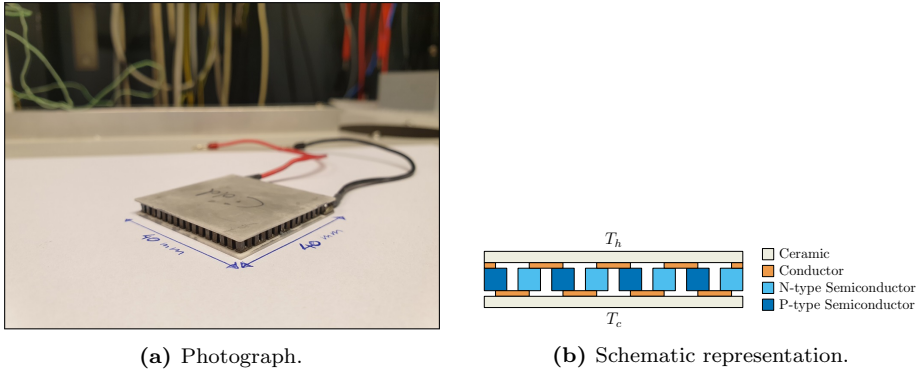

(b) Schematic representation.

Figure 5.2. Photograph and schematic representation of the thermoelectric module used in this chapter. The semiconductor elements are contained between two ceramic plates.

Fourier effect   The Fourier effect Q_f describes the energy transfer through conduction between the 2 sides of the TEM and it is given by

$$Q_f^{1\rightarrow2} = \frac{K_m \cdot A}{d}(T_1 - T_2) \tag{5.1}$$

for conduction from temperature T_1 to T_2 with K_m the conductivity of TEM in $W/m \cdot K$, A the area in m^2 perpendicular to the heat flow and d in m the distance of the heat flow path.

Joule heating   Joule heating Q_j occurs when an electrical current flows through a resistive element, in this case the TEM, and is given by

$$Q_j = R_m I^2 \tag{5.2}$$

where R_m is the electrical resistance in Ω of a single TEM and I is the current in A. It describes the energy loss of electrons moving through an electrical resistance, and it is typically unavoidable without employing superconductivity at cryogenic temperatures.

Peltier effect   The Peltier effect describes the occurrence of a heat flow over a semi-conductor in the presence of an electrical potential difference and resulting current. The analogous Seebeck effect describes the occurrence of an electrical potential over a semi-conductor in the presence of a temperature gradient. While they are manifestations of the same physical phenomenon, for the thermal dynamics the former is described as

$$Q_p = S_m T I \tag{5.3}$$

where S_m is the Seebeck coefficient of the TEM and T is the temperature at the cold/hot side.

It is assumed that the Joule heating Q_j, that is generated in the semi-conductors, see Figure 5.2b, is divided equally over the hot and cold side of the TEM since the module is symmetric. The heat balance equations for the hot and cold side are then given by

$$Q_c = Q_f^{h \to c} + \frac{1}{2}Q_j - Q_p + Q^{env \to c} \tag{5.4}$$

$$= K_m(T_h - T_c) + \frac{1}{2}R_m I^2 - S_m T_c I + Q^{env \to c}$$

$$Q_h = Q_f^{c \to h} + \frac{1}{2}Q_j + Q_p + Q^{env \to h} \tag{5.5}$$

$$= K_m(T_c - T_h) + \frac{1}{2}R_m I^2 + S_m T_h I + Q^{env \to h}$$

where $Q^{env \to c,h}$ accounts for any thermal interaction with the environment, indicated by the superscript ^{env}, i.e., the ambient air or neighboring lumps.

5.3.2. Modeling the experimental setup

To construct a finite order model that is tractable for parameter identification and control, the setup, as shown in Figure 5.1, is discretized into 18 lumps. Lumped mass modeling assumes the lump temperature to be uniform in each discrete lump, and a measure for the accuracy of this assumption is the Biot number

$$\text{Bi} = \frac{R_{in}}{R_{ext}} \tag{5.6}$$

that is a ratio of the internal and external resistance which should be smaller than Bi < 0.1 to achieve uniformity within the lump. Consequently, a discretization as shown in Figure 5.3 is obtained. To obtain lump temperature measurements, both thermocouples (TC) and negative temperature coefficient thermistors (NTC) temperature sensors are attached to the setup.

By constructing an energy balance equation for each lump, an accurate model is constructed including the TEMs and any connecting elements. This results in a state-space model, where the states $x = T_{(1,\ldots,n_x)}$, with n_x the number of states, represent the temperature of the lumps with corresponding state equations

$$E_n \dot{x}_n = \sum Q_n, \quad n \in \{1, \ldots n_x\} \tag{5.7}$$

where $E_n = m_n c_n$ is the thermal capacitance of the lump n with m_n the mass in kg and c_n the specific heat capacity in J/kgK and $\sum Q_n$ the heat balance
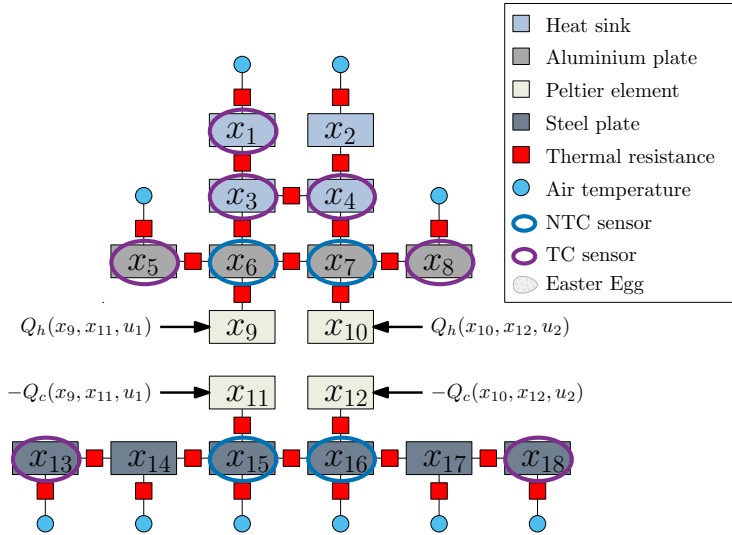
Figure 5.3. Illustration of the lumped-mass discretization of the experimental setup resulting in a network of connected nodes. The illustration also indicates the sensor placement, which is assumed to measure the true lump temperature.

equation, akin to (5.4), for a specific lump n. By collecting these differential equations the state-space model of a system is given by

$$E\dot{x} = Ax + Bw + F^{NL}(x, u) \tag{5.8}$$
$$y = Cx$$
$$x(0)_n = w \ \forall \ n \in \{1, 2, \ldots, n_x\}$$

where $E \in \mathbb{R}^{n_x \times n_x}$ is the thermal mass matrix, $B \in \mathbb{R}^{n_x \times 1}$ the disturbance input matrix with w the ambient air temperature, $F^{NL}(x, u)$ is a nonlinear function depending on x and the input current $u = I$, $C \in \mathbb{R}^{n_s \times n_x}$ is the output matrix with n_s the number of temperature sensors, $x(0)_n \in \mathbb{R}^{n_x \times 1}$ is the initial condition of the states. By incorporating the nonlinear input, e.g., the joule heating Q_j and state-dependent dynamics in $F^{NL}(x, u)$ a full system model is constructed. This nonlinear input function $F^{NL}(x, u)$ is given by

$$F^{NL}(x,u) = \begin{bmatrix} 0 \\ \vdots \\ 0 \\ K_m(x_c - x_h) + \frac{1}{2}R_m u^2 + S_m x_h u \\ K_m(x_h - x_c) + \frac{1}{2}R_m u^2 - S_m x_c u \\ 0 \\ \vdots \\ 0 \end{bmatrix}. \tag{5.9}$$

where $x_h \in \mathbb{R}^{n_h \times 1}$, $x_c \in \mathbb{R}^{n_c \times 1}$ with $n_h = n_c = n_{TEM}$ the number of lumps on the hot and cold side of the number of TEMs respectively, which for the illustrative setup is $n_{TEM} = 2$, and $K_m, R_m, S_m \in \mathbb{R}^{n_{TEM} \times 1}$ are respectively the thermal conductivity, electrical resistance and Seebeck coefficient of the corresponding TEM. Observe that the first term in (5.9) is actually a linear contribution, assuming that K_m is not state-dependent. Including this linear term in (5.9) allows the structuring of the linear dynamics matrix $A \in \mathbb{R}^{n_x \times n_x}$ as

$$A = \begin{bmatrix} A_H & \mathbf{0} \\ \mathbf{0} & A_C \end{bmatrix} \tag{5.10}$$

where $A_H \in \mathbb{R}^{n_H \times n_H}$ and $A_C \in \mathbb{R}^{n_C \times n_C}$ are considered the hot and cold sides dynamics respectively with n_H, n_C the number of lumps in their respective parts of the model. Consequently, the states are structured as $x = \begin{bmatrix} x_{L_h} & x_h & x_c & x_{L_c} \end{bmatrix} \in \mathbb{R}^{n_x}$ where $x_{L_h} \in \mathbb{R}^{n_H - n_h}, x_{L_c} \in \mathbb{R}^{n_C - n_c}$ are the states associated with the thermal node network on the hot side and cold side respectively, i.e., $x_{1,\ldots,8}$ for the hot side and $x_{13,\ldots,18}$ for the cold side. The disturbance input matrix $B \in \mathbb{R}^{n_x \times 1}$ is also structured as

$$B = \begin{bmatrix} B_H & 0 & 0 & B_C \end{bmatrix}^T \tag{5.11}$$

where $B_H \in \mathbb{R}^{n_H - n_h \times 1}$ and $B_c \in \mathbb{R}^{n_C - n_c \times 1}$ since it is assumed that the TEMs are not coupled directly to the ambient air w, see Figure 5.3. The output matrix C is structured as

$$C = \mathrm{diag}\left(C_1^{1 \times n_H - n_h}, 0^{1 \times n_h}, 0^{1 \times n_c}, C_1^{1 \times n_C - n_c}\right) \in \mathbb{R}^{n_x \times n_x} \tag{5.12}$$

where $C_1 = \begin{bmatrix} 1 & 0 & 1 & 1 & 1 & 1 & 1 & 1 \end{bmatrix}$ and $C_2 = \begin{bmatrix} 1 & 0 & 1 & 1 & 0 & 1 \end{bmatrix}$ such that the appropriate lumps are measured according to the sensor placement shown in Figure 5.3. Moreover, the lumps $x_{9,\ldots,12}$ consist of the TEM ceramic plates and their state, i.e., temperature, is not directly measurable.

Remark

Note that the derivation of (5.8) is done in continuous time, a discrete time model is obtained by applying an appropriate discretization method, e.g., Euler discretization. For completeness and to allow reproducibility of the results, a full numerical model of (5.8) is provided in Appendix.5.A.

5.4. Temperature dependent modeling

Employing constant parameters in the model (5.8) can yield sufficiently accurate results for systems that operate in a limited temperature range, as demonstrated in Bos et al. (2018). For the systems considered in this chapter, e.g., a blood diagnostic device that cycles over a large temperature range, this is often not sufficient and temperature dependencies must be taken into account. In this section, emphasis is placed on temperature dependent modeling, and it is shown that including this dependency can increase modeling accuracy for a wide temperature range.

Including the temperature dependency in (5.8) is done by modeling the parameters S_m and R_m as a function of the average temperature T_{avg} of the TEM, i.e., $S_m(T_{avg}), R_m(T_{avg})$, where

$$T_{avg} = \frac{T_c + T_h}{2}. \tag{5.13}$$

Remark

While the conductivity of the TEM is also considered temperature dependent in some literature (Ju et al., 2019) in this chapter this was not deemed beneficial within the current temperature range and it is taken as a constant value.

5.4.1. Identifying temperature dependent parameters

To include the temperature dependency of R_m and S_m requires an identification procedure that can determine the value of these parameters over the required temperature range. This is done by measuring the electrical potential V_{TEM} required to induce a fixed current I_{TEM} in a single TEM. The total voltage is given by

$$\begin{aligned} V_{TEM} &= V_{R_m} + V_{S_m} \\ &= R_m(T_{avg})I_{TEM} + S_m(T_{avg})(T_h - T_c) \end{aligned} \tag{5.14}$$

where I_{TEM} is the current output in A of an amplifier used to control the TEM. This amplifier is controlled in high-gain feedback, therefore it adjusts its output
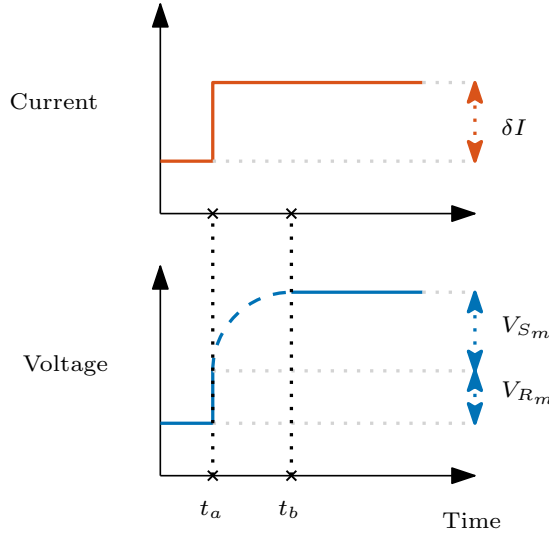
Figure 5.4. Illustration of the voltage profile following a current step δI (—). Since the current amplifier is in closed-loop, the voltage (—) is increased to compensate for the back EMF voltage V_{S_m}.

voltage to compensate for the V_{S_m} that acts as a back EMF type voltage. This voltage V_{S_m} in V is known as the Seebeck effect, and it generates a voltage based on the temperature gradient over the TEM.

Time constants   Solving (5.14) for 2 unknowns, i.e., $S_m(T_{avg}), R_m(T_{avg})$, is generally not possible. However, as suggested in Mitrani et al. (2004), V_{R_m} and V_{S_m} manifest in different time scales. This difference in time constants is illustrated in Figure 5.4. At time t_a, a current command δI is applied to the amplifier, causing an instantaneous step in electric potential V_{R_m}. While V_{S_m} only manifests after a sufficient time has passed and a thermal equilibrium is reached at time t_b yielding a $\Delta T = T_h - T_c$ over the TEM. By explicitly exploiting this difference in time constants, both $S_m(T_{avg})$ and $R_m(T_{avg})$ can be determined from (5.14) using voltage measurements.

5.4.2. Experimental identification setup

In this section the temperature dependent parameters are identified using the approach presented in Section 5.4.1. A dedicated TEM parameter identification setup is designed to isolate the TEM from external influences and facilitate accurate estimation of temperature dependent parameters. In Figure 5.5 a schematic representation of the setup is shown. The TEM is clamped between two stain-
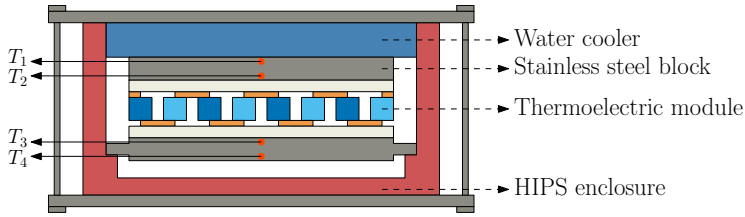
Figure 5.5. Schematic representation of the experimental setup, its various components and sensor locations.
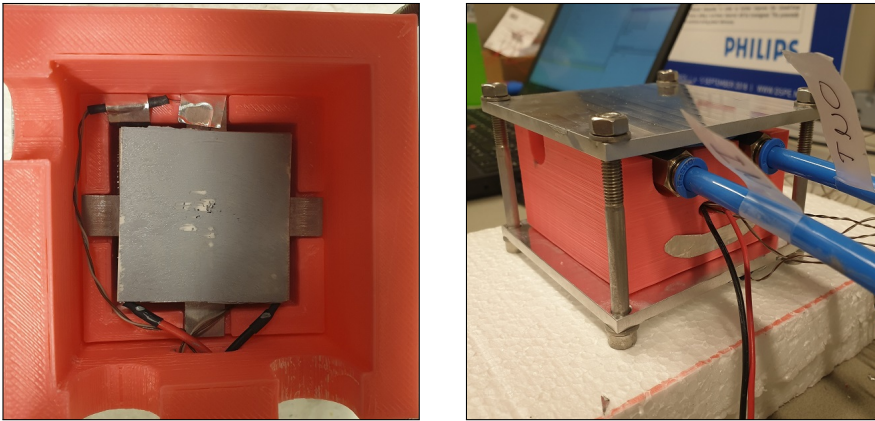
Figure 5.6. Photographs of the experimental identification setup. On the left the internal compartment is shown, illustrating a small thermal connection to the HIPS enclosure by reducing the contact area of the support. On the right, the full setup is shown including the connections to the water chiller that provides conditioned water to the heatsink.

less steel blocks to provide some additional thermal mass and spread the heat evenly. On the top, the hot side, the steel block is conditioned using a water cooling block and water chiller to provide a controllable temperature stable heat sink. The setup is encapsulated by a 3D-printed enclosure made of High Impact PolyStyrene (HIPS) that is printed with a low infill of 10% to provide thermal insulation from the environment. The temperature measurements are obtained by using NTCs. Each stainless steel block contains 2 sensors, as indicated in Figure 5.5, where T_2 and T_3 are considered the TEM hot and cold side respectively. To mitigate heat transfer from the setup to the enclosure, small tabs connect the lower block to the HIPS enclosure, as shown in Figure 5.6, to minimize the contact area.

5.4.3. Temperature dependent identification

In this section, the method proposed in Section 5.4.1 is utilized to estimate the temperature dependent parameters $R_m(T_{avg}), S_m(T_{avg})$ for multiple TEMs. To yield an accurate model for the purposes of this chapter, a significant temperature range for T_{avg} must be considered. To achieve this, the input current I is changed in small increments covering a wide operating range, as shown in Figure 5.7a.

Identification procedure   The identification procedure of the temperature dependent parameters is described in Algorithm 1

Algorithm 1 Identification procedure

    Initalize $I = I_0$
    for Each δI **do**
        I + δI
        Calculate $R_m(T_{avg}) = \delta I / V_{R_m}$
Ensure: Steady-State
        Calculate $S_m(T_{avg}) = V_{S_m} / \Delta T$
    end for

---

where δI are the steps in the current reference for the amplifiers, as shown in Figure 5.7a and $I_0 = 0$ is the initial current. The electrical resistance $R_m(T_{avg})$ is estimated from the instantaneous voltage jump V_{R_m}, shown in Figure 5.7b, that occurs after a step in current, since $R_m(T_{avg}) = I / V_{R_m}$. Then, the current is maintained until the system reaches a steady-state and associated ΔT, as shown in 5.7c. This yields a back EMF voltage due to the Seebeck effect $V_{S_m} = S_m(T_{avg}) \Delta T$, that is used to estimate $S_m(T_{avg})$. By repeating this process both parameters are estimated for a range of T_{avg}.

Temperature-dependent parameters   The identification procedure is repeated for 3 different, but of equal type, TEMs. This allows the characterization of an average parameter over a batch of actuators. While individual calibration curves could yield superior results, most applications do not allow for dedicated unit calibration tests, since they are both time intensive and expensive. The results of the identification procedure are shown in Figure 5.8 for $R_m(T_{avg})$ and in Figure 5.9 for $S_m(T_{avg})$. Both parameters show a linear dependency on T_{avg} and a significant change of their value over the range of 15 [°C] to 55 [°C], that corresponds to a cold-side temperature range of 5 [°C] to 85 [°C] since the hot-side is maintained at a constant temperature of 25 [°C]. The results show a small spread over the different TEMs. However, in Figure 5.9 the first module has a slightly different $S_m(T_{avg})$, this could be an outlier but a larger sample
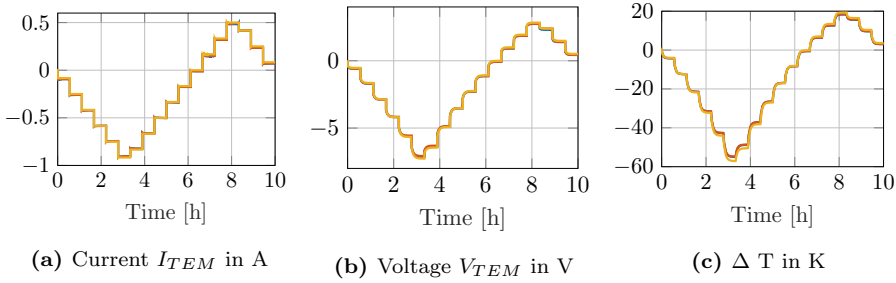
(a) Current I_{TEM} in A

(b) Voltage V_{TEM} in V

(c) Δ T in K

Figure 5.7. Identification experiment used to identify the temperature dependent electrical resistance $R_m(T)$ and Seebeck coefficient $S_m(T)$. The different sub-plots show the Current, Voltage and Temperature respectively. The experiment is repeated for 3 modules, TEM 1 (—), TEM 2 (—) and TEM 3 (—), and the results for all modules are quite similar.

size is required to yield a more definitive outcome. Moreover, since the input current profile consists of both positive and negative δI steps, at similar T_{avg}, some insight into possible hysteresis effects is gained. In the results, the positive and negative current perturbation yield similar parameter estimates, indicating that hysteresis effects are negligible.

5.4.4. Experimental validation

To verify the effectiveness of a model structured as in (5.8) with temperature dependent parameters $S_m(T_{avg}), R_m(T_{avg})$ a comparison of modeling with and without temperature dependencies is shown in Figure 5.10. The modeling error, without including temperature dependencies as shown in Figure 5.10a, is quite significant, especially when a large temperature range is considered. By including the temperature dependencies of the model parameters the modeling error, as shown in Figure 5.10b, is significantly reduced. More importantly, while there is still a residual error, it appears to be much less correlated with the temperature range. This indicates that the temperature dependency is successfully taken into account.

5.5. Feedback linearization

In this section a feedback linearization approach is presented that linearizes the input to output dynamics of a TEM setup. The model obtained in Section 5.3 is leveraged to improve accuracy of the linearization over a wide operating range.
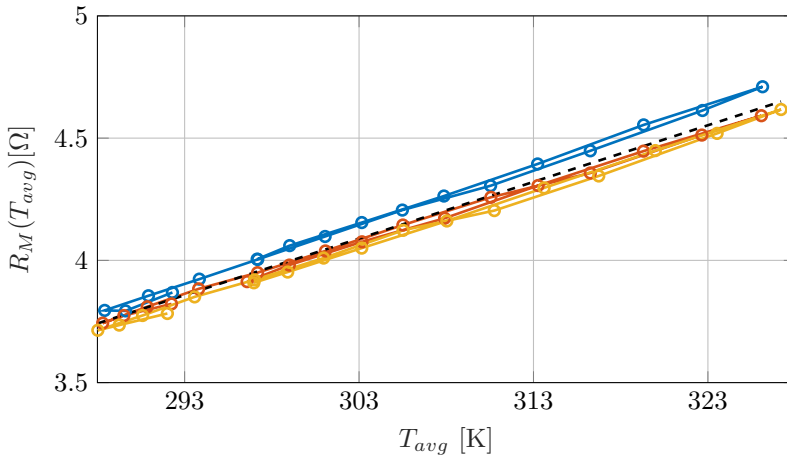
Figure 5.8. Identifying the temperature dependent electrical resistance $R_m(T)$ for different TEMs. It shows that for TEM 1 (—o—), TEM 2 (—o—) and TEM 3 (—o—) the results show a similar linear relation with the average temperature T_{avg} for all TEMs leading to an average $R_m(T_{avg})$ (- - -).
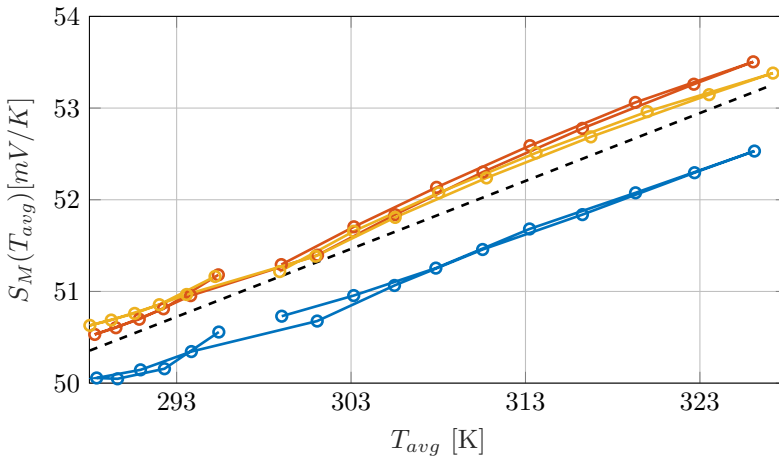
Figure 5.9. Identifying the temperature dependent Seebeck coefficient $S_m(T)$ for different TEMs. It shows that for TEM 2 (—o—) and TEM 3 (—o—) the result is quite similar, and TEM 1 (—o—) deviates from the rest. This yields a slightly shifted average linear relation for $S_m(T_{avg})$ (- - -).
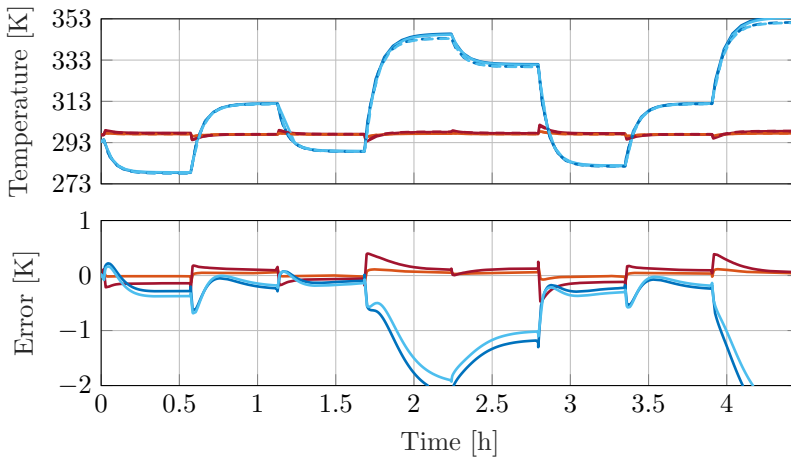
(a) Constant parameters S_m, R_m.
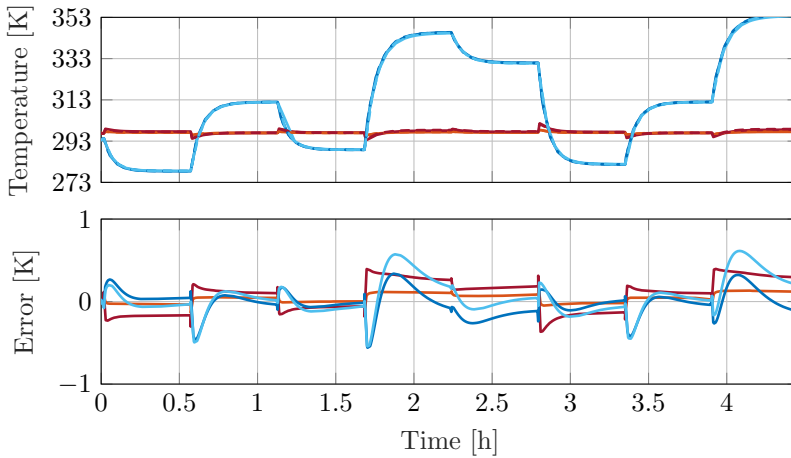
(b) Temperature-dependent parameters $S_m(T_{avg}), R_m(T_{avg})$.

Figure 5.10. Simulation results (dashed) compared to experimental measurements (solid) using temperature dependent parameters for T_1 (—), T_2 (—), T_3 (—), T_4 (—). The model prediction error is significantly improved to results in Figure 5.10a by taking into account temperature dependent parameters.

5.5.1. Feedback linearization
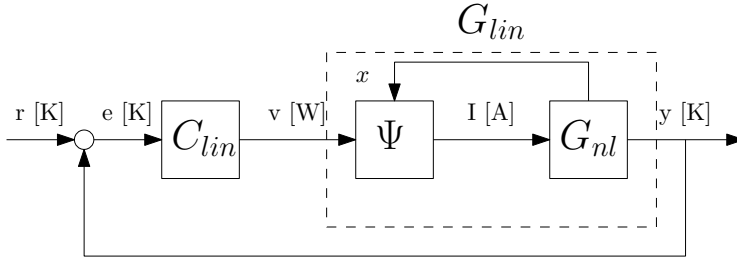
Figure 5.11. Closed-loop control diagram including the feedback linearization law Ψ that linearizes the non-linear system G_{nl} to obtain a system G_{lin} that is linear in input u to output $y = x_c$ dynamics.

Remark

To facilitate the presentation, in this section a single TEM is considered. For multiple TEMs, e.g., 2 modules as shown in Figure 5.3, the cold side state vector is $x_c \in \mathbb{R}^{n_{TEM}}$ with n_{TEM} the number of TEMs in the setup.

Given the system in (5.8) with the non-linear function F_{NL} in (5.9). Consider the feedback linearization law $I = \Psi(v, x)$, as shown in Figure 5.11, that provides I given a variable v and states x where

$$v = K_m(x_h - x_c) + \frac{1}{2}R_m I^2 - S_m x_c I \tag{5.15}$$

that can be solved for I to find

$$I = \Psi(v, x) = \frac{S_m x_c}{R_m} - \sqrt{\frac{(S_m x_c)^2}{R_M^2} + \frac{2(v - K_m(x_h - x_c))}{R_m}} \tag{5.16}$$

where $S_m(T_{avg})$ and $R_m(T_{avg})$ are both a function of the average temperature $T_{avg} = \dfrac{x_h - x_c}{2}$. Clearly, solving (5.15) for I has 2 possible solutions with (5.16) being the one that yields to smallest I for a given v. The feedback linearization law (5.15) is constructed for x_c and not x_h since the cold side of the TEM is most commonly the side of interest. A similar approach could be used to linearize towards x_h, although the stability proof will be slightly more involved. The variable v has a clear physical interpretation, it represents the effective heating power in the TEM. Moreover, a lower bound on v is required to ensure non-complex values in (5.16) given by

$$\Gamma : v \geq K_m(x_h - x_c) - \frac{S_m^2 x_c^2}{2R_m}. \tag{5.17}$$

Finally, an optimal current that maximizes the effective heating power is given by

$$I_{opt} = \frac{S_m x_c}{R_M} \tag{5.18}$$

that is obtained if the effective heating power (5.15) is minimized for I.

Applying the feedback linearization law $\Psi(v, x)$ to the system in (5.8), with the structure as proposed in (5.10), yields the following state equations

$$E \begin{bmatrix} \dot{x}_{L_h} \\ \dot{x}_h \\ \dot{x}_c \\ \dot{x}_{L_c} \end{bmatrix} = \begin{bmatrix} A_H & \mathbf{0} \\ \mathbf{0} & A_C \end{bmatrix} \begin{bmatrix} x_{L_h} \\ x_h \\ x_c \\ x_{L_c} \end{bmatrix} + \begin{bmatrix} B_H \\ 0 \\ 0 \\ B_C \end{bmatrix} w + \begin{bmatrix} \mathbf{0} \\ f_h^{NL} \\ v \\ \mathbf{0} \end{bmatrix} \tag{5.19}$$

Here, the "hot side" dynamics are non-linear since they are affected by $f_h^{NL}(x_h, x_c, u(v)) = \frac{1}{2}R_m u^2 + S_m x_h u + K_m(x_c - x_h)$, and the "cold side" dynamics are linear since they are solely affected by v. By including the conduction term $K_m(x_h - x_c)$ in $\Psi(v, x)$ a uni-directional coupling is achieved, i.e., the hot side does not influence the cold side. Consequently, classical linear control can be employed to generate an appropriate control input v for the linear plant G_{lin} where the dynamics from v to $y = x_c$ are now linearized. The controller C_{lin} is typically a collection of linear filters, e.g., a PID controller, that can be tuned through loopshaping techniques (Skogestad and Postlethwaite, 2009).

5.5.2. Stability

The feedback linearization law from Section 5.5.1 achieves unidirectional decoupling of the hot side to the cold side. Moreover, a controller for G_{lin} can be constructed such that it is stable. However, this does not guarantee that an unreachable set point does not induce unstable behavior, known as thermal runaway. This can occur when an infeasible amount of cooling for v is required to achieve a certain temperature setpoint that is not achievable by the TEM. To guarantee full system stability, input to state stability can be guaranteed by constructing a Lyapunov candidate function

$$V = x_H^T P_H x_H + x_C^T P_c x_C \tag{5.20}$$

$$= \begin{bmatrix} x_{L_h} \\ x_h \end{bmatrix}^T \underbrace{\begin{bmatrix} P_{L_h} & 0 \\ 0 & P_h \end{bmatrix}}_{P_H} \begin{bmatrix} x_{L_h} \\ x_h \end{bmatrix} + \begin{bmatrix} x_c \\ x_{L_c} \end{bmatrix}^T \underbrace{\begin{bmatrix} P_c & 0 \\ 0 & P_{L_c} \end{bmatrix}}_{P_C} \begin{bmatrix} x_c \\ x_{L_c} \end{bmatrix}$$

where $P_H = P_H^T \succ 0$ and $P_C = P_C^T \succ 0$ are symmetric and positive definite matrices. The derivative of V in (5.20) is given, after explicitly exploiting the

structure in (5.19), by

$$\dot{V} = \dot{x}_H^T P_H x_H + x_H^T P_H \dot{x}_H + \dot{x}_C^T P_C x_C + x_C^T P_C \dot{x}_C \tag{5.21}$$
$$= -x_H^T Q_H x_H - x_C^T Q_C x_C$$
$$+ 2x_{L_h}^T P_{L_h} B_H w + 2x_{L_c}^T P_{L_c} B_C w$$
$$+ 2x_h P_h f_h^{NL}(x_h, x_c, I(v)) + 2x_c P_c v$$

where

$$-Q_H = A_H^T P_H + P_H A_H \tag{5.22}$$
$$-Q_C = A_C^T P_C + P_C A_C \tag{5.23}$$

satisfy the continuous Lyapunov equation, i.e., $AP + PA^H + Q = 0$, with $Q_H = Q_H^T \succ 0$ and $Q_C = Q_C^T \succ 0$, assuming a solution exists that allows the structure for P_H, P_C as illustrated in (5.20). To guarantee the structure in (5.20) additional constraints are enforced during the solving of the LMIs in (5.22). Input to state stability can be concluded if $\dot{V} < 0$ in (5.21) and a solution to (5.22) exists under the structure imposed by (5.20). To conclude that $\dot{V} < 0$ holds, (5.21) is further simplified by employing the identities

$$-x_H^T Q_H x_H \leq -\lambda_{min}(Q_H)||x_H||_2^2 \tag{5.24}$$
$$-x_C^T Q_C x_C \leq -\lambda_{min}(Q_C)||x_C||_2^2 \tag{5.25}$$

where $\lambda_{min}(Q)$ denotes the minimal eigenvalue of Q and x_H can be separated into x_{L_h}, x_h by using

$$||x_H||_2^2 = ||x_{L_h}||_2^2 + x_h^2 \tag{5.26}$$
$$||x_C||_2^2 = ||x_{L_c}||_2^2 + x_c^2 \tag{5.27}$$

to finally yield

$$\dot{V} = \dot{V}_1 + \dot{V}_2 \tag{5.28}$$

with

$$\dot{V}_1 = 2x_{L_h}^T P_{L_h} B_H w + 2x_{L_c}^T P_{L_c} B_C w$$
$$- \lambda_{\min}(Q_H)||x_{L_h}||_2^2 - \lambda_{\min}(Q_C)||x_{L_c}||_2^2 \tag{5.29}$$

and

$$\dot{V}_2 = -\lambda_{\min}(Q_C)x_h^2 - \lambda_{\min}(Q_C)x_c^2$$
$$+ 2x_h P_h f_h^{NL}(x_h, x_c, u(v)) + 2x_c P_c v. \tag{5.30}$$

Since $\lambda_{\min}(Q) > 0$ for a positive definite matrix $Q \succ 0$ and the ambient air $w \geq 0$ is assumed to be bounded, the first term $\dot{V}_1$ can be assumed to be strictly smaller than 0. To conclude stability by ensuring that $\dot{V} < 0$ it must hold that $\dot{V}_2 < 0$.
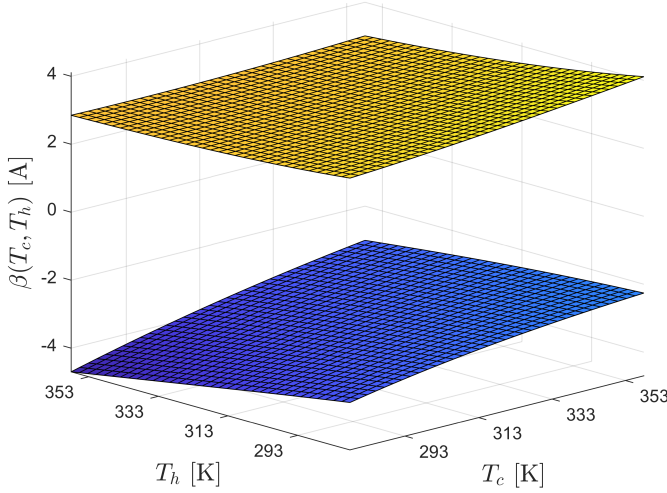
Figure 5.12. Temperature dependent bounds displayed as a surface for varying hot and cold side temperatures. Here, a positive current provides a flux from T_c to T_h, and it can be observed that when T_c is high, more cooling is allowed.

5.5.3. Temperature dependent stability bounds

The bound on $\dot{V}_2 < 0$ in (5.30), is solved for I to yield the following temperature dependent bounds on the allowable TEM current I [A]

$$\Phi : \beta_1(x_c, x_h) \le I \le \beta_2(x_c, x_h) \tag{5.31}$$

with

$$
\begin{aligned}
\beta_1(x_c, x_h) = \big((P_c^2 S_m^2 x_c^4 &+ 2K_m R_m P_c^2 x_c^3 \\
- 2K_m R_m P_c^2 x_c^2 x_h &- 2P_c P_h S_m^2 x_c^2 x_h^2 + R_m \lambda_{\min}(Q_C) P_c x_c^3 \\
+ R_m \lambda_{\min}(Q_h) P_c x_c x_h^2 &+ P_h^2 S_m^2 x_h^4 - 2K_m R_m P_h^2 x_c x_h^2 \\
+ 2K_m R_m P_h^2 x_h^3 &+ R_m \lambda_{\min}(Q_C) P_h x_c^2 x_h + \\
R_m \lambda_{\min}(Q_h) P_h x_h^3 \big)^{\frac{1}{2}} \\
+ P_c S_m x_c^2 - P_h S_m x_h^2 \big) &\big(P_c R_m x_c + P_h R_m x_h \big)^{-1}
\end{aligned}
\tag{5.32}
$$

and $\beta_2(x_c, x_h) = -\beta_1(x_c, x_h)$ and $S_m(T_{avg}), R_m(T_{avg})$ are the temperature dependent parameters. The bounds on v [W] can be derived using a similar approach.

     The bounds obtained in (5.31) are typically incorporated into the feedback linearization as a saturation bound on the TEM current. However, they can be
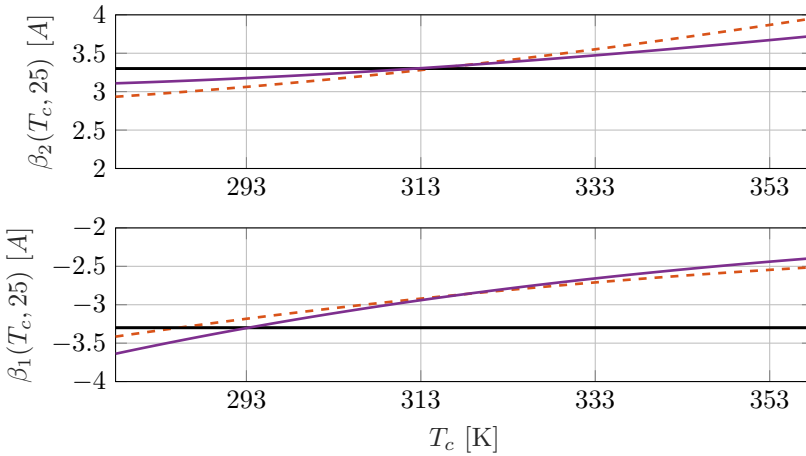
Figure 5.13. Stability bound assuming a hot side temperature of $T_h = 25$ [K] and varying cold side temperature T_c. The bounds are shown using constant parameters with $T_{avg} = 308$ [K] (- - -) and using temperature dependent parameters $T_{avg} = \frac{T_h + T_c}{2}$ (——). Incorporating temperature dependency changes the conservatism of the bounds, and at $T_{avg} = 308$ [K] the bounds are equal. The maximum current as specified by the manufacturer is ± 3.3 [A] (——).

included in a more advanced type of control, e.g., model predictive control, to apply the maximum allowable current given measured hot and cold side temperature. In Figure 5.12 the bounds in (5.31) are shown for varying T_h, T_c since they are temperature dependent. Moreover, the accuracy of the bounds is improved by including temperature dependent parameters $S_m(T_{avg}), R_m(T_{avg})$. In Figure 5.13 the bounds are shown for $T_h = 298$ [K] and a varying T_c, both for constant parameters $S_m(308), R_m(308)$ and temperature dependent parameters $S_m(T_{avg}), R_m(T_{avg})$. The results show that the bounds vary for different values of $T_{avg} = \frac{T_h + T_c}{2}$, and at $T_h = 318$ [K], i.e., $T_{avg} = 308$ [K], the bounds are equal.

Remark

The bounds in (5.31) can be conservative, as they form a sufficient but not necessary condition for stability. The amount of conservatism depends on the specific solution to the LMIs in (5.22).

5.5.4. Experimental validation

By employing the high-fidelity model obtained in Section 5.4 combined with the procedure provided in Section 5.6 the application setup is linearized. Leveraging

the feedback linearization law $\Psi(v,x)$ in (5.16) the system G_{lin}, as shown in Figure 5.11, is now linear from v [W] to $y = x_c$ [K].

To verify the effectiveness of the feedback linearization, a comparison of the systems step response with and without linearization is made for different step magnitudes.

Without linearization   The results without feedback linearization are shown in Figure 5.14, it shows both the step responses of different magnitudes and the normalized responses. The normalized responses in Figure 5.14b clearly show that the response varies with step magnitude. This indicates that the TEM system does not abide by the scaling principle of linear systems since the system is both state dependent and non-linear in the input.

With linearization   The results with feedback linearization, i.e., system G_{lin}, are shown in Figure 5.15. Again, step responses of different magnitudes are shown in Figure 5.15a that are then normalized and shown in Figure 5.15b. The normalized responses, and especially y_2, show significantly reduced correlation with the magnitude of the step. This illustrates that the system now behaves linearly in its input to output dynamics, thereby validating the effectiveness of the feedback linearization. Moreover, by including the temperature dependency of S_m, R_m in Ψ the linearization law is now valid over a significantly larger temperature range when compared to earlier results (Bos et al., 2018).

> **Remark**
>
> Alternatively, it is possible to analyze the extent of the non-linear residual after feedback linearization through an analysis as described in Schoukens et al. (2016). This is done using multiple experimental realizations to determine the Best Linear Approximation (BLA) of the transfer function G_{lin} in Figure 5.11 accompanied with the level non-linear distortions.

5.6. Observer design

In Section 5.5 an approach to feedback linearize the TEM based system is presented. This technique requires state information that is not always available. Moreover, in industrial applications it is often unwanted and sometimes impossible to attach numerous sensors to the TEM. Therefore, in this section, an observer based approach is presented. By combining a limited number of sensors with an internal model a state estimate is constructed.
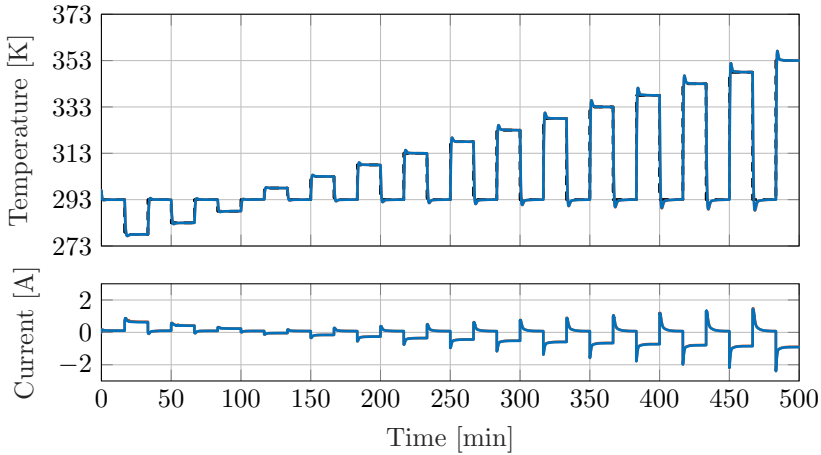
(a) Sequence of step responses for both module 1 y_1 (——) and module 2 y_2 (——) without using feedback linearization.
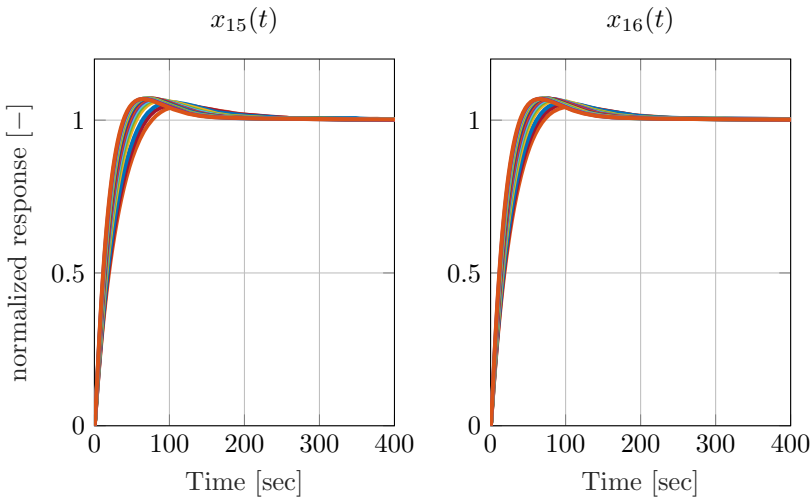
(b) Normalized step responses without using feedback linearization for both module 1 y_1 and module 2 y_2.

Figure 5.14. Normalized experimental step response without feedback linearization. The normalized step response varies with the amplitude of the step.
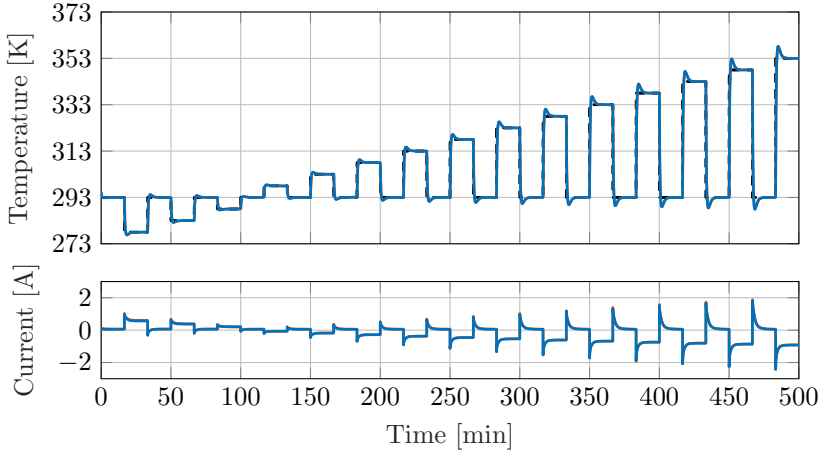
(a) Sequence of step responses for both module 1 y_1 (——) and module 2 y_2 (——) using feedback linearization.
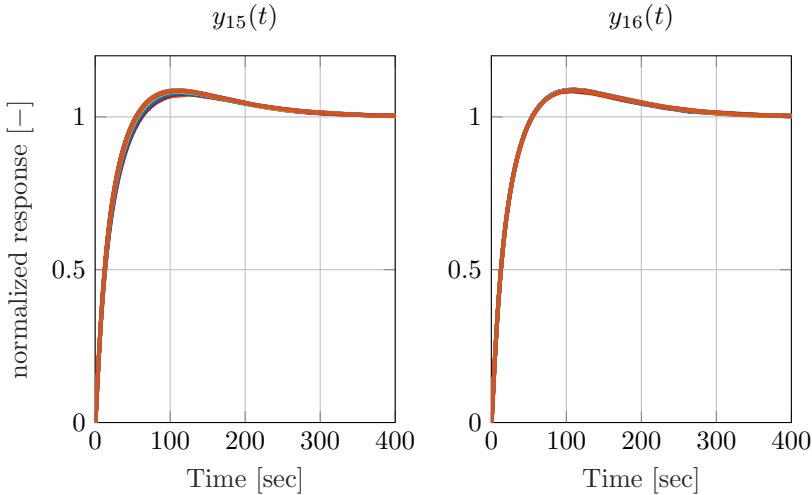
(b) Normalized step responses using feedback linearization for both module 1 y_1 and module 2 y_2.

Figure 5.15. Normalized experimental step response with feedback linearization. The normalized step response is almost completely invariant to the amplitude of the step, illustrating that the non-linear system is now linearized in input to output dynamics.

5.6.1. State Estimator

Consider again the system in (5.8) but now the linear conduction terms $K_m(x_{c,h} - x_{h,c})$ are combined into the A matrix. The mass matrix E can be taken to be unity or incorporated into the A and B matrices and f^{NL} by multiplying those contributions with the inverse of E. Moreover, the system is now described in discrete time by an appropriate transformation, e.g., Euler approximation. This yields

$$\begin{bmatrix} x(k+1)_{L_h} \\ x(k+1)_h \\ x(k+1)_c \\ x(k+1)_{L_c} \end{bmatrix} = A_d \begin{bmatrix} x(k)_{L_h} \\ x(k)_h \\ x(k)_c \\ x(k)_{L_c} \end{bmatrix} + B_d w(k) + \begin{bmatrix} \mathbf{0} \\ \alpha f_h^{NL} \\ \alpha f_c^{NL} \\ \mathbf{0} \end{bmatrix}$$

$$y(k) = C_d x(k) \tag{5.33}$$

as the state-space equations. Here, $A_d = (I + T_s A)$, $B_d = T_s B$, $f_h^{NL}(x_h, u) = S_m x_h u + \frac{1}{2} R_m u^2$, $f_c^{NL}(x_c, u) = S_m x_c u + \frac{1}{2} R_m u^2$ and $\alpha = T_s$ a scaling factor that is equal to the sampling time T_s for Euler approximation. The matrix C_d relates the outputs to the states. Moreover, it is equal $C_d = C$ to the output matrix in continuous time and dependent on the sensor placement in the setup.

To construct a state-estimator an additional innovation term is added to (5.33) to yield, with slight abuse of notation,

$$\hat{x}(k+1) = A_d \hat{x}(k) + B_d w(k) + f_{NL} + L(y(k) - C_d \hat{x}(k)) \tag{5.34}$$

where L is the observer gain and $\hat{x}$ the state estimate. The observer gain is designed such that the estimation error, $\tilde{x}(k) = x(k) - \hat{x}(k)$, dynamics are stable and converge within reasonable time. For a linear stable system, this can be always be achieved if the states can be reconstructed in the output of the systems, i.e., if they are observable. The observability of the states is confirmed, assuming the system is stable, using the Hautus test on the pair A_d, C_d. The estimation error $\tilde{x}$ dynamics are given by

$$\begin{bmatrix} \tilde{x}(k+1)_{L_h} \\ \tilde{x}(k+1)_h \\ \tilde{x}(k+1)_c \\ \tilde{x}(k+1)_{L_c} \end{bmatrix} = \underbrace{(A_d - LC_d)}_{A_o} \begin{bmatrix} \tilde{x}(k)_{L_h} \\ \tilde{x}(k)_h \\ \tilde{x}(k)_c \\ \tilde{x}(k)_{L_c} \end{bmatrix}$$

$$+ \operatorname{diag}\underbrace{\left(\begin{bmatrix} \mathbf{0} \\ S_m(T_{avg})u \\ -S_m(T_{avg})u \\ \mathbf{0} \end{bmatrix} \right)}_{F_o^{NL}} \begin{bmatrix} \tilde{x}(k+1)_{L_h} \\ \tilde{x}(k+1)_h \\ \tilde{x}(k+1)_c \\ \tilde{x}(k+1)_{L_c} \end{bmatrix} \tag{5.35}$$

where A_o are the linear error dynamics and F_o^{NL} the non-linear contribution that includes the state-dependent elements of f_{NL} in (5.34).

5.6.2. Observer gain

The observer in (5.34) is constructed as a linear-quadratic estimator (LQE), i.e., a Kalman filter. To determine the observer gain L that projects $(y(k) - C_d \hat{x})$ onto the state estimate $\hat{x}$ a discrete algebraic Ricatti equation is solved. Given a discrete system

$$x(k+1) = Ax(k) + Bu(k) + Gw(k) \tag{5.36}$$
$$y(k) = Cx(k) + Du(k) + Hv(k) \tag{5.37}$$

and noise covariance matrix of the process and measurement noise respectively given by

$$Q = E(w(k)w(k)^T), R = E(v(k)v(k)^T) \tag{5.38}$$

the gain matrix L can be derived by solving a discrete-time algebraic Riccati equation

$$L = (APC^T + Q)(CPC^T + \bar{R})^{-1} \tag{5.39}$$

where

$$\bar{R} = R + HQH^T \tag{5.40}$$

assuming that $v(k)$ and (w) are uncorrelated, i.e., $E(w(k)v(k)^T) = 0$.

5.6.3. Stability

In the typical application of the LQE, stability of the estimation error $\tilde{x}$ dynamics is ensured by evaluating the eigenvalues of $A_o = A_d - LC_d$. However, in the current application this is not sufficient since F_o^{NL} also influences the estimation error as seen in (5.35), making the system non-linear.

To verify stability of the observer structure employed in this chapter, a Lyapunov cadidate function is constructed as

$$V(\tilde{x}(k)) = \tilde{x}(k)^T P \tilde{x}(k) \tag{5.41}$$

with $P \in \mathbb{R}^{n_x \times n_x} \succ 0, P^T = P$. The discrete time derivative of $\Delta V(\tilde{x}(k)) = V(\tilde{x}(k+1) - V(\tilde{x}(k))$ is given by

$$\tilde{x}(k)^T((A_o + F_o^{NL})^T P(A_o + F_o^{NL}) - P)\tilde{x}(k) \tag{5.42}$$

that must be negative for all $\tilde{x}$ to ensure stability. This is equivalent to

$$(A_o + F_o^{NL})^T P(A_o + F_o^{NL}) - P \prec 0 \tag{5.43}$$

or

$$A_o^T P A_o - P \prec -(F_o^{NL})^T P F_o^{NL}. \tag{5.44}$$

Clearly, the matrix F_o^{NL} is a function of $S_m(T_{avg})$, which is temperature dependent, and the input u. To provide stability against a worst case F_o^{NL} a lower bound on F_o^{NL} is calculated by using the inequality

$$- \lambda_{max}((F_o^{NL})^T P F_o^{NL}) ||\tilde{x}(k)||_2^2 \leq$$
$$- \tilde{x}^T((F_o^{NL})^T P F_o^{NL}) \tilde{x}(k). \tag{5.45}$$

Using this inequality it is possible to determine the worst case F_o^{NL} by determining the maximum eigenvalue $\lambda_{max}(F_o^{NL})$ over a range of T_{avg} and u. Moreover, since F_o^{NL} is diagonal, see (5.35), its eigenvalues are determined by the entries on the diagonal itself. Therefore, the maximum eigenvalue is obtained using $S_M(T_{avg})$ with $T_{avg} = 328$ [K] Celsius, where S_m is largest as shown in Figure 5.9, and $u = 4$ [A] which is well above the admissible current for the TEM. This then yields a worst case scenario bound for F_o^{NL} that is incorporated in (5.43). Stability of the estimation error $\tilde{x}(k)$ is then achieved if a solution is found to the set of LMIs in (5.43) using F_o^{NL} with the worst case parameters as determined by the lower bound in (5.45). If the LMIs in (5.43) can not be solved for a given observer gain L, stability can not be guaranteed and the design should be reconsidered by redesigning L. In Bos et al. (2020), an Extended Kalman Filter (EKF) is used as a non-linear state estimator. While the approach achieves accurate results, a stability guarantee remains challenging.

Remark

Analogous to the stability of the feedback linearization in Section 5.5, a solution to the LMIs (5.43) is only a sufficient and not a necessary condition for stability of the estimation error dynamics.

5.6.4. Experimental validation

In this section an observer, as described in Section 5.6, is used to form a state reconstruction $\hat{x}$ using a limited set of sensors on the setup shown in Figure 5.1. More precisely, only sensors on x_6 and x_7, as shown in Figure 5.3, are used and the other sensors are used to evaluate the state reconstruction error.

In Figure 5.16 the results for 2 separate experiments are shown. For both module 1, with results in Figure 5.16a, and module 2, with results in Figure 5.16b, a sequence of step excitations is used. In the bottom half of the figures the reconstruction error $\tilde{x} = x - \hat{x}$ is shown, where x are the measured states and $\hat{x}$ the reconstruction made by the observer. It can be seen that the reconstruction error is quite small over the full temperature range. Moreover, the results are in the same order of magnitude as those shown in Figure 5.10b, indicating that the reconstruction by the observer is accurate up to the accuracy of the underlying model.
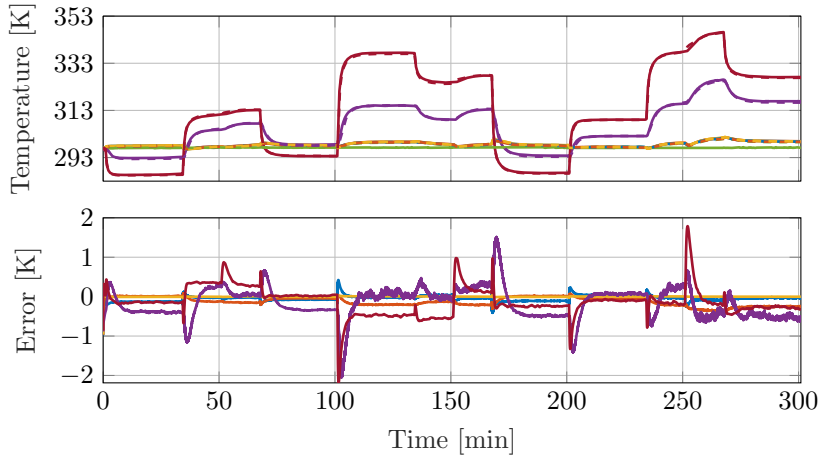
(a) Peltier 1 with measured (solid) and observed (dashed) states $\hat{x}_3$ (—), $\hat{x}_5$ (—), $\hat{x}_6$ (—), $\hat{x}_{13}$ (—), $\hat{x}_{15}$ (—) and corresponding prediction error and the water cooling temperature w_{env} (—).
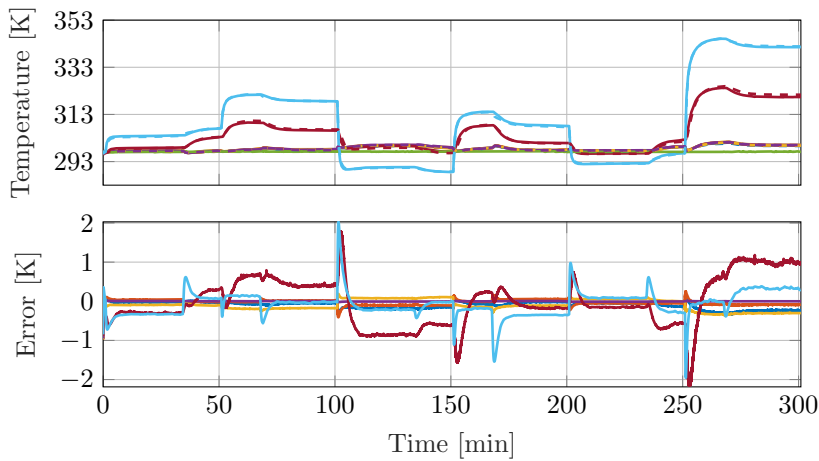
(b) Peltier 2 with measured (solid) and observed (dashed) states $\hat{x}_2$ (—), $\hat{x}_4$ (—), $\hat{x}_8$ (—), $\hat{x}_7$ (—), $\hat{x}_{18}$ (—), $\hat{x}_{16}$ (—) and the water cooling temperature w_{env} (—).

Figure 5.16. State reconstruction error using an observer and 2 temperature sensors on x_6, x_7.

5.7. Conclusion

Advanced thermal control is a crucial area of research and development, especially in the medical, high-power lighting, and semiconductor industry. Controlling thermal dynamics using heater based actuators is inherently limited since they can only provide a positive heat flux. Using thermoelectric elements alleviates these limitations by providing active temperature control capable of both heating and cooling. This chapter presents a full framework for modeling and control of thermoelectric elements. Using temperature dependent parameters yields a high-fidelity first principles model suitable for control. Using feedback linearization combined with a Kalman filter observer facilitates advanced control with a limited number of temperature sensors. It is shown that the framework yields accurate models and reliable control strategies suitable for a large temperature range.

5.A. State-Space Matrices

A full numerical model for the application setup shown in Figure 5.1 can be constructed by using the structure in (5.8) and details from Section 5.2 with the numerical matrices provided in (5.46)-(5.47).

5

$$
A_H =
\begin{bmatrix}
-8.342 & 0 & 7.648 & 0 & 0 & 0 & 0 & 0 & 0 & 0 \\
0 & -8.342 & 0 & 7.648 & 0 & 0 & 0 & 0 & 0 & 0 \\
7.648 & 0 & -25.11 & 6.528 & 0 & 10.93 & 0 & 0 & 0 & 0 \\
0 & 7.648 & 6.528 & -27.39 & 0 & 0 & 13.22 & 0 & 0 & 0 \\
0 & 0 & 0 & 0 & -1.945 & 1.076 & 0 & 0.7344 & 0 & 0 \\
0 & 0 & 10.93 & 0 & 1.076 & -25.58 & 0.408 & 0 & 13.17 & 0 \\
0 & 0 & 0 & 13.22 & 0 & 0.408 & -28.74 & 1.953 & 0 & 13.17 \\
0 & 0 & 0 & 0 & 0.7344 & 0 & 1.953 & -2.822 & 0 & 0 \\
0 & 0 & 0 & 0 & 0 & 13.17 & 0 & 0 & -13.17 & 0 \\
0 & 0 & 0 & 0 & 0 & 0 & 13.17 & 0 & 0 & -13.17
\end{bmatrix}
$$

$$
A_C =
\begin{bmatrix}
-9.096 & 0 & 9.096 & 0 & 0 & 0 & 0 & 0 & 0 & 0 \\
0 & -9.096 & 0 & 9.096 & 0 & 0 & 0 & 0 & 0 & 0 \\
9.096 & 0 & -0.2644 & 0.216 & 0 & 9.096 & 0 & 0 & 0 & 0 \\
0 & 9.096 & 0.216 & -0.3742 & 0.1098 & 0 & 0.01944 & 0 & 0 & 0 \\
0 & 0 & 0 & 0.1098 & -9.235 & 0.02592 & 0 & 0 & 0 & 0 \\
0 & 0 & 9.096 & 0 & 0.02592 & -9.228 & 0.1029 & 0 & 0 & 0 \\
0 & 0 & 0 & 0.01944 & 0 & 0.1029 & -0.3673 & 0.216 & 0 & 0 \\
0 & 0 & 0 & 0 & 0 & 0 & 0.216 & -0.2644 & 0.01944 & 0 \\
0 & 0 & 0 & 0 & 0 & 0 & 0 & 0 & 0 & 0 \\
0 & 0 & 0 & 0 & 0 & 0 & 13.17 & 0 & 0 & -0.2644
\end{bmatrix}
$$

$$
E = \mathrm{diag}\left(
\begin{bmatrix}
40.605 & 40.605 & 57.524 & 57.524 & 21.656 & 12.994 & 12.994 & 21.656 & 4.7832 \\
4.7832 & 4.7832 & 9.6826 & 9.6826 & 9.6826 & 11.619 & 11.619 & 9.6826 & 4.7832 & 9.6826
\end{bmatrix}
\right)
$$

$$
B_H = [0.6942 \;\; 0.6942 \;\; 0 \;\; 0.1345 \;\; 0 \;\; 0.1345 \;\; 0 \;\; 0 \;\; 0 \;\; 0.0028 \;\; 0.0028 \;\; 0 \;\; 0 \;\; 0 \;\; 0.0290 \;\; 0.0290 \;\; 0 \;\; 0.0290 \;\; 0.0290 \;\; 0]^T
$$

$$
B_C = [0 \;\; 0 \;\; 0.0290 \;\; 0.0290 \;\; 0.0028 \;\; 0.0028 \;\; 0 \;\; 0 \;\; 0.0290 \;\; 0.0290 \;\; 0 \;\; 0 \;\; 0 \;\; 0 \;\; 0 \;\; 0 \;\; 0.0290]^T
$$

(5.46)

$$F^{NL}(x,u) = \begin{bmatrix} 0^{1\times 8} \\ K_{m_1}(x_{11} - x_9) + \frac{1}{2}R_{m_1}u^2 + S_{m_1}x_9 u \\ K_{m_2}(x_{12} - x_{10}) + \frac{1}{2}R_{m_2}u^2 + S_{m_2}x_{10}u \\ K_{m_1}(x_9 - x_{11}) + \frac{1}{2}R_{m_1}u^2 - S_{m_1}x_{11}u \\ K_{m_2}(x_{10} - x_{12}) + \frac{1}{2}R_{m_2}u^2 - S_{m_2}x_{12}u \\ 0^{1\times 6} \end{bmatrix}$$

(5.47)

$$C = \text{diag}([1\ 0\ 1\ 1\ 1\ 1\ 1\ 0\ 0\ 0\ 1\ 0\ 1\ 1\ 0\ 1])$$

$$S_{m_1} = 0.049087 + 0.000056877 \cdot \frac{x_9 + x_{11}}{2}$$

$$S_{m_2} = 0.049283 + 0.000079559 \cdot \frac{x_{10} + x_{12}}{2}$$

$$R_{m_1} = 3.4125 + 0.024323 \cdot \frac{x_9 + x_{11}}{2}$$

$$R_{m_2} = 3.4034 + 0.022387 \cdot \frac{x_{10} + x_{12}}{2}$$

$$K_{m_1} = 0.31655304537776$$

$$K_{m_2} = 0.32542045701943$$

CHAPTER 6

Beyond Decentralized Wafer/Reticle Stage Control Design: A Double-Youla Approach For Enhancing Synchronized Motion [1]

Abstract: Industrial waferscanners often consists of multiple subsystems. Traditionally, these systems-of-systems are divided into manageable subproblems at the expense of the overall performance, that is determined by the synchronicity of the motions of the subsystems. The aim of this chapter is to enhance overall system performance by posterior coupling of the controlled subsystems. A framework that relates to the Youla parameterization is developed that connects the additional control elements affinely to the overall system performance criterion. The resulting framework parametrizes all stabilizing bi-directional coupling controllers, and enables improved performance. Robust stability is subsequentially addressed through a double-Youla approach. Application to a wafer scanner confirms superior performance of the joint wafer stage and reticle stage performance, while maintaining full system robust stability.

6.1. Introduction

Many mechatronic systems in the manufacturing industry consist of multiple subsystems that jointly contribute to achieve a certain overall performance. Examples of such systems-of-systems include waferscanners used in the lithographic industry (Butler, 2011), where the wafer stage and reticle stage synchronization is critical to achieve the required overlay performance; gantry and carriage platforms such as large scale industrial printers (Bolder, 2015), where performance of both subsystems is directly related to the print quality; and roll-to-roll processing plants, where synchronization between rolls is required for correct deposition of the layer material (Chen et al., 2016). In all these cases, the relative positioning of the subsystems defines the overall system performance.

The design and control of these systems-of-systems is traditionally divided into tractable subproblems with error budgets (Jabben and van Eijk, 2011). Typically, the subsystems aim at a certain absolute positioning accuracy, together these then imply good relative positioning of the subsystems. The main reason is that the overall design problem is too complex to be handled by manual controller design. In fact, already for a single multivariable subsystem a centralized design often is too complex (Oomen, 2018), and by far, the majority of the industrial control systems are still controlled by traditional decentralized PID controllers. Veritably, typical motion control guidelines in Oomen (2018) reveal that control performance and modeling effort should be well-balanced, typically leading to PID controllers by utilizing decentralized controller structures and non-parametric frequency response functions.

In the typical case where the control design is divided into manageable subproblems, the overall performance of the system is limited by the worst-case performance of the subsystems. In turn, the worst case performance is determined by the performance limitations associated with the individual subsystems (Seron et al., 1997). Typically, these subsystems are scalar or at least controlled in decentralized loops using a local performance measure. This is commonly done to facilitate decentralized design, where each module is designed and controlled using its own specifications and error budget. This decomposition of the overall system leads to newly introduced performance limitations. For instance, the definition of Single-In-Single-Out (SISO) subsystems leads to new zeros, which can be non-minimum phase and directly introduce performance limitations. Indeed, this introduction of zeros is well-known and well-understood from squaring down (Maciejowski, 1989). In sharp contrast, the full system using an overall performance criterion often has much less performance variables compared to the number of inputs, in which case the overall system using the global performance criterion generally does not exhibit these NMP zeros. Indeed, non-square systems generally have no such performance limiting zeros (Freudenberg et al., 2003; Van Zundert et al., 2018), and hence exploiting the freedom in the controller architecture in conjunction with the overall performance goal may

alleviate traditional performance limitations.

The aim of this chapter is to improve the combined system performance while maintaining the original decentralized design and control structure. This allows for superior performance in the overall performance criterion, while maintaining the original controller design approach for the controlled variables. This is achieved by: 1) additional add-on coupling elements to the existing decentralized control structure, and 2) optimizing these control elements for a full system performance criterion.

The potential and industrial acceptance of add-on controller extensions has been confirmed in several preliminary ad hoc experimental studies. Research examples of improved synchronization by advanced feedforward can be found in Navarrete et al. (2015), see also Boeren et al. (2014) for related feedforward results. In Barton and Alleyne (2007) and Mishra et al. (2008) improved synchronization is achieved by using iterative learning control. Rational filters are used in direct feedback of the relative error in Wang et al. (2006). Typically, in these experimental studies the controller is extended by a one-way coupling. Such unidirectional interaction is also considered in Sakata and Fujimoto (2009) using rational filters and Heertjes and Temizer (2012) using data-based optimization of FIR filters. Bi-directional interaction allows for inherently better performance due to a larger design freedom. However, bi-directional coupling affects closed-loop stability (Skogestad and Postlethwaite, 2009), which is not the case for unidirectional coupling. In, Looijen and Heertjes (2018) closed-loop stability is analyzed using a multivariate Nyquist criterion which can be challenging to interpret.

Although several attempts to improve overall system performances have been made, at present no systematic framework is available for the design of bi-directional controller coupling that is applicable to synchronized motion control. In this chapter the potential enhancement is shown through fundamental analysis and a generalized framework is developed that achieves this performance gain by connecting the add-on controller elements to the true performance criterion.

The main contribution of this chapter is a control design for coupling in decentralized controllers which is illustrated on a highly complex, high performance motion system. The following sub-contributions are identified.

C1 A framework that facilitates systematic design and analysis of nominal add-on coupling filters to achieve improved overall system performance. In addition, it encompasses all present approaches outlined above as a special case.

C2 Design guidelines for coupling filter synthesis, suitable for both norm-optimal ($\mathcal{H}_2, \mathcal{H}_\infty$) design and manual tuning, where the latter facilitates industrial implementation (Van de Wal et al., 2002).

C3 An extension that appropriately addresses robust stability by considering model uncertainty bounds.

C4 A case study of an industrial wafer scanner is presented, where both nominal performance and robust performance are investigated.

In Evers et al. (2017), a preliminary version addressing in part 6.1, 6.1 is presented. The present chapter extends this to a more general setting containing more detailed proofs and explanation, and, in addition, 6.1, 6.1. Research related to results presented here includes Barton and Alleyne (2007); Heertjes and Temizer (2012); Lambregts et al. (2015); Navarrete et al. (2015); Sakata and Fujimoto (2009).

  The framework guarantees robust stability under uncertainty in the system dynamics, finite accuracy of the plant model and neglected subsystem interaction components. The presented framework provides a systematic design based on several Youla-type parameterizations that in turn depend on coprime factorizations. The approach relates to coprime factorization based Youla result in Tay et al. (1998), see also Chen et al. (2015); Oomen et al. (2014a). The proposed framework provides a basis for general control design methodologies ranging from manual tuning to $\mathcal{H}_2/\mathcal{H}_\infty/\mu$-based optimal control. For clarity and brevity of the exposition the framework is presented for a 2×2 SISO case. The framework can be directly applied to MIMO systems along conceptually similar lines. Moreover, it is assumed that the contribution of the additional coupling controllers to the actuator signal is relatively small. For the considered wafer scanner application, this assumption is valid, the control input predominantly consists of feedforward inputs (De Gelder et al., 2006). Therefore, non-linear effects such as dead-zones, saturation, and anti-windup (Prempain et al., 2009) are considered beyond the scope of this chapter.

6.2. Motivation and problem formulation

In this section, the problem considered in this chapter is formulated. First, a motivating case study is presented, followed by the specification of the requirements and control goal.

6.2.1. Industrial wafer scanner: the role of the reticle stage and the wafer stage

The potential performance benefit of the additional controller freedom due to the coupling elements is exploited in an industrial case study. The following section presents the considered system, the industrial context and the control challenges.

  The case study considered in this chapter is an industrial waferscanner, as shown in Figure 6.1. A waferscanner is used in the lithographic step in the production process of integrated circuits. An abstract representation of the considered moving stages, the reticle stage and wafer stage, is shown in Figure 6.2.
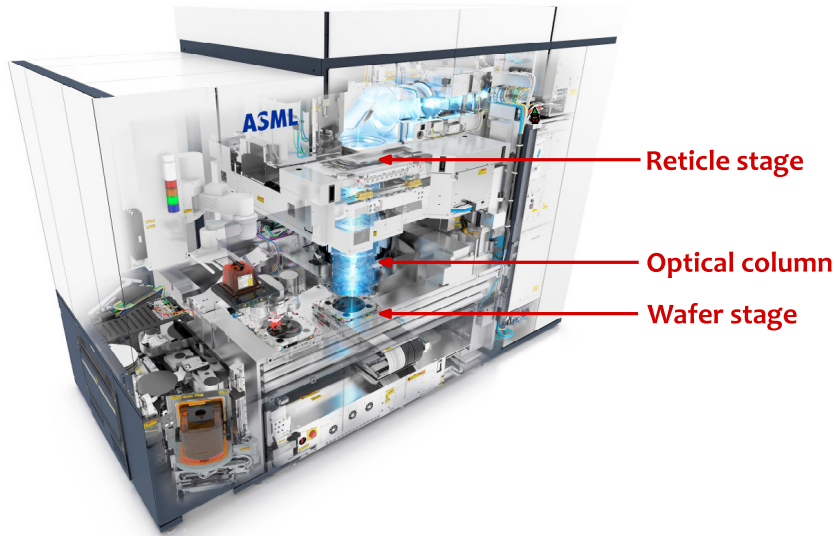
Figure 6.1. Artist impression of a wafer scanner, an industrial production machine used in the lithographic industry.

During the exposure step of the lithographic process, light, typically with a wavelength of approximately 14 nm in state-of-the-art equipment, travels from a source, located outside the machine, through the reticle. The reticle contains the image of the to be produced IC and the beam is projected through the optical column onto a light-sensitive layer on the wafer. The illuminated photoresist is subsequently removed using a chemical solvent. Further chemical processing enable etching of the exposed patterns, which is repeated for each subsequent layer. Approximately 20 layers are required to form each wafer. The final wafer, a silicon disk with a diameter of 300 mm, contains multiple projected and scaled copies of the image contained in the reticle. During the exposure process, the wafer stage must track a challenging reference trajectory in all six motion degrees-of-freedom (DoF). The key performance requirement is a synchronized motion between the reticle and the wafer. Indeed, a synchronized motion is essential for avoiding focus and overlay errors. Hence, the true performance criterion is the relative positioning error between the two stages.

State-of-the-art wafer scanner control: To facilitate development, the wafer stage and reticle stage controllers are designed separately. Here, the control objective is to obtain the smallest tracking error in all six DoF for each of the individual stages. At present, the design of this controller is simplified by applying a decoupling procedure. This allows the use of SISO PID controllers
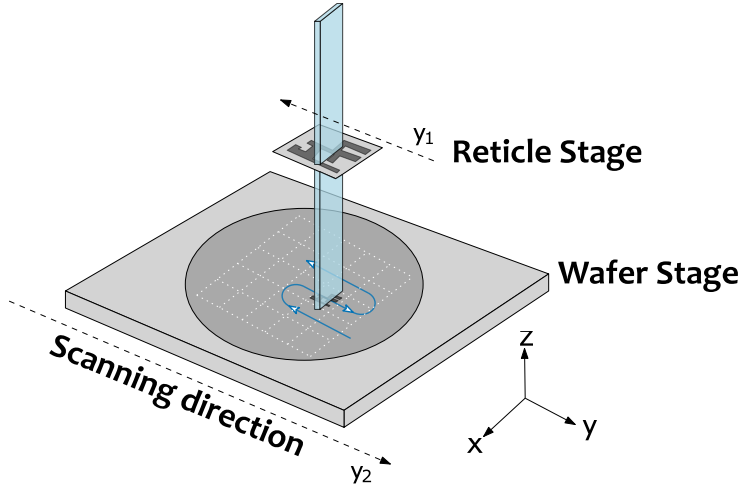
Figure 6.2. Abstract representation of the reticle stage and wafer stage. The optical column is disregarded for simplicity. Here, the true performance criterion is the relative error $e_{12} = y_2 - y_1$.

for each of the individual DoF (Butler, 2011). Centralized approaches, including model based $\mathcal{H}_\infty$ robust control (Oomen et al., 2014b; Van de Wal et al., 2002) often cannot be justified due to very high modeling requirements. This illustrates that a fully centralized approach for a single subsystem is challenging, moreover, a fully centralized approach encompassing both subsystems, the reticle stage and wafer stage, is infeasible.

Performance limitations introduced by subdivision: At present, decoupling procedures are often used to facilitate SISO controller design for MIMO systems. While this simplifies the control architecture, it also introduces the possibility of performance limitations. This is shown by adopting the case study and constraining it to a single DOF, i.e., both the reticle and wafer stage are considered in the scanning direction only, i.e., along the y-axis as shown in Figure 6.2. The control objective is to improve the combined performance of the two stages to best attenuate all disturbances present on both the reticle and wafer stage. To simplify the presentation, two aspects are tacitly omitted from the explanation that are explicitly and appropriately dealt with in the actual implementation. First both the plant and controller are considered in discrete time, and the framework is tacitly adjusted to this situation. Second, in the waferscanner the reticle stage output is scaled by an optical scaling factor γ that accounts for the optical lens reduction (Butler, 2011). This factor is omitted to facilitate the presentation.

Consider the reticle stage and wafer stage synchronized movement, shown in
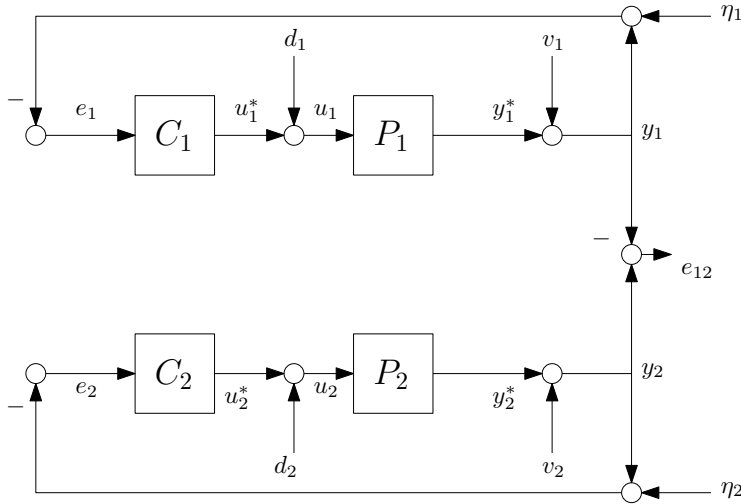
Figure 6.3. Decentralized control structure for the double positioning stage system, cast into a disturbance attenuation problem. It is assumed that any referenced induced tracking error is compensated by advanced feed-forward techniques.

Figure 6.2. Here, the two positioning stages are controlled using a decentralized approach shown in Figure 6.3. Here, the problem is restricted to feedback, where stability is a key issue. Feedforward can be directly induced (Oomen et al., 2015). While the individual stage tracking errors are important and must remain bounded, the true performance criterion is the relative positioning error

$$e_{12} = y_2 - y_1 \qquad (6.1)$$

where y_1 [m] and y_2 [m] are the positions of the first and second positioning stage respectively.

The subsystems shown in Figure 6.3 are considered to be approximately decoupled (Stoev et al., 2016), i.e., it is assumed that there is no interaction between subsystems. An extension that includes this neglected interaction is presented in Section 6.5. While each of the subsystems typically is controlled in 6 DoF, in the scanning direction the combined system can be modeled as a 2×2 diagonal plant and controller

$$P = \begin{bmatrix} P_1 & 0 \\ 0 & P_2 \end{bmatrix}, \quad K_0 = \begin{bmatrix} C_1 & 0 \\ 0 & C_2 \end{bmatrix}. \qquad (6.2)$$

The main objective is to construct add-on elements to K_0 that maintains the original decentralized controllers C_1, C_2 while improving the overall system performance (6.1).

Motivation: beyond traditional performance limitations: The additional add-on controller freedom is used to achieve combined system performance beyond the limitations of the decentralized individual subsystems. One of these limitations is nonminimum-phase (NMP) zeros. If P_1 contains a NMP zero, control performance in this loop is limited, which is directly apparent, e.g., from a Poisson integral relation (Freudenberg et al., 2003), and therefore the overall system performance is limited. Typically, these zeros originate from non-collocated sensor and actuator placement (Hong and Bernstein, 1998) and sampling (Åström et al., 1984).

Further limitations may result from Bandwidth (BW) limitations due to uncertainty or varying dynamics (Van Herpen et al., 2014). Typically, the wafer stage can achieve a lower BW compared to the reticle stage. Through the framework developed here, disturbances occurring in one subsystems can be compensated by the other systems in terms of the synchronized motion.

Assumption 6.1. *Throughout, a high performance decentralized, stabilizing controller is assumed to be present and fixed. Such that, if the coupling is disabled then the original system is recovered.*
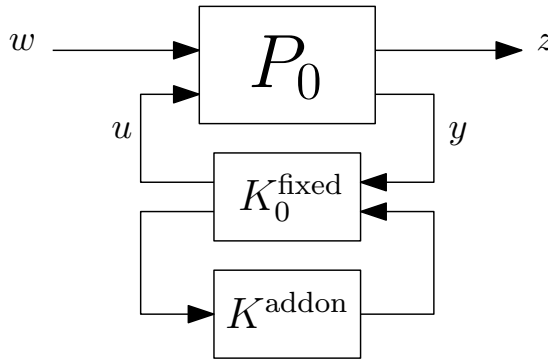
Figure 6.4. Standard plant representation, often used in cases where the performance variables z are not equal to the controlled variables y. Here K_0^{fixed} is the fixed diagonal controller in view of Assumption 6.1 and K^{addon} is the proposed addon controller.

Consider the system in Figure 6.3 that is cast into the standard plant in Figure 6.4. Here $y = [e_1, e_2]^T$, $u = [u_1, u_2]^T$ and $w = [v_1, v_2]^T$. In addition, for simplicity $\eta_1 = \eta_2 = d_1 = d_2 = 0$. Next, consider two cases that each define a different performance variable z. In particular z is chosen 1) traditionally $z_1 = [e_1, e_2]^T$ or 2) as is proposed here, $z_2 = e_{12} = [e_1 - e_2]$.

Traditional: The traditional approach is focused on minimizing e_1 and e_2 separately. The controllers C_1 and C_2 are designed accordingly, leading to a closed-

loop sensitivity that can be written as

$$\begin{bmatrix} e_1 \\ e_2 \end{bmatrix} = - \underbrace{\begin{bmatrix} S_1 & 0 \\ 0 & S_2 \end{bmatrix}}_{T_{zw_1}} \begin{bmatrix} v_1 \\ v_2 \end{bmatrix}. \tag{6.3}$$

where S_1 and S_2 are the closed-loop sensitivity functions. As a result, the synchronization error is $e_{12} = S_1 e_1 - S_2 e_2$, and if either P_1 or P_2 contain performance limitations, e.g., NMP zeros, then the synchronization performance is reduced.

Proposed: The central idea is to consider

$$e_{12} = - \begin{bmatrix} I & -I \end{bmatrix} \begin{bmatrix} S_1 & S_{12} \\ S_{21} & S_2 \end{bmatrix} \begin{bmatrix} v_1 \\ v_2 \end{bmatrix} \tag{6.4}$$

$$= \underbrace{\begin{bmatrix} (S_{21} - S_1) & (-S_{12} + S_2) \end{bmatrix}}_{T_{zw_2}} \begin{bmatrix} v_1 \\ v_2 \end{bmatrix} \tag{6.5}$$

and to minimize $z_2 = e_{12}$ directly.

The main idea is to design coupling controllers to appropriately shape S_{12} and S_{21}, given the existing decentralized designs. This shows that the performance of the full system in T_{zw_2} is no longer limited by the subsystems, as S_{12} and S_{21} can be used to achieve complementary performance in regions where S_1 and S_2 are limited by, e.g., NMP zeros.

6.2.2. Requirements

Section 6.2.1 reveals that controller extension in conjunction with an overall control objective conceptually allows an increase in achievable performance. The main objective of this chapter is to improve the synchronized motion of the wafer and reticle stage by designing a framework for add-on controller performance improvement in view of the overall control goal. Fully exploiting this potential in a practically applicable design procedure leads to the following additional requirements.

1. The additional coupling filters must be "add-on" to the existing architecture in view of Assumption 6.1.

2. Nominal stability of the coupled system is guaranteed.

3. Robust stability in the presence of model uncertainty is guaranteed.

The interpretation of the above is the following: Requirement 1 ensures that the additional coupling filters do not interfere with the existing decentralized

control architecture. Hence, they can be turned off at any time to recover the pre-existing stabilizing feedback controller in Assumption 6.1 such that the traditional controller design, tuning and implementation can be retained. Moreover, by Requirement 2 stability of the original individual subsystems must be guaranteed. Bi-directional coupling leads to potential stability issues (Maciejowski, 1989) hence additional stability requirements should be fulfilled. Finally, Requirement 3 is posed such to ensure robust stability of the system under model uncertainties and disturbances. Uncertainties include finite model accuracy, varying plant dynamics, and interaction within and between subsystems.

Achieving performance beyond individual stage limits can be transparently done by connecting the add-on controller freedom with the new performance criterion e_{12}, which is proposed in this chapter.

6.3. Synchronized motion control: Youla framework

Bi-directional coupling leads to inherent two-way interaction and hence system characteristics such as well-posedness and internal stability require a detailed analysis (Maciejowski, 1989). In this section, the standard Youla parameterization is presented that, together with specific choices, leads to the coupling framework that allows systematic coupling of the subsystems while guaranteeing overall system stability. Furthermore, it will be systematically expanded in Section 6.5 to encompass model uncertainties. Throughout, the subsystems are tacitly assumed scalar and decoupled for clarity and brevity of the exposition. The presented approach directly extends to the MIMO case.

6.3.1. Standard Youla parameterization

To guarantee nominal stability the Youla parameterization (Anderson, 1998; Youla et al., 1976) is employed. Here, the Youla parameterization generates the set of all stabilizing controllers for a nominal system $P_0 \in \mathcal{R}$ as a function of a nominal controller $K_0 \in \mathcal{R}$ and a Youla parameter $\Delta_k \in \mathcal{RH}_\infty$. This allows for direct separation and analysis of the nominal controller K_0 and the additional add-on controller freedom captured by Δ_k. Here, both the nominal controller $K_0 = N_k D_k^{-1}$ and nominal plant $P_0 = N_p D_p^{-1}$ are represented as right-coprime factorizations. The control structure diagram of the Youla parameterization using coprime factorization is shown in Figure 6.5.

A right coprime factorization is defined as follows.

Definition 6.2 (Right-coprime factorization (rcf))**.** *The ordered pair* $\{N, D\}$, *with* $D \in \mathcal{RH}_\infty^{q \times q}$ *and* $N \in \mathcal{RH}_\infty^{p \times q}$, *is a right-coprime factorization (rcf) of* $P \in \mathcal{R}_\infty^{p \times q}$ *if*

(i) D is invertible (square and non-singular),
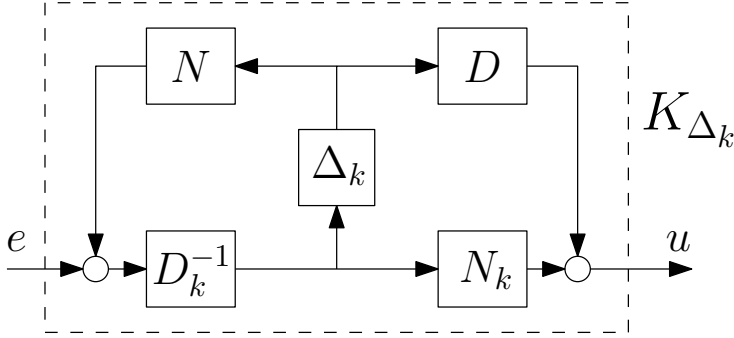
Figure 6.5. Controller diagram of a Youla parameterization using coprime factorization. Here, each element is a (2×2) transfer function matrix.

(ii) $P = ND^{-1}$,
(iii) N *and* D *are right-coprime.*

Here, N and D are right-coprime if there exist matrices $W, L \in \mathcal{RH}_\infty$ such that the Bezout identity (Zhou et al., 1996)

$$LN + WD = I, \qquad (6.6)$$

holds. Using the coprime factorizations of the nominal controller and plant, the Youla parameterization provides the set of stabilizing controllers.

Theorem 6.3 (Set of stabilizing controllers)**.**
Let $P_0 = N_p D_p^{-1}$ *and* $K_0 = N_k D_k^{-1}$ *where* $\{N_p, D_p\}$, $\{N_k, D_K\}$ *are rcfs of* P_0 *and* K_0. *Let the perturbed controller factors be defined as*

$$N_{k_\Delta} := N_k + D_p \Delta_k, \quad D_{k_\Delta} := D_k - N_p \Delta_k \qquad (6.7)$$

such that

$$K_{\Delta_k} = N_{k_\Delta} D_{k_\Delta}^{-1} \qquad (6.8)$$

where Δ_k *is the free Youla parameter. Then it follows that* K_{Δ_k} *stabilizes* P_0 *iff* $\Delta_k \in \mathcal{RH}_\infty$.

See, e.g., Zhou et al. (1996) for a proof.

6.3.2. Towards stabilizing bi-directional controller coupling

A bi-directional controller coupling is developed, where closed-loop stability follows through a direct connection to the Youla parameterization. Several specific choices are made that lead to favorable closed-loop system characteristics in view

of requirements in Section 6.2.2. In the common situation where $K_0 \in \mathcal{RH}_\infty$ in industrial applications, then

$$K_0 = \overbrace{\begin{bmatrix} C_1 & 0 \\ 0 & C_2 \end{bmatrix}}^{N_k} \overbrace{\begin{bmatrix} I & 0 \\ 0 & I \end{bmatrix}^{-1}}^{D_k^{-1}}, \tag{6.9}$$

where C_1, C_2 are the original decentralized controllers, is a suitable RCF. If C_1 or C_2 is unstable or has integral control action, i.e., poles on the imaginary axis, a suitable factorization should be constructed, e.g., see Vinnicombe (2000). Similarly, the nominal plant P_0 is written as

$$P_0 = \overbrace{\begin{bmatrix} Z_1 & 0 \\ 0 & Z_2 \end{bmatrix}}^{N_p} \overbrace{\begin{bmatrix} P_1^{-1} Z_1 & 0 \\ 0 & P_2^{-1} Z_2 \end{bmatrix}^{-1}}^{D_p^{-1}}, \tag{6.10}$$

where Z_1, Z_2 are constructed such that $N_p, D_p \in \mathcal{RH}_\infty$.

Remark

The parameterization in (6.10) is chosen such that Requirement 1 is facilitated, other options are possible if improved performance is the sole requirement. However, other filter selections than (6.10) will not achieve ((d)) in Theorem 6.4, which follows below.

For (6.10) to be a valid coprime factorization as defined in Definition 6.2, it is required that both P_1, P_2 have no pole/zero cancellations and Z_1, Z_2, which are constructed by the user, should be selected such that they contain no additional RHP zeros other than those required to ensure $D_p \in \mathcal{RH}_\infty$. This is a direct requirement of coprime factorization, since it does not allow for RHP pole/zero cancellation between N_p and D_p^{-1}.

The resulting coupled closed-loop system $\mathcal{F}_l(P_0, K_{\Delta_k})$ can be written as the sum of the original closed-loop system $\mathcal{F}_l(P_0, K_0)$, which is assumed to be stable, and an additional factor that is affine in $\Delta_k \in \mathcal{RH}_\infty$. The design parameters of the add-on coupling controllers are contained in the Youla parameter Δ_k, i.e., define Δ_k as

$$\Delta_k = \begin{bmatrix} 0 & \hat{X} \\ \hat{Y} & 0 \end{bmatrix} \in \mathcal{RH}_\infty. \tag{6.11}$$

The structure in (6.11) indicates the structure of the additional coupling between the subsystems. An off-diagonal matrix indicates that there exist only coupling between the subsystems and no coupling within the subsystems, i.e., the decentralized controller is fixed in view of Assumption 6.1.
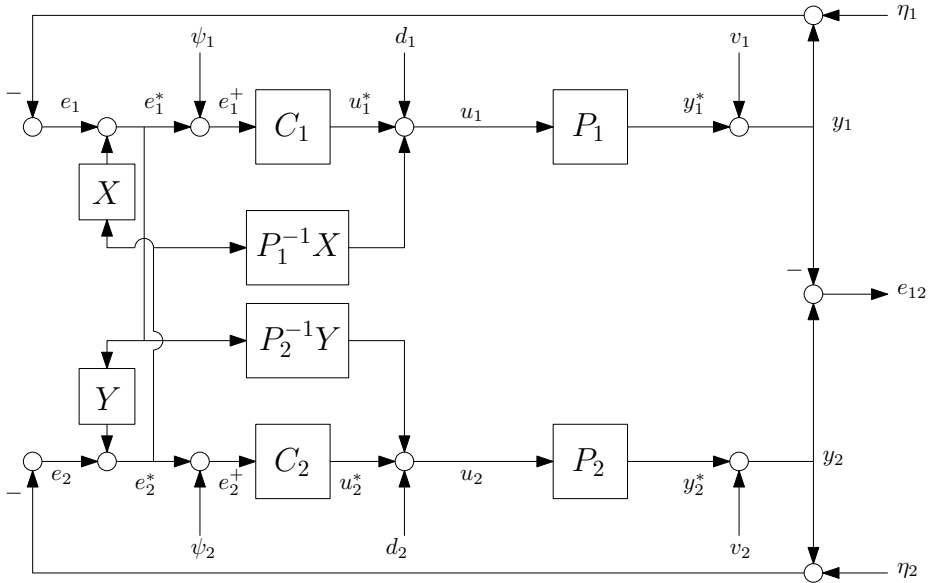
Figure 6.6. Proposed controller structure represented in a conventional control block diagram.

Substituting (6.11) into (6.7) reveals that the set of stabilizing controllers is given by

$$K_{\Delta_k} = \begin{bmatrix} C_1 & P_1^{-1} Z_1 \hat{X} \\ P_2^{-1} Z_2 \hat{Y} & C_2 \end{bmatrix} \begin{bmatrix} I & -Z_1 \hat{X} \\ -Z_2 \hat{Y} & I \end{bmatrix}^{-1}. \tag{6.12}$$

Note that $\hat{X}, \hat{Y} \in \mathcal{RH}_\infty$ are the free design parameters, since Z_1, Z_2 must be chosen such that $D_p \in \mathcal{RH}_\infty$.

> **Remark**
>
> Note that $K_0 \in \mathcal{RH}_\infty$ and $\Delta_k \in \mathcal{RH}_\infty$ does not immediately imply that $K_{\Delta_k} \in \mathcal{RH}_\infty$. Through a small gain argument, it is sufficient that $||Z_1 \hat{X} Z_2 \hat{Y}||_\infty < 1$ to guarantee that $K_{\Delta_k} \in \mathcal{RH}_\infty$ which is often desired for industrial implementation.

6.3.3. Synchronization framework

By combining the Youla framework in Section 6.3.1 with the specific choices in Section 6.3.2, the main result of this section, which constitutes Contribution 6.1, can be stated. The proposed Youla parameterization corresponds to the structure shown in Figure 6.6 with $X = Z_1 \hat{X}$ and $Y = Z_2 \hat{Y}$.

By using a specific structure in the coprime factorization of P_0 in (6.10) the following theorem provides the basis for the design framework, i.e., Contribution 6.1.

Theorem 6.4 (Bi-directional coupling). *Given the feedback loop with K_0 and system P_0 are defined by (6.9) and (6.10), respectively, and Δ_k is chosen as in (6.11), then the set of stabilizing bi-directional coupling controllers for P_0 is given by:*

$$K_{\Delta_k}(P_0) = \{N_{k_\Delta} D_{k_\Delta}^{-1} | \Delta_k \in \mathcal{RH}_\infty\} \tag{6.13}$$

Any controller in (6.13) then achieves the coupled closed-loop $\mathcal{F}_l(P_0, K_{\Delta_k})$ that has the following properties.

(a) $\forall \Delta_k \in \mathcal{RH}_\infty$, $\mathcal{F}_l(P_0, K_{\Delta_k})$ *is well-posed and internally stable.*
(b) $\forall \Delta_k$, $\mathcal{F}_l(P_0, K_{\Delta_k})$ *is affine in Δ_k.*
(c) $\forall \Delta_k$, $\mathcal{F}_l(P_0, K_{\Delta_k})_{ii} = \mathcal{F}_l(P_0, K_0)_{ii}$, *where $i = [1,2]$ of each 2×2 block matrix entry.*
(d) $\forall \Delta_k$, $e_1^+ \neq f(e_2^+)$ *and* $e_2^+ \neq f(e_1^+)$, *i.e. e_1^+, e_2^+ are invariant to the added coupling.*

See 6.A for a proof.

The results illustrated in Theorem 6.4 enables the fulfillment of the requirements posed in Section 6.2.2. In particular result (a) together with result (b) allows for relatively straightforward tuning of the coupling elements Δ_k and simplifies the nominal stability proof, therefore fulfilling Requirement 1. Results (c) and (d) are closely related and reveal that for all Δ_k the coupled closed-loop system maintains the original decentralized controllers. Moreover, the input to the original controllers is solely a function of their respective decentralized loop, i.e., no inter-subsystem coupling is observed and thus Requirement 2 is fulfilled. This leaves Requirement 3, robust stability, which is addressed in Section 6.5.

By evaluating the full closed-loop transfer function matrix of the coupled system (6.41) in 6.A a relation for $e_{12} = y_2 - y_1$ can be found. The combined system performance, reduced to a function of two output disturbances v_1, v_2 to facilitate the presentation, is given by

$$e_{12} = -(I + Y)S_1 v_1 + (I + X)S_2 v_2, \tag{6.14}$$

where $Y = Z_2\hat{Y}, X = Z_1\hat{X}$. The structure relates to the result shown in (6.4). It shows that the coupled system can be described by the original decentralized transfer function matrices and two affine improvement factors $(I + Y), (I + X)$. This is a key result and enables Contribution 6.1 that is presented in Section 6.4. Therefore, overall superior system performance can be achieved by optimizing the improvement factors under the constraints presented in the Youla framework.

The presented framework is a generalization of previous master-slave type solutions. An unidirectional coupling is most commonly seen in short-stroke long-stroke master-slave control systems, e.g., in precision actuator design. By setting $Y = 0$, a unidirectional coupling approach as presented, e.g., in Heertjes and Temizer (2012) is recovered as a special case of the presented framework.

6.4. Design guidelines

In this section, a design procedure to facilitate the design of the add-on controller elements under the constraints of the Youla framework is presented, thereby constituting Contribution 6.1. Perfect disturbance attenuation in (6.14) is achieved when $X = Y = -I$, i.e., $(I + X) = 0$ and $(I + Y) = 0$. However, this generally leads to an inadmissible coprime factorization in (6.10), e.g. $D_p \notin \mathcal{RH}_\infty$ caused by non-invertible elements in the nominal plant models of the subsystems. This can be caused by NMP zeros, I/O delay and pole/zero excess, leading to complications with model inversion (Blanken et al., 2018).

In the proposed framework the parameters X, Y are constructed out of two components, i.e., $X := Z_1\hat{X}, Y := Z_2\hat{Y}$. Components denoted as Z_1, Z_2 that, in view of requirements, must be chosen such that $\{P_1^{-1}X, P_2^{-1}Y\} \in \mathcal{RH}_\infty$ and components $\hat{X}, \hat{Y}$ that can be designed to minimize e_{12}, where e.g., for the SISO case $|(I + Z_1\hat{X})| < 1$ and $|(I + Z_2\hat{Y})| < 1$, for specific, e.g., low, frequency ranges. A similar approach for tracking control can be found in Tomizuka (1987).

The following procedure aims to design X, Y such that e_{12} is minimized under the constraints posed by the Youla framework.

Algorithm 2 Bi-directional coupling filters

1: Construct the models P_1, P_2.
2: If $P_1^{-1}, P_2^{-1} \notin \mathcal{RH}_\infty$, construct Z_1, Z_2 such that

$$P_1^{-1}Z_1, P_2^{-1}Z_2 \in \mathcal{RH}_\infty. \tag{6.15}$$

3: Evaluate
$$|(I + Z_1\hat{X})|, |(I + Z_2\hat{Y})| \ \forall \ \omega \tag{6.16}$$

and construct $\hat{X}, \hat{Y}$ such that (6.16) is small for specific, e.g., low-frequency ranges.
4: Implement the stabilizing coupling controller by constructing (6.13) as described in Theorem 6.4.

Remark

In this section P_1 is used as an example, the design guidelines for P_2 are conceptually similar.

Step 1 Constructing the models for P_1 and P_2 can be done by first principle modeling or parametric model identification procedures. Dealing with a mismatch between the true system and the nominal system models is addressed in Section 6.5.

Step 2   The NMP zeros of P_1 in (6.10) are contained in Z_1 such that they cancel in $P_1^{-1}Z_1$. However, this generally makes $Z_1\hat{X} \notin \mathcal{RH}_\infty$ since duplicating the zeros leads to a non-proper filter. Therefore, the NMP elements in Z_1 are constructed as biproper all-pass elements, i.e., their relative degree is 0 and $|Z_1(j\omega)| = 1 \ \forall \ \omega$, to ensure that the parameter $Z_1\hat{X} \in \mathcal{RH}_\infty$ as required by (6.10). To enforce a proper filter $P^{-1}Z_1$, the element Z_1 includes a low-pass filter with a high-frequency cut-off of order equal to or greater than the amount of pole/zero excess.

Step 3   Using the free design parameter $\hat{X}$, the improvement factor $(I + Z_1\hat{X})$ can be shaped such that the coupled closed-loop disturbance attenuation is improvement at the desired, e.g. low, frequency region. The parameter can be shaped using manual loop-shaping or norm optimal techniques such as $\mathcal{H}_2/\mathcal{H}_\infty-$optimal controller design. If the free design parameter is chosen as $\hat{X} = -I$ it is ensured that $|(I + X)| \ll 1$ at low frequencies which is generally desired for disturbance attenuation.

Step 4   By following the systematic design procedure the results in Theorem 6.4 hold, and the stabilizing coupling filter is given by the form in (6.13).

The guidelines presented in this section facilitate a straightforward manual design of the coupling filters. By following the design rules it is guaranteed that the full system performance is improved, under the assumption that $|(I + Z_1\hat{X})| < 1$ and/or $|(I + Z_2\hat{Y})| < 1$ for some frequency range of interest, while maintaining nominal stability.

Example 6.5. *Consider the following continuous time subsystem model*

$$P_1 = \frac{s - a}{s + b},$$

with $a, b \in \mathbb{R} > 0$. The subsystem has a RHP zero and inversion under the constraint in (6.10) not possible. Therefore, Z_1 is constructed as

$$Z_1 = \frac{s - a}{s + a} \in \mathcal{RH}_\infty.$$

It then follows that

$$P_1^{-1}Z_1 = \frac{s + b}{s + a} \in \mathcal{RH}_\infty,$$

can be used in an admissible RCF in the Youla framework to approximate P_1^{-1}. The improvement factor now becomes

$$(I + Z_1) = I + \frac{s - a}{s + a} \tag{6.17}$$

of which the amplitude ranges from $|(I + Z_1)| \in [0, 2]$ when $s = j\omega \in [0, \inf]$ due to the phase shift in Z_1.
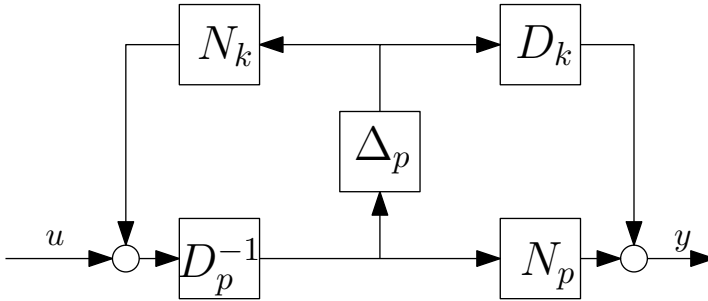
Figure 6.7. Dual Youla factorization for a set of stabilized plants $P_{\Delta_p}(K_0)$. Here each of the elements is composed of a 2×2 diagonal transfer function matrix.

6.5. Modeling uncertainty: dual-Youla

This section presents an extension to the Youla framework presented in Section 6.3 that appropriately addresses robust stability. This is done by extending the Youla framework with a dual-Youla parameterization that facilitates the inclusion of model uncertainties. By extending the framework, robust stability can be guaranteed, constituting Contribution 6.1.

6.5.1. Dual-Youla

To analyze the effect of model uncertainty on system stability, use is made of a dual-Youla parameterization (Niemann, 2003) as shown in Figure 6.7. The parameterization is not unique, but the chosen structure is dual to the framework used to represent nominal bi-directional coupling as presented in Section 6.3.

Using coprime factorization, it is possible to define a set of plants $P_{\Delta_p}(K_0)$ that are stabilized by a nominal controller K_0.

Theorem 6.6 (Set of stabilized systems)**.** *Let P_0 and K_0 have RCFs $P_0 = N_p D_p^{-1}$ and $K_0 = N_k D_k^{-1}$, then the perturbed factors are defined as:*

$$N_{\Delta_p} := N_p + D_k \Delta_p, \quad D_{\Delta_p} := D_p - N_k \Delta_p \tag{6.18}$$

such that the set of systems that are stabilized by K_0 is equal to

$$P_{\Delta_p}(K_0) = \{N_{\Delta_p} D_{\Delta_p}^{-1} | \Delta_p \in \mathcal{RH}_\infty\}, \tag{6.19}$$

where set $P_{\Delta_p}(K_0)$ represents all possible systems that are stabilized by the nominal controller K_0 under a model uncertainty Δ_p.

See, e.g., Ma (1988) for a proof.

By using the same coprime factorization for P_0 and K_0 as used in Section 6.3 the nominal framework is extended to include model uncertainty. In contrast to Δ_k, which is structured to contain only off-diagonal elements, the plant uncertainty model can be unstructured such that

$$\Delta_p := \begin{bmatrix} \Delta_{p_{11}} & \Delta_{p_{12}} \\ \Delta_{p_{21}} & \Delta_{p_{22}} \end{bmatrix} \in \mathcal{RH}_\infty \qquad (6.20)$$

where $\Delta_{p_{11}}, \Delta_{p_{22}}$ indicate nominal subsystem model uncertainty and $\Delta_{p_{12}}, \Delta_{p_{21}}$ indicate (possibly small) inter-subsystem coupling effects.

To construct the subsystem uncertainty model, use is made of a parametric nominal system model and non-parametric system identification measurements (Evers et al., 2018a) to significantly reduce modeling effort. By adopting a similar approach as in Oomen et al. (2014b); Van de Wal et al. (2002), where given a measured Frequency Response Function (FRF) P_{frf}, the uncertainty block Δ_k that achieves $P_{frf} = P_{\Delta_k}(K_0)$ is given by:

$$\Delta_k = (D_k + P_{frf} N_k)^{-1} (P_{frf} - P_0) D_p. \qquad (6.21)$$

This provides a straightforward approach to construct the uncertainty model Δ_k using an inexpensive non-parametric estimate of the (MIMO) frequency response function.

Remark

Note that $\Delta_k \in \mathcal{RH}_\infty$ as described in Section 6.3 is fully known. The plant uncertainty model $\Delta_p \in \mathcal{RH}_\infty$, however, is sometimes unknown and can be bounded in $\mathcal{H}_\infty$ norm using uncertainty modeling techniques (Oomen et al., 2014a) using closed-loop measurements.

6.5.2. Double-Youla: robust stability

Using the dual-Youla parameterization in Theorem 6.6 it is guaranteed that $\forall\, \Delta_p \in \mathcal{RH}_\infty$ the system is stabilized by the nominal controller K_0. Furthermore, by Theorem 6.3 any K_{Δ_k} induced by $\Delta_k \in \mathcal{RH}_\infty$ stabilizes the nominal plant P_0. In view of Contribution 6.1, the main interest is whether K_{Δ_k} stabilizes all P_{Δ_p} in the closed-loop system $\mathcal{F}_l(P_{\Delta_p}, K_{\Delta_k})$.

By using the result from Theorem 6.6 the stability proof of the Youla framework can be extended to include the uncertainty model Δ_p such that the following holds

Theorem 6.7 (Robust bi-directional coupling)**.** *Consider a closed-loop system* $\mathcal{F}_l(P_{\Delta_p}, K_{\Delta_k})$ *as shown in Figure 6.8, with simultaneous controller* Δ_k *and plant* Δ_p *perturbations chosen as (6.11) and (6.20), respectively. It can be assumed*
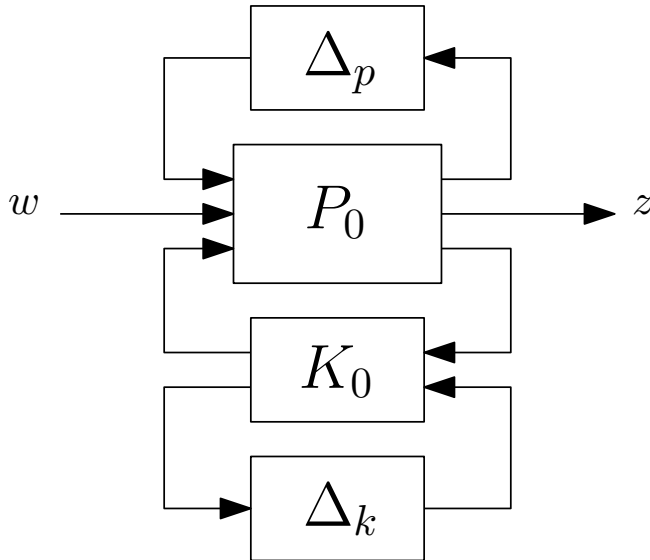
Figure 6.8. Standard plant notation of robust bi-directional coupling. The nominal plant and controller are subject to simultaneous perturbations Δ_k and Δ_p respectively.

that $\mathcal{F}_l(P_0, K_0)$ is stable. If the interconnection of Δ_k and Δ_p is stable, then the closed-loop system $\mathcal{F}_l(P_{\Delta_p}, K_{\Delta_k})$ is stable.

See, e.g, Schrama et al. (1992); Tay et al. (1998) for a proof. The Youla parameterization for K_{Δ_k} connected with the dual-Youla parameterization for P_{Δ_p} forms the double-Youla parameterization that allows for the full analysis and synthesis of the robust add-on coupling filters.

In the presented framework, the elements Z_1 and Z_2 are fixed by the design guidelines presented Section 6.4. The elements $\hat{X}, \hat{Y}$ are free design parameters and can be tuned such to achieve performance requirements. These elements $\hat{X}, \hat{Y}$ must be constructed such that the full system $\mathcal{F}_l(P_{\Delta_p}, K_{\Delta_k})$ remains stable. This can be done by two different approaches, manual design and norm-based optimal design

Manual design for RS: Manual loopshaping remains common practice in industry (Oomen, 2018), which motivated the add-on requirement in Section 6.2.2. And multivariable systems are often decomposed into scalar systems by applying techniques such as sequential loop closing (Maciejowski, 1989, Sec 4.2). Therefore, a suitable stability criterion is required to apply these manual methods to the robust coupling filter design. For this, a stability criterion based on the small gain argument is constructed. Since the coupling filters Δ_k have a clear off-

diagonal structure, the structured singular value (Skogestad and Postlethwaite, 2009, Sec 8.8) is used to reduce its conservatism.

Theorem 6.8. *The closed-loop $\mathcal{F}_l(P_{\Delta_p}, K_{\Delta_k})$ is stable if*

$$\bar{\sigma}(\Delta_k(j\omega)) < \mu_{\Delta_k}(\Delta_p(j\omega))^{-1} \quad \forall\ \omega \tag{6.22}$$

where $\bar{\sigma}$ denotes the maximum singular value at a single frequency and $\mu_{\Delta_k}(\Delta_p(j\omega))$ denotes the structured singular value of Δ_p with respect to the structure in Δ_k.

Proof. By small-gain argument, Δ_k stabilizes Δ_p if $||\Delta_k\Delta_p||_\infty \leq ||\Delta_k||_\infty ||\Delta_p||_\infty < 1$. Since $\{\Delta_k, \Delta_p\} \in \mathcal{RH}_\infty$ it holds that $||\Delta_k||_\infty ||\Delta_p||_\infty < 1 \Leftrightarrow \bar{\sigma}(\Delta_k(j\omega))\bar{\sigma}(\Delta_p(j\omega)) < 1\ \forall\ \omega$. And since $\mu_{\Delta_k}(\Delta_p) \leq \bar{\sigma}(\Delta_p)$, Δ_k stabilizes Δ_p if $\bar{\sigma}(\Delta_k(j\omega)) < \mu_{\Delta_k}(\Delta_p)^{-1}\ \forall\ \omega$. Therefore the closed-loop system $\mathcal{F}_l(P_{\Delta_p}, K_{\Delta_k})$ is stable by Theorem 6.7.   □

Since it holds that $\mu_{\Delta_k}(\Delta_p) \leq \bar{\sigma}(\Delta_p)$ the criterion in (6.22) is less conservative than using the regular singular value $\bar{\sigma}$. If no uncertainty is present, i.e., $\Delta_p = 0$, then any $\Delta_k \in \mathcal{RH}_\infty$ is admissible and Theorem 6.3 is recovered as a special case. A dual result holds for the plant uncertainty Δ_p. The result shows that if (6.22) holds, then the simultaneous perturbation $\{\Delta_p, \Delta_k\}$ does not induce unstable system behavior. Given that Δ_k is structured as an off-diagonal matrix, and therefore the maximum singular value is determined by the off-diagonal elements, and for robust stability it is required that (6.22) holds,

$$\{\bar{\sigma}(\hat{X}(j\omega)), \bar{\sigma}(\hat{Y}(j\omega))\} < \mu_{\Delta_k}(\Delta_p(j\omega))^{-1}\ \forall\ \omega \tag{6.23}$$

is sufficient to achieve robust stability. These bounds can be enforced in arbitrary order, allowing for use of well known manual methods such as sequential loopshaping for the design of the coupling elements $\hat{X}$ and $\hat{Y}$ in Δ_k.

$\mathcal{H}_\infty$-design for RS: An alternative to manual loopshaping design of the coupling filters can be norm-optimal techniques such as $\mathcal{H}_\infty$-design. A one-shot procedure to synthesize Δ_k based weighting filters and Thm. 6.7 is possible, but complicated due to the structure in Δ_k, e.g., forcing diagonal elements to be zero. This would require techniques such as structured $\mathcal{H}_\infty$ design, see, e.g., Burke et al. (2006). To reduce the computational complexity a different, more traditional $\mathcal{H}_\infty$ approach is taken by applying the sequential stability bounds (6.23) directly as an $\mathcal{H}_\infty$ weighting filter.

The improvement factor $(I + Z_1\hat{X})$, in (6.14), is represented as a block diagram in Figure 6.9. If the parameter $\hat{X}$ is then considered the controller to a plant Z_1 the problem can be rewritten as a standard disturbance attenuation problem in the standard plant shown in Figure 6.9 on the right. If $\hat{X}$ and
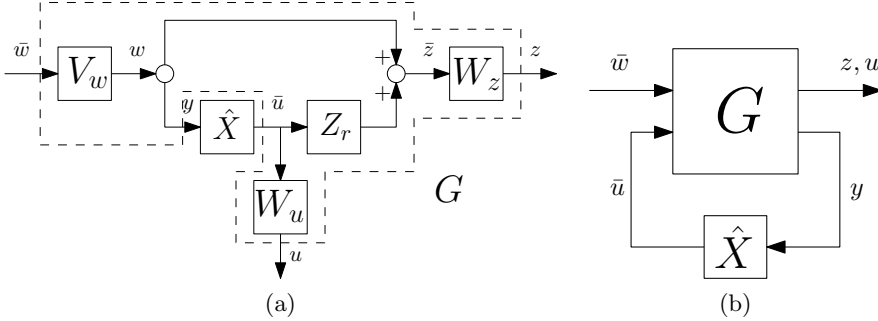
Figure 6.9. Block diagram representing the improvement factor, as conventional (a) and standard plant (b).

$\hat{Y}$ are bounded by $\mu_{\Delta_k}(\Delta_p(j\omega))^{-1}$ the bi-directional closed-loop system is robustly stable. Since $\{\hat{X}, \hat{Y}\} \in \mathcal{RH}_\infty$ it holds that $||\hat{X}||_\infty = \max_\omega \bar{\sigma}(\hat{X}(j\omega))$ and $||\hat{Y}||_\infty = \max_\omega \bar{\sigma}(\hat{Y}(j\omega))$. Assuming W_u is a weighting function (Van de Wal et al., 2001) on $\hat{X}$ then this yields

$$||\hat{X}(j\omega)W_u(j\omega)||_\infty < 1 \tag{6.24}$$

$$||\hat{X}(j\omega)||_\infty < ||W_u(j\omega)^{-1}||_\infty \tag{6.25}$$

and if $W_u(j\omega) = \mu_{\Delta_k}(\Delta_p(j\omega))$ this achieves

$$\max_\omega \bar{\sigma}(\hat{X}(j\omega)) < \max_\omega \bar{\sigma}(\mu_{\Delta_k}(\Delta_p(j\omega))^{-1}) \tag{6.26}$$

and since for a scalar element $\bar{\sigma}(\mu_{\Delta_k}(\Delta_p(j\omega))^{-1}) = \mu_{\Delta_k}(\Delta_p(j\omega))^{-1}$ it fulfills the constraint (6.23). A similar derivation holds for $\hat{Y}$. Moreover, the output weighting filter W_z is constructed such to achieve the desired performance specification, e.g. $(I + Z_1\hat{X})$ small for low frequencies. The input filter V_w is taken as identity. Using this approach it is possible to automatically synthesize the coupling filters $\hat{X}, \hat{Y}$ to achieve a low-frequency performance improvement while maintaining full system robust stability.

The Double-Youla framework lends itself well to conventional and norm optimal controller synthesis techniques. It allows for the application of the stability criterion separately to each of the coupling filters. And facilitates the controller design engineer to use the preferred tool, e.g., manual loopshaping or norm-based synthesis. This is a useful step towards industrial adaptation, especially since the interconnected multivariable approach is becoming increasingly important in the manufacturing industry while SiSo methods remain the standard (Oomen, 2018).
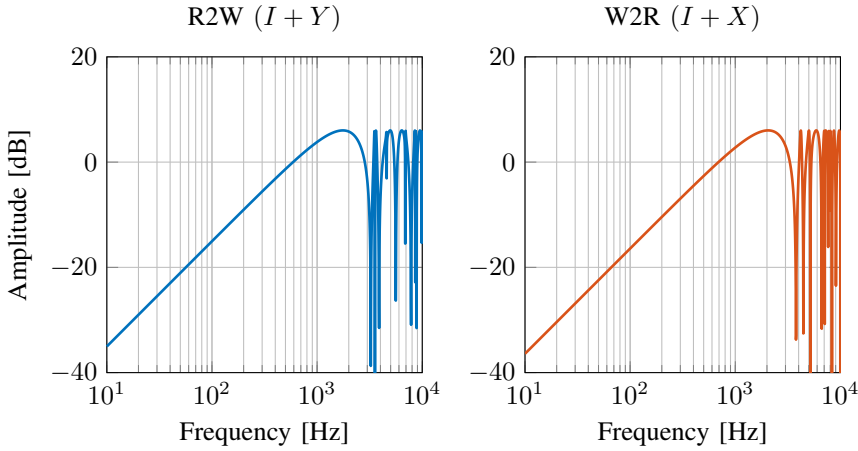
Figure 6.10. The improvement factors for R2W (——) and W2R (——) coupling. It shows that for low frequencies a significant improvement in disturbance attenuation can be achieved.

6.6. Application to a Wafer Scanner

The following section applies the developed theoretical framework to the case study presented in Section 6.2.1 using real system measurements and a high-fidelity simulator of an industrial wafer scanner. It illustrates the potential of the framework and constitutes Contribution 6.1.

6.6.1. Youla framework

To suppress the output disturbance shown in (6.14) it is desired that the improvement factors are smaller than 1 for low-frequencies up till approximately 200 [Hz].

Applying the nominal design procedure as described in Proc. 2 in Section 6.4 yields results shown in Figure 6.11. It shows the change in the sensitivity function of the disturbance towards the overall performance criterion e_{12}. This change is affine in the improvement factors, shown in Figure 6.10, e.g., $(I+Y)S_r$ and $(I+X)S_w$ are the new reticle stage and wafer stage sensitivity functions, respectively. Importantly, the dips in the sensitivity functions at higher frequencies are not caused by increased controller gain but rather the improvement factors $(I+X)$ and $(I+Y)$ being locally equal to 0. By applying the additional coupling elements the low-frequency disturbance attenuation is greatly improved.

The time domain performance is investigated by utilizing 8 measured servo error traces of wafer scan movement. The expected performance using bi-
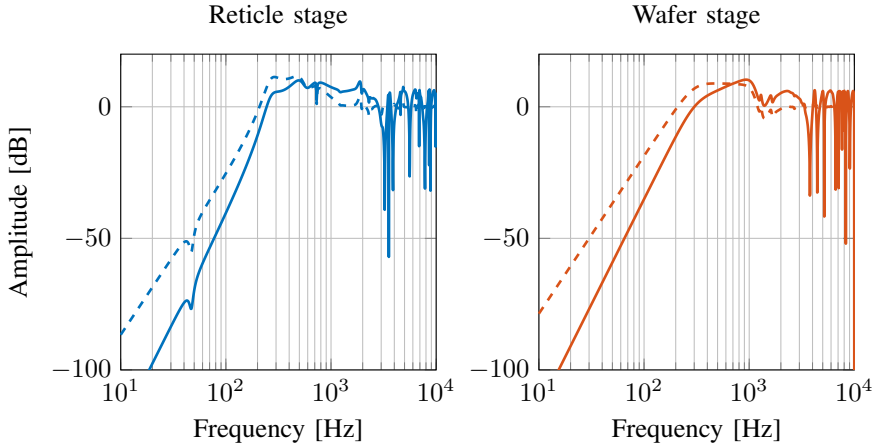
Figure 6.11. Original sensitivity for the reticle S_r (- - -) stage and wafer S_w (- - -) stage. Improved reticle sensitivity (——) and wafer sensitivity (——) by applying coupling filter shown in Figure 6.10.

directional coupling is then simulated using the high-fidelity system models in the simulator. The results in Figure 6.12 show that at low-frequencies the additional controller freedom is exploited to synchronize the stages. The results in Figure 6.13 then show that the improved synchronization of the two stages yields a significant improvement in the performance variable e_{12} at low-frequencies.

6.6.2. Dual Youla

The results of the nominal coupling illustrate the potential performance gain by the additional controller freedom. Robust stability under model uncertainty is achieved using the dual Youla result in Section 6.5. Theorem 6.3 shows that $\Delta_k \in \mathcal{RH}_\infty$ is sufficient to ensure closed-loop nominal stability. However, this only holds when $\Delta_p = 0$ as shown in Lemma (6.8). Therefore, to ensure robust stability an uncertainty model is constructed using the nominal plant P_0 and a set of measurements. The uncertainty element is constructed as

$$\Delta_p = \begin{bmatrix} \Delta_{p_{11}} & 0 \\ 0 & \Delta_{p_{22}} \end{bmatrix} \tag{6.27}$$

where $\Delta_{p_{11}}$ and $\Delta_{p_{22}}$ are constructed by applying (6.21).

The diagonal entries of (6.27) are shown in Figure 6.14, it indicates that at low-frequencies the uncertainty is small since the system dynamics are accurately modeled by a rigid body approximation. At higher frequencies the nominal system model contains a relatively large amount of uncertainty. This increase in model uncertainty limits the amount of coupling admissible by (6.8).
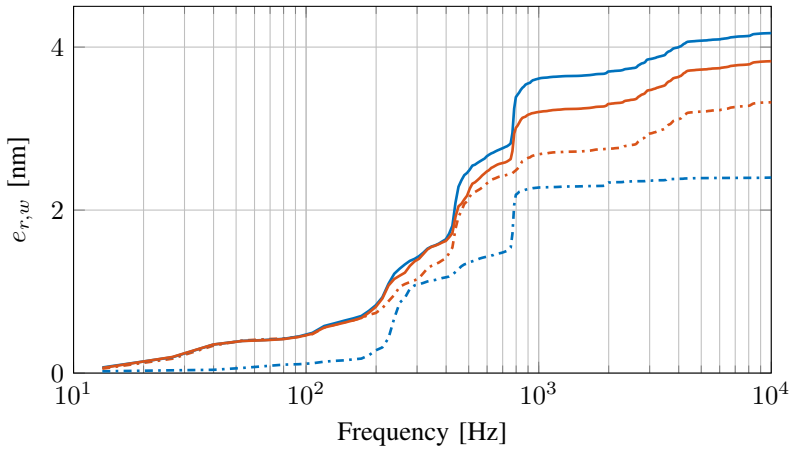
Figure 6.12. Cumulative subsystem servo error, mean + 3σ, of the reticle stage (——) and wafer stage (——) with coupling. And the reticle stage (–·–·) and wafer stage (–·–·) without coupling. To achieve stage synchronization the reticle stage is synchronized to the wafer stage.
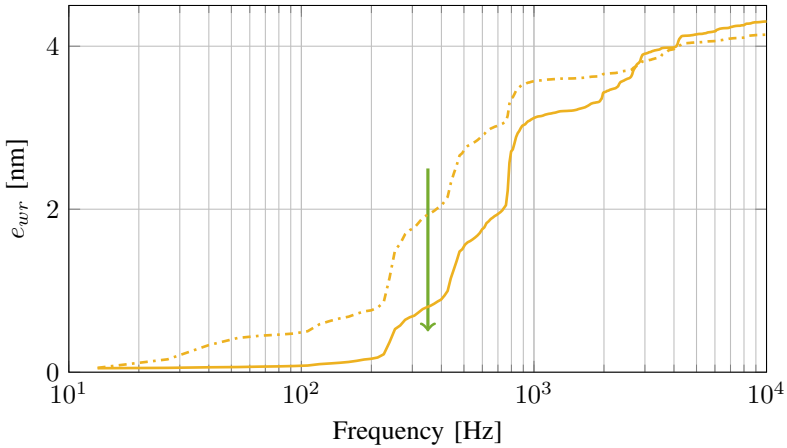
Figure 6.13. Cumulative relative servo error with (——) and without (–·–·) coupling. Results show a clear reduction in low-frequency content at the cost of slight high-frequent deterioration.
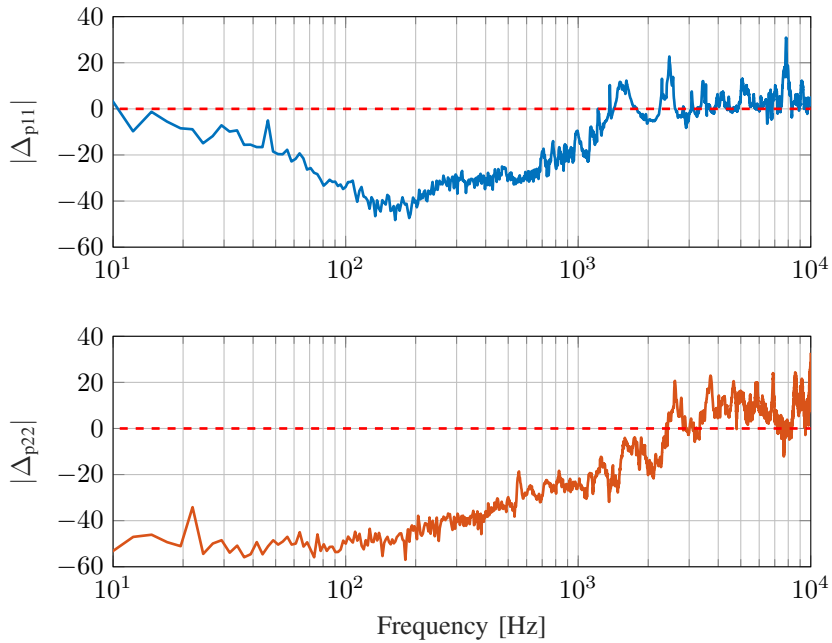
Figure 6.14. Maximum uncertainty models for the reticle stage (——) and wafer stage (——). Constructed by taking the maximum amplitude over frequency at spatially distributed measurement locations.

Moreover, the results in Figure 6.16 show that the system is not guaranteed to be stable as (6.22) is not fulfilled. To achieve robust stability, $\mathcal{H}_\infty$-synthesis, following Section 6.5.2, robust coupling filters are synthesized. The new Youla
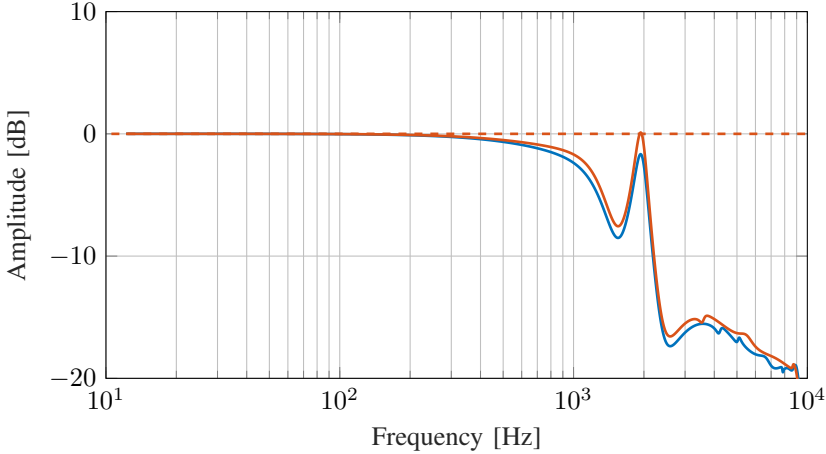
Figure 6.15. Robust Youla parameters $\hat{X}$ (——), $\hat{Y}$(——) compared to the nominal Youla parameters, that are both equal to 0 [dB] (- - -). Phase information is omitted as only the amplitude is used in the small gain analysis.

parameters are shown in Figure 6.15. Robust stability is achieved by including high-frequency roll-off, thus limiting the coupling in regions with high model uncertainty as shown in Figure 6.14. The results in Figure 6.16 show that using the new coupling elements, under Thm. 6.8 the system is now robustly stable.

6.6.3. Results

Figure 6.17 compares the closed-loop disturbance rejection using either the nominal or robust coupling filters. It shows that a slight low-frequency performance deterioration is required to enable sufficient robustness against the large model uncertainty at high-frequencies.

The results in Tab. 6.1 present the averaged time-domain scanning results at 5 distributed locations on the wafer and 3σ indicates the 99.73% confidence interval. It shows that a decrease in Moving Average (MA), which is correlated to overlay and the more critical performance indicator, causes an increased Moving Standard Deviation (MSD), which is correlated to image focus (Butler, 2011). And that by adding robustness to the nominal coupling filters some performance is lost. However, both the nominal and robust coupling achieve a significant reduction in MA and therefore yield superior overlay performance.
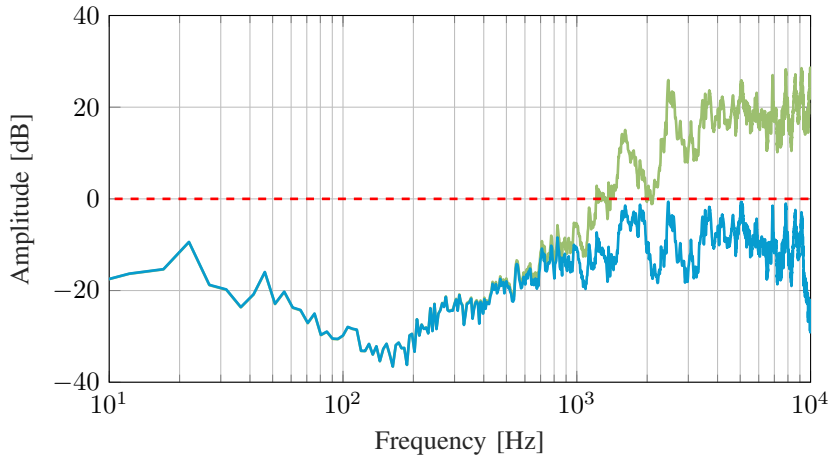
Figure 6.16. Small gain criterion using the nominal (——) and newly designed robust (——) Youla parameters. By de-tuning the coupling Δ_k at high frequencies, the small gain criterion using the structured singular value is now fulfilled under the model uncertainty.

Table 6.1. MA and MSD results using nominal or robust coupling filters.

	No coupling	Nominal	Robust
MA [pm]			
3σ	565	108	200
Peak	603	182	338
MSD [pm]			
3σ	2879	3329	3304
Peak	3145	3485	3670

6.7. Conclusion

The framework presented in this chapter enables coupling of subsystems to improve overall system performance. The framework is well-suited for a large range of mechatronic systems, where subsystems are often designed, built, and controlled separately. The proposed framework enables a systematic performance improvement of the integrated system.

A nominal design approach is given where the coupled system behavior is expressed as a straightforward combination of the original closed-loop characteristics and an affine factor, allowing for simplified design. Model uncertainty is appropriately addressed and a sufficient condition for robust stability is provided that can be used in a posteriori analysis or a priori constraint based $\mathcal{H}_\infty$-synthesis
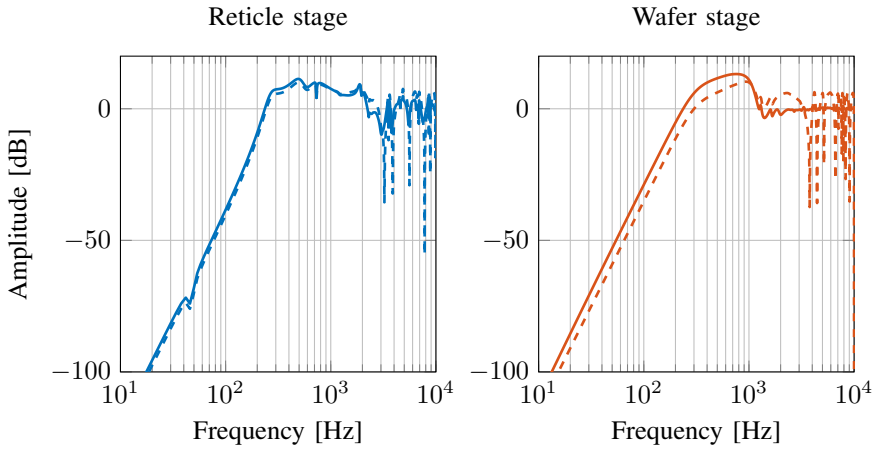
Figure 6.17. Bode magnitude diagram comparing the sensitivity using nominal coupling, for the reticle stage (- - -) and wafer stage (- - -), and robust coupling, for the reticle stage (——) and wafer stage (——).

of the add-on coupling elements. This in contrast to the industry standard of manual tuning that requires significant trial and error by an experienced control engineer. This substantially simplifies the process of coupling an increasing amount of subsystems contained in modern systems-of-systems used in the manufacturing industry. The resulting design framework facilitates improved overall system performance and achieves robust stability. In addition, there is current research effort aiming to employ the developed framework for the coupling of thermal-mechanical systems (Evers et al., 2018a), for real-time thermal induced deformation compensation.

6.A. Proof of Theorem 6.4

Proof. Following (Schrama et al., 1992), the set of stabilizing controllers is defined using the perturbed controller factors:

$$N_{k_\Delta} := N_k + D\Delta_k, \quad D_{k_\Delta} := D_k - N\Delta_k \tag{6.28}$$

These factors, under the controller and plant definition given in Thm. 6.4, are equal to

$$N_{k_\Delta} = \begin{bmatrix} C_1 & 0 \\ 0 & C_2 \end{bmatrix} + \begin{bmatrix} P_1^{-1}Z_1 & 0 \\ 0 & P_2^{-1}Z_2 \end{bmatrix} \Delta_k, \tag{6.29}$$

$$D_{k_\Delta} = \begin{bmatrix} I & 0 \\ 0 & I \end{bmatrix} - \begin{bmatrix} Z_1 & 0 \\ 0 & Z_2 \end{bmatrix} \Delta_k. \tag{6.30}$$

If it is then defined that Δ_k equals

$$\Delta_k = \begin{bmatrix} 0 & \hat{X} \\ \hat{Y} & 0 \end{bmatrix} \tag{6.31}$$

the perturbed controller factors become

$$N_{k_\Delta} = \begin{bmatrix} C_1 & P_1^{-1}Z_1\hat{X} \\ P_2^{-1}Z_2\hat{Y} & C_2 \end{bmatrix}, D_{k_\Delta} = \begin{bmatrix} I & -Z_1\hat{X} \\ -Z_2\hat{Y} & I \end{bmatrix} \tag{6.32}$$

thus yielding

$$K_{\Delta_k}(P_0) = \begin{bmatrix} C_1 & P_1^{-1}X \\ P_2^{-1}Y & C_2 \end{bmatrix} \begin{bmatrix} I & -X \\ -Y & I \end{bmatrix}^{-1} \tag{6.33}$$

where $X = Z_1\hat{X}$ and $Y = Z_2\hat{Y}$. The closed-loop equations are derived by using that $y = (I + P_0K_{\Delta_k}(P_0))^{-1}\tilde{e}$, which brings the full closed loop to

$$\begin{bmatrix} y_1 \\ y_2 \end{bmatrix} = \underbrace{\left(\begin{bmatrix} I & 0 \\ 0 & I \end{bmatrix} + \begin{bmatrix} P_1C_1 & P_1P_1^{-1}X \\ P_2P_2^{-1}Y & P_2C_2 \end{bmatrix} \underbrace{\begin{bmatrix} I & -X \\ -Y & I \end{bmatrix}^{-1}}_{H^{-1}} \right)^{-1}}_{M^{-1}} \tilde{e} \tag{6.34}$$

where

$$\tilde{e} = \left(\begin{bmatrix} v_1 + P_1d_1 + P_1C_1\psi_1 \\ v_2 + P_2d_2 + P_2C_2\psi_2 \end{bmatrix} \right.$$

$$\left. - \begin{bmatrix} P_1C_1 & P_1P_1^{-1}X \\ P_2P_2^{-1}Y & P_2C_2 \end{bmatrix} \begin{bmatrix} I & -X \\ -Y & I \end{bmatrix}^{-1} \begin{bmatrix} \eta_1 \\ \eta_2 \end{bmatrix} \right) \tag{6.35}$$

Here, H^{-1} is written, using block matrix inverse (Lu and Shiou, 2002), as

$$H^{-1} = \begin{bmatrix} \alpha & X\beta \\ Y\alpha & \beta \end{bmatrix} \qquad (6.36)$$

where $\alpha = (I - XY)^{-1}$ and $\beta = (I - YX)^{-1}$, yielding

$$M = \begin{bmatrix} I + (XY + P_1C_1)\alpha & (P_1C_1 + I)X\beta \\ (P_2C_2 + I)Y\alpha & I + (YX + P_2C_2)\beta \end{bmatrix} \qquad (6.37)$$

where entries $M(1,1)$ and $M(2,2)$ can be simplified by using $I = \alpha^{-1}\alpha$ and $I = \beta^{-1}\beta$ respectively. This brings M to

$$M = \begin{bmatrix} (I + P_1C_1)\alpha & (I + P_1C_1)X\beta \\ (I + P_2C_2)Y\alpha & (I + P_2C_2)\beta \end{bmatrix} \qquad (6.38)$$

Using the block matrix inverse together with the matrix identity $(AB)^{-1} = B^{-1}A^{-1}$, it is found that

$$M^{-1} = \begin{bmatrix} (I + P_1C_1)^{-1} & -\alpha^{-1}X\beta(I + P_2C_2)^{-1} \\ -\beta^{-1}Y\alpha(I + P_1C_1)^{-1} & (I + P_2C_2)^{-1} \end{bmatrix}. \qquad (6.39)$$

Using the push-through rule (Skogestad and Postlethwaite, 2009, p65) $(I + AB)^{-1}A = A(I + BA)^{-1}$ it is seen that $X\beta = X(I - YX)^{-1} = (I - XY)^{-1}X = \alpha X$ which brings M^{-1} to

$$M^{-1} = \begin{bmatrix} (I + P_1C_1)^{-1} & -X(I + P_2C_2)^{-1} \\ -Y(I + P_1C_1)^{-1} & (I + P_2C_2)^{-1} \end{bmatrix} \qquad (6.40)$$

The full closed-loop transfer function matrix is derived by repeating the steps for all disturbances and it is provided in (6.41).

(a) Evaluating all entries of the matrix (6.41) is sufficient (Zhou et al., 1996) to guarantee well-posedness and internal stability under the assumption that $\Delta_k \in \mathcal{RH}_\infty$.

(b) Matrix (6.41) is clearly affine in Δ_k.

(c) For each of the (2×2) block matrices in (6.41) the diagonal entries are those of the original closed-loop system.

(d) By evaluating the 5th and 6th row of (6.41) it is seen that there is no interaction since the off-diagonals are 0.

$\square$

$$
\begin{bmatrix} y_1 \\ y_2 \\ e_1 \\ e_2 \\ e_1^+ \\ e_2^+ \\ u_1 \\ u_2 \\ e_{12} \end{bmatrix} =
\left[\begin{array}{cc|cc|cc|cc}
S_1 & -XS_2 & PS_1 & -XPS_2 & T_1 & -XT_2 & -T_1 & -XS_2 \\
-YS_1 & S_2 & -YPS_1 & PS_2 & -YT_1 & T_2 & -YS_1 & -T_2 \\
\hline
-S_1 & XS_2 & -PS_1 & XPS_2 & -T_1 & XT_2 & -S_1 & XS_2 \\
YS_1 & -S_2 & YPS_1 & -PS_2 & YT_1 & -T_2 & YS_1 & -S_2 \\
\hline
-S_1 & 0 & -PS_1 & 0 & S_1 & 0 & -S_1 & 0 \\
0 & -S_2 & 0 & -PS_2 & 0 & S_2 & 0 & -S_2 \\
\hline
CS_1 & P_1^{-1}XS_2 & S_1 & -P_1^{-1}XSP_2 & CS_1 & -P_1^{-1}XT_2 & CS_1 & P_1^{-1}XS_2 \\
P_2^{-1}YS_1 & CS_2 & -P_2^{-1}YSP_1 & S_2 & -P_2^{-1}YT_1 & CS_2 & P_2^{-1}YS_1 & CS_2 \\
\hline
-(I+Y)S_1 & (I+X)S_2 & -(I+Y)PS_1 & (I-X)PS_2 & -(I+Y)T_1 & (I-X)T_2 & -YS_1+T_1 & -T_2+XS_2
\end{array}\right]
\begin{bmatrix} v_1 \\ v_2 \\ d_1 \\ d_2 \\ \psi_1 \\ \psi_2 \\ \eta_1 \\ \eta_2 \end{bmatrix}
$$

(6.41)

6

CHAPTER 7

Conclusions and Recommendations

Abstract: Next-generation mechatronic systems are a culmination of a synergistic balance between a wide range of engineering domains. Impressive progress in advanced motion control has led to a situation where the thermally induced deformations are of essential importance in the overall system performance. The main idea pursued in this thesis is geared towards taking an active approach to thermally induced deformations rather than relying on mitigation through passive isolation. In this chapter, conclusions regarding the main results are presented, accompanied with recommendations for future research.

7.1. Conclusions

The main idea pursued in this thesis is geared towards an active approach to thermally induced deformations rather than relying on a passive isolation approach. This is done by predicting and controlling thermally induced deformations through accurate modeling and control. Using this approach, a level of overall system performance can be achieved beyond that of a classical mitigation based approach. In this classical approach, thermal induced deformations are mitigated through a sophisticated mechanical design and by relying on passive isolation from the environment. It is expected that this approach is no longer sufficient to achieve the increasingly stringent requirements imposed on the next-generation of mechatronic systems.

The transition towards active thermomechanical control is facilitated by the contributions presented in this thesis. The contributions connect to different research areas as illustrated in Section 1.6, i.e., modeling, actuation, and control. The main conclusions of each of these contributions are presented here.

7.1.1. Modeling next-generation mechatronic systems

In Chapters 2-4 of this thesis a collection of techniques is presented that enable fast and accurate modeling of next-generation mechatronic systems. The detailed exposition presented in Chapter 2 provides insights into the challenges and opportunities in thermal system identification. An approach is presented that enables fast and accurate modeling of multivariate systems through frequency response function identification. Moreover, by incorporating ambient air temperature measurements as additional excitation inputs, the modeling accuracy at lower frequencies can be improved. The parameters of a parametric lumped-mass model are updated by leveraging the frequency response functions to obtain a high-fidelity parametric model to facilitate the application of advanced control techniques.

The results in Chapter 3 provide insights into the accuracy of FRF identification in view of a transient, closed-loop, or multivariate setting. It demonstrates how to judiciously apply identification techniques that could otherwise lead to biased estimations results.

In Chapter 4, a comprehensive framework for local parametric modeling in view of frequency response function identification is presented. It facilitates identification under transient conditions by explicitly estimating and removing the transient component that would otherwise cause a biased estimation. The framework employs a local rational basis with prescribed poles, and leverages prior-knowledge through an appropriate Möbius transformation to achieve improved estimation results.

7.1.2. Transitioning towards active thermal control

In Chapters 5-6 of this thesis, new opportunities for both thermal actuation and thermal control are presented, facilitating an active control approach towards thermally induced deformations. In Chapter 5, a complete framework for modeling and control of thermoelectric elements in mechatronic systems is presented. Thereby facilitating localized heating and cooling through appropriate thermal actuation and addressing many of the pitfalls of existing thermal actuation methods, e.g., non-localized control and heating only. It is shown that through temperature-dependent modeling a high-fidelity parametric model is achieved that is suitable for applications spanning a wide temperature range. Moreover, it enables an appropriate approach for feedback linearization and observer design to expedite the application of advanced linear control techniques. In Chapter 6, an integrated control approach is presented that incorporates existing decentralized control structures and provides complementing coupling controllers to improve overall system performance. It allows for bi-directional coupling between sub-systems and encompasses previous master-slave type solutions to provide a more systematic approach. A double Youla parameterization is constructed such that stability against model uncertainty can be guaranteed. Moreover, a set of coupling controller design guidelines is presented that encompass both a manual loop-shaping approach and $\mathcal{H}_\infty$-controller synthesis. It is expected that inter-disciplinary coupling will be increasingly relevant in next-generation mechatronic systems, e.g., coupling the mechanical and thermal dynamics.

7.1.3. Remarks on practical applicability

This thesis aims to provide a sound theoretical basis to facilitate an improved approach for identification and active thermomechanical control in precision mechatronics. True mastery of the techniques and approaches comes after applying them to real life industrial challenges. In this section, some remarks on practical applicability are provided.

Modeling   Given a thermal system similar to those demonstrated in this thesis, then the user should take into account the following aspects during experiment design for non-parameteric FRF identification. First, whenever possible use periodic excitation to mitigate leakage errors and perform multiple repetitions of the input sequence. Second, emulate operating conditions of the system during the identification experiment, e.g., provide an realistic heat load to achieve a desired temperature range. Third, determine the amount of non-linearity in the system through multiple experiments with different phase realizations. Finally, include the ambient air temperature and external influences in your system model.

By applying the techniques presented in this thesis one can obtain a significantly favorable balance between estimation quality and experiment duration,

7

e.g., through exploitation of transient data. Although the time saved is greatly dependent on the specific applications, anecdotal application of the techniques by the author to several experimental systems has shown potential for experiment time reductions from 25% up to 50%.

Optimization based parameter calibration and data-driven modeling methods are commonplace in academia. While the industrial practitioner often adheres to manual tuning of the model response to a specific measurement result. This is not advisable, since users have a tendency to minimize the peak modeling error in a graphical sense. To truly appreciate the accuracy of the model one should apply the measurement uncertainty as a weighting function and use a cost-function based optimization approach.

Actuation and control   Although thermoelectric elements provide a promising opportunity for an active thermomechanical control, one should be aware of the inherent challenges associated with these elements. Given that the hot side of the element must be thermally conditioned, traditional bulk cooling based on convective cooling or watercircuits remains necessary. The elements should be strategically employed to provide fast control action at performance critical locations.

The control approach presented in Chapter 6 provides a systematic approach to the coupling of multiple sub-systems to improve performance. A common misconception is that the approach requires an elaborate parametric model of the system. While a high fidelity modeling reduces the conservatism of the approach, it can be straightforwardly employed using simplified models and an accurate FRF function that can be directly obtained through system measurements.

7.2. Recommendations for future research

Based on the challenges and contributions demonstrated in this thesis the following recommendations for additional future research are formulated.

7.2.1. Modeling

First, concerning the modeling of thermomechanical behavior in precision mechatronics, the following aspects are important for ongoing research.

Incorporating ambient disturbances   Incorporation of ambient temperature fluctuations can yield improved estimation accuracy for thermal system identification, as demonstrated in Chapter 2. However, since the temperature measurements invariably contain measurement noise it could be considered in an errors-in-variables framework (Söderström, 2018). Moreover, the excitation of the system can also cause fluctuations in the environmental temperature due to convective heat transfer, causing the two inputs to be correlated. In Chapter 2,

the effects of these two phenomena is tacitly assumed to be negligible to facilitate the presentation. In future work, it could be explored whether this assumption is justified and if violation of the assumption is significantly detrimental to the estimation results.

Uncertainty in prior knowledge   In Chapter 4 of this thesis it is shown that using prior knowledge in a local rational basis can yield improved frequency response function estimation accuracy. If no such prior knowledge exists, the poles of the rational functions can be placed at ∞ to recover the LPM as a special case. However, the effects of selecting the prescribed poles at an specific but erroneous location, i.e., not on or near the poles of the true system, has not been analyzed in great detail. In certain cases where the prior knowledge might be uncertain, it could prove more reliable to select the prescribed poles such to recover the LPM. A sensitivity analysis, similar to the approximation error analysis presented in Verbeke and Schoukens (2018),Verbeke (2019, Chapter 2), would provide additional value to the proposed approach.

Data-driven modeling   In modeling and identification of (non-linear) electrical, biochemical, and mechanical systems, data-driven methods show promising results (Noël and Kerschen, 2017; Schoukens et al., 2014). For thermomechanical systems constructing a parametric model often requires extensive modeling effort. By employing the FRF based techniques presented in this thesis a significant reduction in modeling effort can be achieved. However, first principles modeling, e.g., to construct the lumped-mass model, often still represents a substantial time investment. Initial results in Noël et al. (2020) on data-driven modeling of thermoelectric elements are promising and could provide an additional reduction in modeling effort. It should be investigated if applying techniques as presented in Noël and Kerschen (2017) on thermomechanical systems can yield models that are sufficiently suitable for active thermal control.

7.2.2. Actuation and Control

Second, concerning the topics of actuation and control, the following aspects are important for ongoing research.

Modal control   Typically, the thermal control objective in the thermomechanical examples demonstrated in this thesis is to maintain a constant temperature over the full spatial domain of a system. Controlling all, in theory infinite, thermal eigenmodes is infeasible using a limited number of temperature sensors and actuators. The control effort could be concentrated on the most dominant modes, employing a technique demonstrated for mechanical systems in De Rozario et al. (2017) to construct a modal reconstruction using a limited set of sensors.

7

Feedforward control   Typically, a large part of the reference tracking performance in motion systems is achieved through feedforward control, i.e., applying the required control effort based on a given reference (Boeren et al., 2014; Zhang et al., 2012). In thermal systems, reference tracking is less apparent, and a common control objective is to maintain a fixed temperature, which is often achieved solely through feedback control. Employing disturbance observers, similar to the work presented in Mooren et al. (2018); Voorhoeve et al. (2016b) in a mechanical context, to apply feedforward control to reject disturbances such as ambient temperature fluctuations could prove to be highly effective.

Linear parameter varying modeling and control   Several systems presented in this thesis exhibit linear parameter varying (LPV) dynamics as a function of temperature, e.g., the thermal beam setup in Chapter 2 and the TEM in Chapter 5. In this thesis, this temperature dependency was taken into account through dedicated experiments. In Voorhoeve et al. (2020) an approach is presented for modeling and control of LPV systems in a mechanical context through frequency response function measurements. This approach could be investigated further in a thermomechanical context. Initial results in Schepens et al. (2020) on the modeling of flow-dependent dynamics in a local fluid stream heater have proven to be promising.

Control of thermoelectric elements   The approach presented in Chapter 5 is capable of linearizing the input-output dynamics of a thermoelectric element. In practice, a small non-linear residual can not be completely avoided due to modeling errors and parameter uncertainty. A data-driven analysis, based on estimating the Best Linear Approximation (Pintelon and Schoukens, 2012; Schoukens et al., 2016), can be used to estimate the scale of the non-linear residual. It should be investigated if classical linear control approaches, e.g., PID control, offers sufficient robustness in view of this non-linear residual. Alternatively, the Lyapunov based stability proof in Section 5.5.2 of Chapter 5 could be extended to encompass a closed-loop context by including the controller in the analysis. Finally, the application of linear control and in particular integral control can result in "hunting" behavior in thermoelectric systems, where there is a continuous overshoot of the setpoint that can lead to limit cycles. It could be investigated if the hybrid integrator-gain approach described in Van den Eijnden et al. (2020) yields improved results since it aims to reduce overshoot in closed-loop control.

Bibliography

Akçay, H. and Ninness, B. (September 1999). Orthonormal Basis Functions for Modelling Continuous-Time Systems. en. *Signal Processing*, 77(3):261–274. DOI: `10.1016/S0165-1684(99)00039-0`.

Anderson, B. D. (December 1998). From Youla–Kucera to Identification, Adaptive and Nonlinear Control. en. *Automatica*, 34(12):1485–1506. DOI: `10.1016/S0005-1098(98)80002-2`.

Antoulas, A., Sorensen, D., Gallivan, K. A., Van Dooren, P., Grama, A., Hoffmann, C., and Sameh, A. (2004). Model Reduction of Large-Scale Dynamical Systems. en. In *Computational Science - ICCS 2004*. Edited by M. Bubak, G. D. van Albada, P. M. A. Sloot, and J. Dongarra. Lecture Notes in Computer Science, pages 740–747. Berlin, Heidelberg: Springer. DOI: `10.1007/978-3-540-24688-6_96`.

ASML (2020). *Media Library - Supplying the Semiconductor Industry*. en. URL: `https://www.asml.com/en/news/media-library` (visited on 09/23/2020).

Åström, K., Hagander, P., and Sternby, J. (January 1984). Zeros of Sampled Systems. en. *Automatica*, 20(1):31–38. DOI: `10.1016/0005-1098(84)90062-1`.

Atsumi, T., Nakamura, S., Odai, M., Naniwa, I., and Nosaki, S. (2013). Experimental Evaluation of Triple-Stage-Actuator System with Thermal Actuator for Hard Disk Drives. *Journal of Advanced Mechanical Design, Systems, and Manufacturing*, 7(4):722–735. DOI: `10.1299/jamdsm.7.722`.

Attia, M. H. (1998). Modelling, Identification and Control of Thermal Deformation of Machine Tool Structures, Part 2: Generalized Transfer Functions.

Attia, M. H. (1999). Modelling, Identification and Control of Thermal Deformation of Machine Tool Structures, Part 3: Real-Time Estimation of Heat Sources. *Journal of Manufacturing Science and Engineering*, 121:501.

Barton, K. L. and Alleyne, A. G. (2007). Cross-Coupled ILC for Improved Precision Motion Control: Design and Implementation. In *American Control Conference, 2007. ACC'07*, pages 5496–5502.

Beijen, M. A., Voorhoeve, R., Heertjes, M. F., and Oomen, T. (July 2018). Experimental Estimation of Transmissibility Matrices for Industrial Multi-Axis Vibration Isolation Systems. en. *Mechanical Systems and Signal Processing*, 107:469–483. DOI: `10.1016/j.ymssp.2018.01.013`.

Bergman, T. L., editor (2011). *Introduction to Heat Transfer*. 6th ed edition. Hoboken, NJ: Wiley.

Blanken, L., Isil, G., Koekebakker, S., and Oomen, T. (June 2018). Data-Driven Feedforward Learning Using Non-Causal Rational Basis Functions: Application to an Industrial Flatbed Printer. en. In *2018 American Control Conference (ACC 2018)*. Wisconsin, United States: Institute of Electrical and Electronics Engineers (IEEE).

Blanken, L. and Oomen, T. (2019). Multivariable Iterative Learning Control Design Procedures: From Decentralized to Centralized, Illustrated on an Industrial Printer. *IEEE Transactions on Control Systems Technology*:1–8. DOI: `10.1109/TCST.2019.2903021`.

Boeren, F., Bruijnen, D., van Dijk, N., and Oomen, T. (September 2014). Joint Input Shaping and Feedforward for Point-to-Point Motion: Automated Tuning for an Industrial Nanopositioning System. en. *Mechatronics*, 24(6):572–581. DOI: `10.1016/j.mechatronics.2014.03.005`.

Bolder, J. (2015). Flexibility and Robustness in Iterative Learning Control : With Applications to Industrial Printers. PhD, Eindhoven University of Technology.

Bolton, W. (2019). *Mechatronics: Electronic Control Systems in Mechanical and Electrical Engineering*. en. Seventh edition edition. Harlow, England ; New York: Pearson Education Limited.

Bonilla, S. H., Silva, H. R. O., Terra da Silva, M., Franco Gonçalves, R., and Sacomano, J. B. (October 2018). Industry 4.0 and Sustainability Implications: A Scenario-Based Analysis of the Impacts and Challenges. en. *Sustainability*, 10(10):3740. DOI: `10.3390/su10103740`.

Bos, K., Heck, D., Heertjes, M., and van der Kall, R. (June 2018). IO Linearization, Stability, and Control of an Input Non-Affine Thermoelectric System. In *2018 Annual American Control Conference (ACC)*, pages 526–531. Milwaukee, WI: IEEE. DOI: `10.23919/ACC.2018.8431574`.

Bos, K., Heck, D., van der Kall, R., and Heertjes, M. (February 2020). Input-Output Linearized Control of a Thermoelectric Actuator Using an Extended Kalman Filter Observer. In *Euspen Special Interest Group Meeting: Thermal Issues*. Aachen, Germany.

Box, S. (July 2008). Design and Temperature Control for Nanometre Precision. *Mikroniek*. Professional Journal on Precision Engineering, 48(3):12–16.

Bukkems, B., Ruijl, T., Ronde, M., and Lamers, R. (September 2018). Milli-Kelvin Temperature Control Using a Local Fluid Stream Heater. In *DSPE Conference on precision mechatronics*. Sint Michielsgestel, The Netherlands.

Burke, J. V., Henrion, D., Lewis, A. S., and Overton, M. L. (2006). HIFOO - A MATLAB Package for Fixed-Order Controller Design and H-Infinity Optimization. In *IFAC Symposium on Robust Control Design*. Toulouse, France.

Butler, H. (2011). Position Control in Lithographic Equipment [Applications of Control]. *IEEE Control Systems*, 31(5):28–47.

Chen, X., Jiang, T., and Tomizuka, M. (December 2015). Pseudo Youla–Kucera Parameterization with Control of the Waterbed Effect for Local Loop Shaping. en. *Automatica*, 62:177–183. DOI: 10.1016/j.automatica.2015.09.029.

Chen, Z., He, J., Zheng, Y., Song, T., and Deng, Z. (January 2016). An Optimized Feedforward Decoupling PD Register Control Method of Roll-to-Roll Web Printing Systems. *IEEE Transactions on Automation Science and Engineering*, 13(1):274–283.

Cui, Y. J., Wang, K. F., Wang, B. L., Li, J. E., and Zhou, J. Y. (December 2019). A Comprehensive Analysis of Delamination and Thermoelectric Performance of Thermoelectric Pn-Junctions with Temperature-Dependent Material Properties. en. *Composite Structures*, 229:111484. DOI: 10.1016/j.compstruct.2019.111484.

Dixit, U. S., Hazarika, M., and Davim, J. P. (2017). History of Mechatronics. en. In *A Brief History of Mechanical Engineering*. Edited by U. S. Dixit, M. Hazarika, and J. P. Davim. Materials Forming, Machining and Tribology, pages 147–164. Cham: Springer International Publishing. DOI: 10.1007/978-3-319-42916-8_7.

van den Eijnden, S. J. A. M. and Heertjes, M. F. and Heemels, W. P. M. H. and Nijmeijer, H. (October 2020). Hybrid Integrator-Gain Systems: A Remedy for Overshoot Limitations in Linear Control? *IEEE Control Systems Letters*, 4(4):1042–1047. DOI: 10.1109/LCSYS.2020.2998946.

Evers, E. (June 2016). Synchronized Stage Motion Control: A Double-Youla Approach to Systematic Bi-Directional Controller Coupling. MSc Thesis, Eindhoven University of Technology, Eindhoven.

Evers, E., de Jager, B., and Oomen, T. (January 2018a). Improved Local Rational Method by Incorporating System Knowledge: With Application to Mechanical and Thermal Dynamical Systems. en. *IFAC-PapersOnLine*. 18th IFAC Symposium on System Identification SYSID 2018, 51(15):808–813. DOI: 10.1016/j.ifacol.2018.09.127.

Evers, E., De Jager, B., and Oomen, T. (October 2018b). Thermo-Mechanical Behavior in Precision Motion Control: Unified Framework for Fast and Accurate FRF Identification. In *IECON 2018 - 44th Annual Conference of the*

IEEE Industrial Electronics Society, pages 4618–4623. DOI: `10.1109/IECON.2018.8592781`.

Evers, E., Lamers, R., and Oomen, T. (April 2019a). Thermally Induced Deformations in Electron Microscopy: Challenges and Opportunities for System Identification. English. *Mikroniek*, (2):12–18.

Evers, E., Slenders, R., van Gils, R., and Oomen, T. (2020). Temperature-Dependent Modeling of Thermoelectric Elements. English. In *21st IFAC World Congress*.

Evers, E., van Tuijl, N., Lamers, R., and Oomen, T. (January 2019b). Identifying Thermal Dynamics for Precision Motion Control. en. *IFAC-PapersOnLine*. 8th IFAC Symposium on Mechatronic Systems MECHATRONICS 2019, 52(15):73–78. DOI: `10.1016/j.ifacol.2019.11.652`.

Evers, E., van de Wal, M., and Oomen, T. (July 2017). Synchronizing Decentralized Control Loops for Overall Performance Enhancement: A Youla Framework Applied to a Wafer Scanner. en. *IFAC-PapersOnLine*. 20th IFAC World Congress, 50(1):10845–10850. DOI: `10.1016/j.ifacol.2017.08.2382`.

Evers, E., van de Wal, M., and Oomen, T. (February 2019c). Beyond Decentralized Wafer/Reticle Stage Control Design: A Double-Youla Approach for Enhancing Synchronized Motion. en. *Control Engineering Practice*, 83:21–32. DOI: `10.1016/j.conengprac.2018.10.011`.

Fraser, S., Attia, M. H., and Osman, M. O. M. (1998). Modelling, Identification and Control of Thermal Deformation of Machine Tool Structures, Part 1: Concept of Generalized Modelling. en. *Journal of Manufacturing Science and Engineering*, 120(3):623. DOI: `10.1115/1.2830167`.

Freudenberg, J., Hollot, C., Middleton, R., and Toochinda, V. (August 2003). Fundamental Design Limitations of the General Control Configuration. en. *IEEE Transactions on Automatic Control*, 48(8):1355–1370. DOI: `10.1109/TAC.2003.815017`.

Geerardyn, E. (2016). Development of User-Friendly System Identification Techniques. PhD Thesis, Vrije Universiteit Brussel.

Geerardyn, E., Lumori, M. L. D., and Lataire, J. (October 2015). FRF Smoothing to Improve Initial Estimates for Transfer Function Identification. *IEEE Transactions on Instrumentation and Measurement*, 64(10):2838–2847.

Geerardyn, E., Oomen, T., and Schoukens, J. (2014). Enhancing H∞ Norm Estimation Using Local LPM/LRM Modeling: Applied to an AVIS. In *IFAC 19th Triennial World Congress*, pages 10856–10861.

van Gils, Rob (September 2017). Practical Thermal Control by Thermo-Electric Actuators. In *2017 23rd International Workshop on Thermal Investigations of ICs and Systems (THERMINIC)*, pages 1–6. Amsterdam: IEEE. DOI: `10.1109/THERMINIC.2017.8233829`.

Guiatni, M., Drif, A., and Kheddar, A. (2007). Thermoelectric Modules: Recursive Non-Linear ARMA Modeling, Identification and Robust Control. In *IECON 2007 - 33rd Annual Conference of the IEEE Industrial Electronics Society*, pages 568–573. Taipei, Taiwan: IEEE. DOI: `10.1109/IECON.2007.4460142`.

Guo, J. (May 2014). Positioning Performance Enhancement via Identication and Control of Thermal Dynamics: A MIMO Wafer Table Case Study. MSc Thesis, Eindhoven University of Technology.

Heertjes, M. and Temizer, B. (2012). Data-Based Control Tuning in Master-Slave Systems. In *American Control Conference (ACC), 2012*, pages 2461–2466. IEEE.

Heertjes, M., Butler, H., Dirkx, N., van der Meulen, S., Ahlawat, R., O'Brien, K., Simonelli, J., Teng, K.-T., and Zhao, Y. (July 2020). Control of Wafer Scanners: Methods and Developments. In *2020 American Control Conference (ACC)*, pages 3686–3703. DOI: `10.23919/ACC45564.2020.9147464`.

van Herpen, Robbert and Oomen, Tom and Kikken, Edward and van de Wal, Marc and Aangenent, Wouter and Steinbuch, Maarten (2014). Exploiting Additional Actuators and Sensors for Nano-Positioning Robust Motion Control. *Mechatronics*, 24(6):619–631.

van Herpen, Robbert (2014). Identification for Control of Complex Motion Systems : Optimal Numerical Conditioning Using Data-Dependent Polynomial Bases. PhD Thesis, Eindhoven University of Technology, Eindhoven.

Heuberger, P. S. C., P. M. J. van den Hof, and B. Wahlberg, editors (2005). *Modelling and Identification with Rational Orthogonal Basis Functions*. en. London: Springer.

Hong, J. and Bernstein, D. S. (1998). Bode Integral Constraints, Collocation, and Spillover in Active Noise and Vibration Control. *IEEE Transactions on Control Systems Technology*, 6(1):111–120.

van Horssen, E. P. (February 2018). Data-Intensive Feedback Control : Switched Systems Analysis and Design. English. PhD thesis, Eindhoven University of Technology.

Houpis, C. H. and Lamont, G. B. (1992). *Digital Control Systems: Theory, Hardware, Software*. 2nd ed edition. New York: McGraw-Hill.

van den Hurk, David and Weiland, Siep and van Berkel, Koos (March 2018). Modeling and Localized Feedforward Control of Thermal Deformations Induced by a Moving Heat Load. In *2018 SICE International Symposium on Control Systems (SICE ISCS)*, pages 171–178. DOI: `10.23919/SICEISCS.2018.8330172`.

Isermann, R. (2005). *Mechatronic Systems: Fundamentals*. en. London: Springer.

Jabben, L. and van Eijk, J. (2011). Performance Analysis and Design of Mechatronic Systems. *Mikroniek*, 51(2):5–12.

Jiang, J., Kaigala, G. V., Marquez, H. J., and Backhouse, C. J. (January 2012). Nonlinear Controller Designs for Thermal Management in PCR Amplification. *IEEE Transactions on Control Systems Technology*, 20(1):11–30. DOI: `10.1109/TCST.2010.2099660`.

de Jonge, Niels and Poirier-Demers, Nicolas and Demers, Hendrix and Peckys, Diana B. and Drouin, Dominique (August 2010). Nanometer-Resolution Electron Microscopy through Micrometers-Thick Water Layers. en. *Ultramicroscopy*, 110(9):1114–1119. DOI: `10.1016/j.ultramic.2010.04.001`.

Ju, C., Wang, X., Dui, G., Uhl, C. G., and Xin, L. (July 2019). Theoretical Analysis of the Cooling Performance of a Thermoelectric Element with Temperature-Dependent Material Properties. en. *Journal of Electronic Materials*, 48(7):4627–4636. DOI: `10.1007/s11664-019-07217-3`.

Karimi, A. and Zhu, Y. (2014). Robust H-Infinity Controller Design Using Frequency-Domain Data. In *19th IFAC World Congress*. Cape Town, South Africa.

Kaya, M. (2014). Experimental Study on Active Cooling Systems Used for Thermal Management of High-Power Multichip Light-Emitting Diodes. en. *The Scientific World Journal*, 2014:1–7. DOI: `10.1155/2014/563805`.

van Keulen, Thijs and Huijben, Lars and Oomen, Tom (July 2017). Identification of Control-Relevant Diesel Engine Models Using a Local Linear Parametric Approach. en. *IFAC-PapersOnLine*, 50(1):7836–7841. DOI: `10.1016/j.ifacol.2017.08.1061`.

Koevoets, A. H., Eggink, H. J., van der Sanden, J., Dekkers, J., and Ruijl, T. A. M. (2007). Optimal Sensor Configuring Techniques for the Compensation of Thermo-Elastic Deformations in High-Precision Systems. In pages 208–213. IEEE. DOI: `10.1109/THERMINIC.2007.4451779`.

Koevoets, A. H., van der Sanden, J., and Ruijl, T. (2009). Thermal-Elastic Compensation Models for Position Control. In *Proceedings of the ASPE Annual Meeting*. Volume 2009.

Lambregts, C. J., Heertjes, M. F., and van der Veek, B. J. (2015). Multivariable Feedback Control in Stage Synchronization. In *American Control Conference (ACC), 2015*, pages 4149–4154. IEEE.

Lamers, R. (2010). Thermal Effects in Precision Systems. (2).

Levy, E. C. (1959). Complex-Curve Fitting. *IRE Transactions on Automatic Control*, AC-4(1):37–43. DOI: `10.1109/TAC.1959.6429401`.

Ljung, L. (1999). *System Identification: Theory for the User*. 2nd ed edition. Prentice Hall Information and System Sciences Series. Upper Saddle River, NJ: Prentice Hall PTR.

Looijen, V. A. and Heertjes, M. F. (August 2018). Robust Synchronization of Motion in Wafer Scanners Using Particle Swarm Optimization. In *2018 IEEE*

Conference on Control Technology and Applications (CCTA), pages 1102–1107. DOI: `10.1109/CCTA.2018.8511380`.

Lu, T.-T. and Shiou, S.-H. (2002). Inverses of 2$\times$ 2 Block Matrices. *Computers & Mathematics with Applications*, 43(1-2):119–129.

Ma, C. (August 1988). Comments on "A Necessary and Sufficient Condition for Stability of a Perturbed System" by Q. Huang and R. Liu. *IEEE Transactions on Automatic Control*, 33(8):796–797. DOI: `10.1109/9.1305`.

Maciejowski, J. M. (1989). *Multivariable Feedback Design*. Electronic Systems Engineering Series. Wokingham, England ; Addison-Wesley.

Manyika, J., Sinclair, J., Dobbs, R., Strube, G., Rassey, L., Mischke, J., Remes, J., Roxburgh, C., and George, K. (November 2012). *Manufacturing the Future: The next Era of Global Growth and Innovation*. English. McKinsey Global Institute.

McKelvey, T. and Guérin, G. (July 2012). Non-Parametric Frequency Response Estimation Using a Local Rational Model. en. *IFAC Proceedings Volumes*, 45(16):49–54.

Mishra, S., Yeh, W., and Tomizuka, M. (2008). Iterative Learning Control Design for Synchronization of Wafer and Reticle Stages. In *American Control Conference, 2008*, pages 3908–3913. IEEE.

Mitrani, D., Tome, J., Salazar, J., Turo, A., Garcia, M., and Chavez, J. (2004). Methodology for Extracting Thermoelectric Module Parameters. In *Proceedings of the 21st IEEE Instrumentation and Measurement Technology Conference*, pages 564–568. Como, Italy: IEEE. DOI: `10.1109/IMTC.2004.1351112`.

Monteyne, G., Vandersteen, G., Pintelon, R., and Ugryumova, D. (August 2013). Transient Suppression in FRF Measurement: Comparison and Analysis of Four State-of-the-Art Methods. en. *Measurement*, 46(7):2210–2222. DOI: `10.1016/j.measurement.2013.03.032`.

Moore, G. (April 1965). Cramming More Components Onto Integrated Circuits. en. *Electronics*, 38(8):33–35.

Mooren, N. F. M., Voorhoeve, R. J., Dirkx, N. J., and Oomen, T. (2018). Compensating Quasi-Static Disturbances for Inferential Control: An Observer-Based Approach Applied to a Wafer Stage. English. In *Proceedings of the IEEEJ International Workshop on Sensing, Actuation, Motion Control, and Optimization (SAMCON 2018)*, pages 1–2.

Morgan, V. T. (January 1975). The Overall Convective Heat Transfer from Smooth Circular Cylinders. en. *Advances in heat transfer*. DOI: `10.1016/S0065-2717(08)70075-3`.

Navarrete, M. O., Heertjes, M. F., and Schmidt, R. H. M. (2015). Common Zeros in Synchronization of High-Precision Stage Systems. In *Mechatronics (ICM), 2015 IEEE International Conference On*, pages 602–607.

Bibliography

Niemann, H. (September 2003). Dual Youla Parameterisation. en. *IEE Proceedings - Control Theory and Applications*, 150(5):493–497. DOI: 10.1049/ip-cta:20030685.

Ninness, B. (Jan./1998). Estimation of 1/f Noise. en. *IEEE Transactions on Information Theory*, 44(1):32–46. DOI: 10.1109/18.650986.

Ninness, B., Hjalmarsson, H., and Gustafsson, F. (July 1999). The Fundamental Role of General Orthonormal Bases in System Identification. en. *IEEE Transactions on Automatic Control*, 44(7):1384–1406. DOI: 10.1109/9.774110.

Ninness, B., Gibson, S., and Weller, S. (June 2000). Practical Aspects of Using Orthonormal System Parameterisations in Estimation Problems. en. *IFAC Proceedings Volumes*, 33(15):463–468. DOI: 10.1016/S1474-6670(17)39793-8.

Ninness, B. and Gustafsson, F. (1997). A Unifying Construction of Orthonormal Bases for System Identification. *IEEE Transactions on Automatic Control*, 42(4):515–521.

Noël, J. P. and Kerschen, G. (January 2017). Nonlinear System Identification in Structural Dynamics: 10 More Years of Progress. en. *Mechanical Systems and Signal Processing*, 83:2–35. DOI: 10.1016/j.ymssp.2016.07.020.

Noël, J.-P., Evers, E., and Oomen, T. A. E. (March 2020). Nonlinear Data-Driven Identification of a Thermo-Electric System. English. In *39th Benelux Meeting on Systems and Control*.

Oomen, T. (2018). Advanced Motion Control for Precision Mechatronics: Control, Identification, and Learning of Complex Systems. en. *IEEJ Journal of Industry Applications*, 7(2):127–140. DOI: 10.1541/ieejjia.7.127.

Oomen, T., Grassens, E., and Hendriks, F. (July 2015). Inferential Motion Control: Identification and Robust Control Framework for Positioning an Unmeasurable Point of Interest. *IEEE Transactions on Control Systems Technology*, 23(4):1602–1610. DOI: 10.1109/TCST.2014.2371830.

Oomen, T., van der Maas, R., Rojas, C. R., and Hjalmarsson, H. (November 2014a). Iterative Data-Driven H Norm Estimation of Multivariable Systems With Application to Robust Active Vibration Isolation. *IEEE Transactions on Control Systems Technology*, 22(6):2247–2260. DOI: 10.1109/TCST.2014.2303047.

Oomen, T., van Herpen, R., Quist, S., van de Wal, M., Bosgra, O., and Steinbuch, M. (January 2014b). Connecting System Identification and Robust Control for Next-Generation Motion Control of a Wafer Stage. *IEEE Transactions on Control Systems Technology*, 22(1):102–118. DOI: 10.1109/TCST.2013.2245668.

Paalvast, S. L. (2010). Thermal Actuation for Precision Micro Motion and Positioning. en.

Peumans, D., Busschots, C., Vandersteen, G., and Pintelon, R. (July 2018). Improved FRF Measurements of Lightly Damped Systems Using Local Rational Models. en. *IEEE Transactions on Instrumentation and Measurement*, 67(7):1749–1759. DOI: 10.1109/TIM.2018.2800958.

Philips (2020). *Philips Minicare I-20*. nl-nl. URL: https://www.philips.nl/healthcare/product/HCNOCTN496/minicare-i20-enabling-near-patient-blood-testing-in-the-acute-care-setting (visited on 09/23/2020).

Pintelon, R. and Schoukens, J. (2012). *System Identification: A Frequency Domain Approach*. 2nd ed edition. Hoboken, New Jersey: John Wiley & Sons Inc.

Pintelon, R., Schoukens, J., Vandersteen, G., and Barbé, K. (April 2010). Estimation of Nonparametric Noise and FRF Models for Multivariable Systems - Part I: Theory. en. *Mechanical Systems and Signal Processing*, 24(3):573–595. DOI: 10.1016/j.ymssp.2009.08.009.

Pourkiaei, S. M., Ahmadi, M. H., Sadeghzadeh, M., Moosavi, S., Pourfayaz, F., Chen, L., Pour Yazdi, M. A., and Kumar, R. (November 2019). Thermoelectric Cooler and Thermoelectric Generator Devices: A Review of Present and Potential Applications, Modeling and Materials. en. *Energy*, 186:115849. DOI: 10.1016/j.energy.2019.07.179.

Prempain, E., Turner, M. C., and Postlethwaite, I. (December 2009). Coprime Factor Based Anti-Windup Synthesis for Parameter-Dependent Systems. en. *Systems & Control Letters*, 58(12):810–817. DOI: 10.1016/j.sysconle.2009.09.002.

Qiu, C. and Shi, W. (July 2020). Comprehensive Modeling for Optimized Design of a Thermoelectric Cooler with Non-Constant Cross-Section: Theoretical Considerations. en. *Applied Thermal Engineering*, 176:115384. DOI: 10.1016/j.applthermaleng.2020.115384.

Qiu, X. and Yuan, J. (January 2005). Temperature Control for PCR Thermocyclers Based on Peltier-Effect Thermoelectric. In *2005 IEEE Engineering in Medicine and Biology 27th Annual Conference*, pages 7509–7512. DOI: 10.1109/IEMBS.2005.1616249.

Relan, R., Tiels, K., Timmermans, J.-M., and Schoukens, J. (July 2017a). A Local Polynomial Approach to Nonparametric Estimation of the Best Linear Approximation of Lithium-Ion Battery From Multiple Datasets. *IEEE Control Systems Letters*, 1(1):182–187. DOI: 10.1109/LCSYS.2017.2712364.

Relan, R., Tiels, K., Timmermans, J.-M., and Schoukens, J. (2017b). Estimation of Best Linear Approximation from Varying Operating Conditions for the Identification of a Li-Ion Battery Model. *IFAC-PapersOnLine*, 50(1):4739–4744.

de Rozario, R. and Voorhoeve, R. J. and Aangenent, W. and Oomen, Tom (July 2017). Global Feedforward Control of Spatio-Temporal Mechanical Systems: With Application to a Prototype Wafer Stage. en. *IFAC-PapersOnLine*. 20th IFAC World Congress, 50(1):14575–14580. DOI: `10.1016/j.ifacol.2017.08.2100`.

Saathof, R., Wansink, M. V., Hooijkamp, E. C., Spronck, J. W., and Munnig Schmidt, R. H. (November 2016). Deformation Control of a Thermal Active Mirror. en. *Mechatronics*, 39:12–27. DOI: `10.1016/j.mechatronics.2016.07.002`.

Sakata, K. and Fujimoto, H. (2009). Master-Slave Synchronous Position Control for Precision Stages Based on Multirate Control and Dead-Time Compensation. In *Advanced Intelligent Mechatronics, 2009. AIM 2009. IEEE/ASME International Conference On*, pages 263–268. IEEE.

Salmons, B. S., Katz, D. R., and Trawick, M. L. (March 2010). Correction of Distortion Due to Thermal Drift in Scanning Probe Microscopy. en. *Ultramicroscopy*, 110(4):339–349. DOI: `10.1016/j.ultramic.2010.01.006`.

van der Sanden, J.C.G. and Ruijl, T. A. M. (December 2007). Thermal Transient Analysis of Complex Systems Using Structured Lumped Mass Models. In *Proceedings of the Topical Meeting: Thermal Effects in Precision Systems*, pages 32–35. Maastricht.

Schepens, S., Bukkems, B., Ruijl, T., Evers, E., and Oomen, T. (February 2020). Modelling & Identification for Thermal Control of Cooling Water with Varying Flow. In *Euspen Special Interest Group Meeting: Thermal Issues*. Aachen, Germany.

van Schoot, Jan and Troost, Kars and Bornebroek, Frank and van Ballegoij, Rob and Lok, Sjoerd and Krabbendam, Peter and Stoeldraijer, Judon and Loopstra, Erik and Benschop, Jos P. and Finders, Jo and Meiling, Hans and van Setten, Eelco and Kneer, Bernhard and Kuerz, Peter and Kaiser, Winfried and Heil, Tilmann and Migura, Sascha and Neumann, Jens Timo (October 2017). High-NA EUV Lithography Enabling Moore's Law in the next Decade. In *International Conference on Extreme Ultraviolet Lithography 2017*. Volume 10450, 104500U. International Society for Optics and Photonics. DOI: `10.1117/12.2280592`.

Schoukens, J., Vaes, M., and Pintelon, R. (June 2016). Linear System Identification in a Nonlinear Setting: Nonparametric Analysis of the Nonlinear Distortions and Their Impact on the Best Linear Approximation. *IEEE Control Systems*, 36(3):38–69. DOI: `10.1109/MCS.2016.2535918`.

Schoukens, J., Vandersteen, G., Barbé, K., and Pintelon, R. (2009). Nonparametric Preprocessing in System Identification: A Powerful Tool. In *Control Conference (ECC), 2009 European*, pages 1–14. IEEE.

Schoukens, J., Vandersteen, G., Rolain, Y., and Pintelon, R. (October 2012). Frequency Response Function Measurements Using Concatenated Subrecords With Arbitrary Length. en. *IEEE Transactions on Instrumentation and Measurement*, 61(10):2682–2688. DOI: `10.1109/TIM.2012.2196400`.

Schoukens, M., Tiels, K., Widanage, W. D., Abu-Rmileh, A., Schoukens, J., and Marconato, A. (November 2014). Comparison of Several Data-Driven Non-Linear System Identification Methods on a Simplified Glucoregulatory System Example. en. *IET Control Theory & Applications*, 8(17):1921–1930. DOI: `10.1049/iet-cta.2014.0534`.

Schrama, R. J., Bongers, P. M., and Bosgra, O. H. (1992). Robust Stability under Simultaneous Perturbations of Linear Plant and Controller. In *Decision and Control, 1992., Proceedings of the 31st IEEE Conference On*, pages 2137–2139. IEEE.

Seron, M., Braslavsky, J., and Goodwin, G. C. (1997). *Fundamental Limitations in Filtering and Control*. Communications and Control Engineering. London ; New York: Springer.

Shamma, J. S. (2012). An Overview of LPV Systems. en. In *Control of Linear Parameter Varying Systems with Applications*. Edited by J. Mohammadpour and C. W. Scherer, pages 3–26. Boston, MA: Springer US. DOI: `10.1007/978-1-4614-1833-7_1`.

Shao, H., Yang, Z., and Yu, Y. (July 2014). LPV Model-Based Temperature Control of Thermoelectric Device. In *2014 International Conference on Mechatronics and Control (ICMC)*, pages 1012–1017. DOI: `10.1109/ICMC.2014.7231706`.

Skogestad, S. and Postlethwaite, I. (2009). *Multivariable Feedback Control: Analysis and Design*. eng. 2. ed., reprint edition. Chichester: Wiley.

Söderström, T. (2018). *Errors-in-Variables Methods in System Identification*. en. Communications and Control Engineering. Springer International Publishing. DOI: `10.1007/978-3-319-75001-9`.

Söderström, T. and Stoica, P. (1989). *System Identification*. Prentice Hall International Series in Systems and Control Engineering. New York: Prentice Hall.

de Gelder, Edgar. and van de Wal, Marc and Scherer, Carsten and Hol, Camile and Bosgra, Okko (2006). Nominal and Robust Feedforward Design With Time Domain Constraints Applied to a Wafer Stage. en. *Journal of Dynamic Systems, Measurement, and Control*, 128(2):204. DOI: `10.1115/1.2192821`.

Stoev, J., Oomen, T., and Schoukens, J. (2016). Tensor Methods for MIMO Decoupling Using Frequency Response Functions. en. *IFAC-PapersOnLine*, 49(21):447–453. DOI: `10.1016/j.ifacol.2016.10.644`.

Bibliography

Takenaka, S. (1925). On the Orthogonal Functions and a New Formula of Inter-
     polation. en. *Japanese Journal of Mathematics: Transactions and Abstracts*,
     2:129–145.

Tarău, A. N., Nuij, P., and Steinbuch, M. (January 2011). Model-Based
     Drift Control for Electron Microscopes. en. *IFAC Proceedings Volumes*,
     44(1):8583–8588. DOI: `10.3182/20110828-6-IT-1002.02190`.

Tay, T.-T., Mareels, I., and Moore, J. B. (1998). *High Performance Control*.
     Springer Science & Business Media.

Tomizuka, M. (1987). Zero Phase Error Tracking Algorithm for Digital Control.
     en. *Journal of Dynamic Systems, Measurement, and Control*, 109(1):65. DOI:
     `10.1115/1.3143822`.

Touzelbaev, M. N., Miler, J., Yang, Y., Refai-Ahmed, G., and Goodson, K. E.
     (2013). High-Efficiency Transient Temperature Calculations for Applications
     in Dynamic Thermal Management of Electronic Devices. *Journal of Elec-
     tronic Packaging*, 135(3):031001.

Ustundag, A. and Cevikcan, E. (2018). *Industry 4.0: Managing The Digital
     Transformation*. en. Springer Series in Advanced Manufacturing. Springer
     International Publishing. DOI: `10.1007/978-3-319-57870-5`.

Verbeke, D. (2019). Towards User-Friendly Identification of Advanced Motion
     Systems. en. PhD, Vrije Universiteit Brussel.

Verbeke, D. and Schoukens, J. (2018). A Study of Approximation Errors in
     Local Parametric Approaches to Frequency Response Function Estimation.
     en. *IFAC-PapersOnLine*, 51(15):814–819. DOI: `10.1016/j.ifacol.2018.`
     `09.126`.

Vinnicombe, G. (2000). *Uncertainty and Feedback - H∞Loop-Shaping and the
     ν-Gap Metric*. en. Imperial College Press. DOI: `10.1142/9781848160453`.

Voorhoeve, R., de Rozario, R., Aangenent, W., and Oomen, T. (2020). Identi-
     fying Position-Dependent Mechanical Systems: A Modal Approach Applied
     to a Flexible Wafer Stage. *IEEE Transactions on Control Systems Technol-
     ogy*:1–13. DOI: `10.1109/TCST.2020.2974140`.

Voorhoeve, R., de Rozario, R., and Oomen, T. (2016a). Identification for Mo-
     tion Control: Incorporating Constraints and Numerical Considerations. In
     American Control Conference (ACC), 2016, pages 6209–6214. IEEE.

Voorhoeve, R., Dirkx, N., Melief, T., Aangenent, W., and Oomen, T. (2016b).
     Estimating Structural Deformations for Inferential Control: A Disturbance
     Observer Approach. en. In volume 49. 21, pages 642–648.

Voorhoeve, R., van der Maas, A., and Oomen, T. (May 2018). Non-Parametric
     Identification of Multivariable Systems: A Local Rational Modeling Approach
     with Application to a Vibration Isolation Benchmark. en. *Mechanical Systems
     and Signal Processing*, 105:129–152. DOI: `10.1016/j.ymssp.2017.11.044`.

Voorhoeve, R., van Rietschoten, A., Geerardyn, E., and Oomen, T. (2015). Identification of High-Tech Motion Systems: An Active Vibration Isolation Benchmark. *IFAC-PapersOnLine*, 48(28):1250–1255.

de Vries, Douwe K. and Van den Hof, Paul MJ (1998). Frequency Domain Identification with Generalized Orthonormal Basis Functions. *IEEE Transactions on Automatic Control*, 43(5):656–669.

van de Wal, Marc and van Baars, Gregor and Sperling, Frank and Bosgra, Okko (2001). Experimentally Validated Multivariable/Spl Mu/Feedback Controller Design for a High-Precision Wafer Stage. In *Decision and Control, 2001. Proceedings of the 40th IEEE Conference On.* Volume 2, pages 1583–1588. IEEE.

van de Wal, Marc and van Baars, Gregor and Sperling, Frank and Bosgra, Okko (July 2002). Multivariable Feedback Control Design for High-Precision Wafer Stage Motion. en. *Control Engineering Practice*, 10(7):739–755. DOI: 10.1016/S0967-0661(01)00166-6.

Wang, C., Yin, W., and Duan, G. (2006). Cross-Coupling Control for Synchronized Scan of Experimental Wafer and Reticle Stage. In *Technology and Innovation Conference, 2006. ITIC 2006. International*, pages 1168–1172. IET.

Weck, M., McKeown, P., Bonse, R., and Herbst, U. (1995). Reduction and Compensation of Thermal Errors in Machine Tools. en. *CIRP Annals*, 44(2):589–598. DOI: 10.1016/S0007-8506(07)60506-X.

Wikimedia and Fylip22 (November 2010). *Cam Timer Artwork by Fylip22*. URL: https://commons.wikimedia.org/wiki/File:Sequenceur_a_cames_001.jpg (visited on 09/23/2020).

Yager, P., Edwards, T., Fu, E., Helton, K., Nelson, K., Tam, M. R., and Weigl, B. H. (July 2006). Microfluidic Diagnostic Technologies for Global Public Health. en. *Nature*, 442(7101):412–418. DOI: 10.1038/nature05064.

Youla, D., Jabr, H., and Bongiorno, J. (1976). Modern Wiener-Hopf Design of Optimal Controllers–Part II: The Multivariable Case. *IEEE Transactions on Automatic Control*, 21(3):319–338.

Zhang, J., Xu, H., Zou, Q., and Peng, C. (September 2012). Inversion-Based Robust Feedforward–Feedback Two-Degree-of-Freedom Control Approach for Multi-Input Multi-Output Systems with Uncertainty. en. *IET Control Theory & Applications*, 6(14):2279–2291. DOI: 10.1049/iet-cta.2011.0244.

Zhou, K., Doyle, J. C., and Glover, K. (1996). *Robust and Optimal Control.* Upper Saddle River, N.J: Prentice Hall.

Zhu, H., Zhang, H., Ni, S., Korabečná, M., Yobas, L., and Neuzil, P. (September 2020). The Vision of Point-of-Care PCR Tests for the COVID-19 Pandemic and Beyond. en. *TrAC Trends in Analytical Chemistry*, 130:115984. DOI: 10.1016/j.trac.2020.115984.

Bibliography

van Zundert, Jurgen and Luijten, Fons and Oomen, Tom (2018). Achieving Perfect Causal Feedforward Control in Presence of Nonminimum-Phase Behavior - Exploiting Additional Actuators and Squaring Down. In *2018 IEEE American Control Conference*. Milwaukee, Wisconsin.

About the author

Enzo Evers was born in the fall of 1990 in Tilburg, The Netherlands. He completed his high school years in 2008 at the Theresia Lyceum in Tilburg, The Netherlands. He then started his higher education on Mechanical Engineering at the Eindhoven University of Technology. He received his Bachelor of Science degree in 2012. He then continued to specialize in the field of control systems technology and received his Master of Science (cum laude) in 2016. He conducted his internship at ETEL, Switzerland on the topic of frequency response function identification and iterative learning control. His MSc graduation research was performed at ASML research on the topic of synchronized stage motion control to improve the overall system performance of a waferscanner.

In October 2016, Enzo started his Ph.D. research in the Control Systems Technology group at the department of Mechanical Engineering at the Eindhoven University of Technology under the supervision of Bram de Jager and Tom Oomen. His research is focused on identification and active thermomechanical control in the context of precision mechatronics. The results of his research can be found in this thesis.

List of publications

Peer-reviewed journal articles

- Evers, E., Slenders, R., van Gils, R., and Oomen, T. Temperature-Dependent Modeling of Thermoelectric Elements. *In preparation for journal submission.*

- Evers, E., de Jager, B., and Oomen, T. Incorporating prior knowledge in local parametric modeling for frequency response measurements: Applied to thermal/mechanical systems. *Under review.*

- Evers, E., van Tuijl, N., Lamers, R., de Jager, B., and Oomen, T. Fast and Accurate Identification of Thermal Dynamics for Precision Motion Control: Exploiting Transient Data and Additional Disturbance Inputs. Mechatronics, Vol 70, Article 102401, 2020.

- Evers, E., van de Wal, M., and Oomen,T. Beyond decentralized wafer/reticle stage control design: a double-Youla approach for enhancing synchronized motion. *Control Engineering Practice.* 83, p21-32, 2019.

Contribution to professional journal

- Evers, E., Lamers, R. and Oomen, T., Thermally induced deformations in electron microscopy: challenges and opportunities for system identification. *Mikroniek.* 2, p. 12-18, 2019.

Peer-reviewed articles in conference proceedings

- Evers, E., Voorhoeve, R., and Oomen, T. On Frequency Response Function Identification for Advanced Motion Control, IEEE 16th International Workshop on Advanced Motion Control (AMC2020) - Kristiansand, Norway, 2020.

- Evers, E., Slenders, R., van Gils, R., and Oomen, T. Temperature-Dependent Modeling of Thermoelectric Elements. 21th World Congress

of the International Federation of Automatic Control (IFAC 2020 World Congress) - Berlin, Germany. 2020.

○ Scheepens, S.J.M.C., Bukkems, B., Ruijl, T., Evers, E., and Oomen, T. Modelling & Identification for Thermal Control of Cooling Water with Varying Flow. Euspen Special Interest Group Meeting: Thermal Issues, Aachen, Germany, 2020.

● Evers, E., van Tuijl, N., Lamers, R., and Oomen, T. Identifying Thermal Dynamics for Precision Motion Control, IFAC-PapersOnLine (8th IFAC Symposium on Mechatronic Systems MECHATRONICS 2019, Vienna, Austria), vol. 52, no. 15, pp. 73–78, 2019.

● Evers, E., de Jager, B., and Oomen, "Thermo-Mechanical Behavior in Precision Motion Control: Unified Framework for Fast and Accurate FRF Identification," in IECON 2018 - 44th Annual Conference of the IEEE Industrial Electronics Society, 2018, pp. 4618–4623.

● Evers, E., de Jager, B., and Oomen, T. Improved Local Rational Method by incorporating system knowledge: with application to mechanical and thermal dynamical systems, IFAC-PapersOnLine (18th IFAC Symposium on System Identification SYSID 2018, Stockholm, Sweden), vol. 51, no. 15, pp. 808–813, 2018.

● Evers, E., van de Wal, M., and Oomen,T. Synchronizing Decentralized Control Loops for Overall Performance Enhancement: A Youla Framework Applied to a Wafer Scanner, IFAC-PapersOnLine (20th World Congress of the International Federation of Automatic Control (IFAC 2017 World Congress) - Toulouse, France), vol. 50, no. 1, pp. 10845–10850, 2017.

Dankwoord

Het dankwoord, de laatste loodjes van een lang en intensief traject dat dient ter vorming van een jonge doctor uit een kersverse ingenieur. Het hele proces heeft sterke gelijkenissen met de fysiek en mentaal zware uitdagingen die ik eerder ben aangegaan zoals de Kennedymars en de 88 tempel pelgrimstocht op Shikoku. Je begint altijd met goede moed en vol zelfvertrouwen, gaandeweg ga je op de gezicht en loop je blaren, en als je eenmaal goed over de helft bent dan weiger je uit koppigheid te stoppen. Uiteindelijk blijkt er voor de ontwikkeling van je karakter altijd meer in te zitten dan simpelweg de gelopen kilometers.

Allereerst wil ik graag mijn promotoren bedanken voor hun onmisbare bijdrage aan dit proefschrift. Beide hebben op geheel eigen complementaire wijze mij voorzien van visie, inspiratie en koerscorrecties. Tom, jouw ogenschijnlijk oneindige positivisme en enthousiasme waren de perfecte tegenhanger voor mijn momenten van melancholie. Bram, jouw kritische en nuchtere blik op zaken waar ik mij soms druk over kon maken heb ik meer gewaardeerd dan ik misschien heb laten merken.

Verder wil ik iedereen van de CST groep bedanken voor de fijne werksfeer, de laagdrempelige contacten en de gratis lunches. Onder andere de traditie van de eerste conferentie als "freebee" geeft duidelijk aan dat de groep meer dan alleen een academische vorming nastreeft. Maarten, bedankt voor het opzetten van deze vruchtbare omgeving. Ook wil ik graag de leden van het Advanced Thermal Control Consortium bedanken voor hun bijdrage en de kans om deze PhD te kunnen doen. De korte lijntjes met de bedrijven zijn erg waardevol en worden gewaardeerd, wat wel blijkt uit de vele co-publicaties met de industrie.

I would also like to express my gratitude to the members of the PhD committee, professors Hans Vermeulen, Johan Schoukens, and Jonas Sjöberg and Jean-Philippe Noël and Rob van Gils, for their participation in the defense and for the valuable feedback they provided to improve the concept thesis.

De studenten die onder mij hun BSc of MSc gehaald hebben wil ik graag bedanken voor hun inzet en (indirecte) bijdrage aan dit proefschrift. Andreas, Bart, Bas, Gijs, Niels, Raoul, Rens, Timo, ik ben trots op jullie resultaten en dankbaar voor de prettige samenwerking.

Vaak zeggen ze dat een persoon elke 7 jaar de helft van zijn vrienden verliest. Dat gaat zeker niet op voor mij. Adriaan, Christian, Emiel, Lennart, Luc en Sebastiaan, bedankt dat jullie zo hardnekkig zijn. Ondanks periodes van radiostilte houden we contact, drinken we bier en zijn we er voor elkaar. Dat dit nog maar lang zo mag blijven! Tim, bedankt voor alle mooie jaren met de stars on strijp, de vele kilometers zwemmen en de fijne vriendschap. Cas, mijn eftelingmaatje, bedankt voor alle chill momenten, uren series kijken en gratis Jupiler. Je zult bij mij altijd welkom zijn.

Ook bedank ik graag mijn (ex-)kantoorgenoten en de collega's van "groep Oomen" voor de gezelligheid op het werk en de avonturen tijdens de conferenties. Powernappen in Las Vegas, een roadtrip langs de grand canyon, stappen in Chez TonTon, op klaarlichte dag om 5am de Mc Donalds uitlopen, en van de glijbaan in Aqua Mundo. Mooie momenten van teambuilding en academische verbroedering. Scherpschutter Lennart, bedankt voor de ontspanningsmomenten, de humor en het gezelschap op de kamer.

Daarnaast wil ik graag mijn schoonfamilie bedanken voor de acceptatie en onvoorwaardelijke opname in de roedel, ik voel me bij jullie altijd welkom.

Ook dank ik veel van mijn succes aan de goede start gegeven door mijn kleine familie. Oma, bedankt dat jij en Opa† mij altijd gestimuleerd hebben om te verkennen, te leren en te studeren. Machteld, bedankt voor de logeerpartijen met de verhalen over vuurwerk. En mama, met mijn lofrede voor jou zou ik nog pagina's kunnen vullen. Ik dank je voor alles wat ik ben.

Tenslotte richt ik mij tot de belangrijkste persoon in mijn leven. Lieve Nicky, bedankt voor al je liefde en gezelschap in de afgelopen 5 jaar. Ik kijk uit naar onze toekomst samen en het vormgeven van onze eigen kleine familie.

Eindhoven, November 2020

For next-generation mechatronic systems it is expected that a passive isolation approach to thermally induced deformations is no longer sufficient to achieve the increased requirements on accuracy and throughput.

The main idea pursued in this thesis is geared towards facilitating a transition towards an active thermomechanical control approach by providing contributions in the areas of modeling, actuation, and control.